Design of Non-Flow Solid Hydrogen Storage for Long-Distance Maritime Applications

José Antonio González Morales

TU Delft

Design of Non-Flow Solid Hydrogen Storage for Long-Distance Maritime Applications

by

José Antonio González Morales (5594995)

In partial fulfilment of requirements for the degree of

Master of Science in Sustainable Energy Technology

To be defended publicly on Friday 18 August, 2023 at 13:00

Thesis committee

Dr. Othon Moultos

Dr. Poulumi Dey

Dr. Lorenzo Botto

Dr. Carey L. Walters

Supervisor: Dr. Othon Moultos

Project duration: 10 October 2022 -18 August 2023

TU Delft

Acknowledgements

Before closing this project, I would like to be fair and thank the people who have contributed to a certain extent to get me to where I am. As I always say, the best is always yet to come, and that is why I work, whilst being aware and grateful to the people who make it possible.

First, I have a moral duty to thank my parents for the Herculean effort, passion and devotion they have put into making me who I am today.

Second, I would like to thank my supervisors for the support and effort made to bring this project to fruition. I would make a special mention to Dr Othon Moultos and Dr Poulumi Dey, who transmitted their passion for knowledge, good vibes, and desire to keep learning to me from the start. In addition, I would like to thank Dr. Lorenzo Botto and Dr. Carey Walters for their direct and indirect collaboration, contributing to this project with their knowledge and bringing me closer to professionals such as Martjin Hoogelan and PhD candidate Heng Li, whose words were helpful for this work. Moreover, I must thank my unofficial daily supervisor, Vladimir Jelle Lagerweij, who has always enlightened me with his knowledge, support and passion for science. I am sure this project would not have been the same without him. Furthermore, I would like to thank Parsa for his help in the final steps, which contributed enormously to the timely completion of this project.

Finally, I would like to thank my circle for their support, motivation, sanity and trust in the most challenging moments. Thank you, dear circle, those walks, those calls, those words were light in the darkness of the caves, and the positive in me is thanks to you. Thank you Harsh for being my unconditional support.

Eternally grateful to those who helped, those who supported, those who are here and those who left.

The best is always yet to come!

José Antonio González Morales

Delft, July 2023

Summary

Since the early 1990s, climate change has been a major human concern. The legislative fight against global warming started in 1992 with the UN Framework Convention on Climate Change, which the Kyoto Protocol and the Paris Agreement later followed. After more than 30 years of legislation and restrictions, the climate crisis continues to be a social and technological problem. In the last decade, renewable energies have made an incursion into the energy sector. Even so, much work remains to be done to reach the limit set by the Paris Agreement, which limits the average temperature rise to less than two degrees Celsius compared to pre-industrial levels. However, clean technologies inclusion has not been as efficient in sectors such as transport, where total emissions have only increased since the 1990s. This increment is even more remarkable in maritime transport. The main aims of this project focus on the design of the propulsion alternatives currently available to minimise emissions in the maritime sector, especially in the long-distance niche; modelling and validation of one of the most promising energy storage systems, solid hydrogen; comparison with its potential competitors; and definition of the conditions that these systems must meet to be a better solution than its competitors. In order to achieve this, it is necessary to know the current state of emissions in this sector, present and future applicable legislation, define which niche within this sector requires the most urgent intervention, and describe the state of the art of the different technologies that could be part of the solution to this problem to meet the Climate agreements. Therefore, these points are explored in Chapter one of this report.

Chapter two of this report delves into the operation of solid hydrogen storage. This section describes the variables that significantly impact this system's performance, such as the shape of the tank, the geometric and intrinsic properties of the material used to store the hydrogen, and the heat management of the system. Additionally, it analyses the different modelling alternatives developed in literature for this system. Finally, this chapter defines and justifies the design boundary conditions for the solution proposed in this project.

Chapter three describes the methodology involved in the coding of the model, the strategy followed for its validation, and the alternative designs studied for the choice of the solution proposed in this project. This section includes the physical and mathematical basis for the modelling and the simulation configuration used in COMSOL®.

Furthermore, Chapter four presents the solutions obtained in the validation process of the reconstructed model. Additionally, it exposes the results of the alternative designs defined in Chapter Three. Moreover, this chapter justifies the selected geometry and compares its performance with its potential competitors.

Chapter five introduces one of the most commonly assumed simplifications in the literature regarding solid hydrogen modelling, considering hydrogen an ideal gas. The methodology used to analyze the impact of this simplification on simulation results is described, and the obtained results are presented. The section concludes by interpreting these results, discussing the relationship between the variables studied and inferring the final impact of assuming hydrogen as an ideal gas under solid hydrogen storage working conditions.

Finally, Chapter six discusses the main findings of this project, summarising and bringing together the results obtained in sections four and five of this report. Moreover, this section describes the limitations found in this project and introduces future lines of research that can complete the present project.

Nomenclature

Abbreviations

AR	Aspect ratio
EOS	Equation Of State
EU	European Union
GHG	Greenhouse Gas
ISO	International Organization for Standardization
LBG	Liquefied Biogas
LNG	Liquefied Natural Gas
LOHC	Liquid Organic Hydrogen Carriers
PM	Particulate Matter
PR	Peng-Robison
Wt%	Weight percentage

Symbols

a: Peng-Robinson value [kg $m^4 s^{-2} mol^{-2}$].

A_{Orif}: Inlet orifice area [m^2].

α_i: heat transfer coefficient [W m^{-2} K^{-1}].

b: Peng-Robinson parameter [$m^3 s^{-1} mol^{-1}$].

C: fluid temperature [K].

C_a: Adsorption rate [s^{-1}].

C_d: Orifice discharge coefficient.

C_f: local skin friction coefficient [-].

C_p: specific heat capacity at constant pressure [J kg^{-1} K^{-1}].

$c_{v_{H_2}}$: Specific heat at constant volume [J kg^{-1} K^{-1}].

c_0: stagnation velocity [m s^{-1}].

d: characteristic length where the convection is calculated [m].

d_i: inlet diameter [m].

E_a: Adsorption activation energy [J mol^{-1}].

ε: material porosity [-].

ξ: hydrogen concentration in the adsorbent.

g_r: heat production value per unit of volume [W m^{-3}].

ΔH: reaction enthalpy [J mol^{-1}].

h^+: characteristic roughness height [-].

h_R: Reservoir specific enthalpy [J kg^{-1}].

γ: Isentropic exponent [-].

K: Thermal conductivity coefficient of the material [W m^{-1} K^{-1}].

k: Peng-Robinson constant characteristic,

k_s: grain size [m].

M: molar mass [kg mol^{-1}].

Ma: Mach number [-].

m_c: hydrogen mass inside the tank [m].

$\dot{m}_i$: hydrogen inlet mass flow [m s^{-1}].

$\dot{m}_{RA}$: mass flow rate inlet ratio [-].

$\dot{m}_o$: outlet mass flow [kg s^{-1}].

n_1: Stacked torus elements for L=1.8m.

n_2: Stacked torus elements for L=10.8m

P_C: Hydrogen tank pressure [Pa].

P_{crit}: hydrogen critical pressure [Pa].

$P_{\mathrm{eq,ads}}$: Equilibrium pressure given by the Van't Hoff equation [Pa].

P_R: Reservoir pressure [Pa].

P_r: Prandt number [-].

P_{ref}: reference pressure [Pa].

$\dot{Q}_{mat}$: Heat flux balance in the adsorbent material [W].

$\dot{Q}_{pipe}$: Heat flux balance in the pipe [W].

$\dot{Q}_{tank}$: Heat flux balance in the tank's shell [W].

R: Universal gas constant [J K^{-1} mol^{-1}].

Re: Reynolds number [-].

ρ_C: Hydrogen inside the tank density [kg m^{-3}].

ρ_{mat}: material density [kg m^{-3}].

ρ_n: hydrogen density at the nozzle [kg m^{-3}].

ρ_R: Hydrogen reservoir density [kg m^{-3}].

ΔS: reaction entropy [J mol^{-1} K^{-1}].

S_t: Stanton number [-].

t: time [s].

T_C: Gas temperature [K].

T_{crit}: hydrogen critical temperature [K].

T_{mat}: Material temperature [K].

u: Internal energy [J kg^{-1}].

u_0: Reference state internal energy [J kg^{-1}].

U_{H_2}: Hydrogen internal energy [J].

$\dot{U}_{H_2}$: Hydrogen internal energy time derivative [W].

v: fluid velocity [m s^{-1}].

ν: hydrogen viscosity [kg $m^{-1}s^{-1}$].

v_{e_i}: hydrogen inlet velocity [m s^{-1}].

v_{e_o}: hydrogen outlet velocity [m s^{-1}].

v_{moc}: molecular volume [m^3 mol^{-1}].

v_n: hydrogen velocity at the nozzle [m s^{-1}].

wt: maximum weight percentage of hydrogen into material [%].

x: plate length [m].

ω: Acentric factor.

Z: compressibility factor [-].

Table of Contents

Table of Figures

Chapter 1: Introduction

In its fifth report, the Intergovernmental Panel on Climate Change (IPCC) stated that human activities are almost entirely responsible for global warming after the pre-industrial era [1]. The increment in the average temperature of the planet, the melting of the poles, and acid rain are some of the devastating consequences for the Earth that this emission increment has caused [1]. That is why regulators and governments have increased restrictions on emissions, with regulations such as the UN Framework Convention on Climate Change, the Kyoto Protocol, and the Paris Agreement limiting the rise in global average temperature to below 2°C compared to pre-industrial levels [2]. The IPCC's sixth report states that temperatures rising more than 1.5°C compared to pre-industrial values could have catastrophic consequences for humans and nature [1]. Hence, multiple regulations are being applied to reduce greenhouse gas emissions [1]. Despite the stagnation in human growth in recent years, GHG (Greenhouse Gases) emissions have continued to rise [3]. Furthermore, the IPCC report mentions hydrogen as one of the tools to be implemented in a renewable future to address the dramatic consequences of pollution [1].

1.1. Maritime emissions context and regulation

Maritime shipping was responsible for 3-4% of the total CO_2 emissions in the EU (European Union), with around 144 million tonnes of CO_2 in 2021 [4], being the second largest emitter after road transport [5]. Moreover, those emissions are projected to increase by 40% to 2050 in most of the long-term energy and economic scenarios in the EU [4]. Therefore, due to the contamination of this sector and future projections, several regulations and concrete targets are being implemented. These restrictive policies can be categorized as zero-emission policies and emission limitation policies.

The Norwegian parliament and the Maritime and Port Authority of Singapore have launched zero-emission policies for the near future. First, The Norwegian parliament has dictated the resolution of zero emissions requirements for tourist boats, cruise ships, and ferries in the World Heritage fjords by 2026 [6]. The fjords would be the world's first zero-emission zone at sea [6]. The Norwegian Maritime Authority is creating the regulation's requirements [7]. Second, the Maritime and Port Authority of Singapore launched a directive which obligates ship owners to ensure that at least 50% of their fleet registered in the Singapore Registry of Ships (SRS) are neutral emissions by 2050 [8].

The International Convention for the Prevention of Pollution from Ships (MARPOL) and Fuel EU Maritime aim to restrict greenhouse gas emissions. MARPOL published the revision of Annex IV adopted on 15 July 2011 [9]. This regulation sights to reduce the carbon intensity of international shipping by at least 40% by 2030 and 70% by 2050 compared to 2008 [9]. Additionally, this Annex states that the CO_2 emission must be reduced by at least 50% by 2050, compared to 2008 [9]. The Fuel EU Maritime through The European Commission introduced a proposal which focuses on reducing the annual average GHG intensity by 2% by 2025 compared with the 2020 baseline, 6% by 2030, 13% by 2035, 26% by 2040, 59% by 2045, and 75% by 2050 [10]. Moreover, the European Parliament proposes to harden these restrictions, looking for a reduction of 20% by 2035, 38% by 2040, 64% by 2045, and 80% by 2050 [10].

Then, considering the coming regulations, zero emissions solutions are needed. Recently, interest in using hydrogen for maritime propulsion has increased significantly [11]. The number of papers published in Scopus on this topic increased by almost 50 % each year since 2016 [12]. It seems that hydrogen could be a viable alternative to traditional propulsion methods [13].

1.2. Immediate market implementation

After understanding the regulatory context and the needs of the maritime transport sector, this section argues which maritime subsector hurries zero-emission solutions.

Firstly, considering the order of relevance, long-distance maritime transport is the most relevant [14]. Due to its impact on international trade, the economic dependence of many countries and its efficiency [14]. Maritime transport mobilises three-quarters of all shipping and is responsible for one-fifth of the transport sector's emissions [14]. Although, it is the lowest energy-consuming transport mode considering its market share, it has a significant impact on the emissions, as previously shown [14]. These are the main arguments why the Energy Technology Perspective report published by the International Energy Agency stated that long-distance maritime shipping needs zero-emission propulsion systems due to their importance and the difficulties in finding an alternative zero emission transport [14].

Secondly, nine of the largest companies in the world have announced their intention to transition to zero-emission shipping by 2040. These companies include Amazon, Inditex, Ikea and Michelin. The latter has announced a $2 trillion investment to achieve zero-emission long-distance shipping by 2040 [15].

Finally, as shown in the following subsection 1.3, companies such as Fleetzero, Future Proof Shipping, UECC (United European Car Carriers), and Soya Group are working on solutions for this problem.

Therefore, long-distance maritime transport has been chosen as the target implementation of this project, as there is a technical urgency to comply with the applicable legislation in the medium term, interest in the market to use these solutions and interest from companies to develop them.

1.3. Solutions for the maritime shipping emissions problem

This sub-section covers most of the low pollution alternatives to traditional propulsion systems that have been researched and developed. This segment describes the different solutions, technology, advantages, and disadvantages and TRL (Technology Readiness Levels) of each. These solutions are categorized into low and zero-emissions technologies.

1.3.1. Low emissions alternatives

In the case of low-emission propulsion systems, there are two main approaches, alternative low emissions fuels, and hybrid systems, which mix traditional propulsion systems with greener solutions. The technologies listed are transitional, as they cannot achieve the zero-emissions required by the different emission regulations.

1.3.1.1. Alternatives fuels

This segment includes the most extensive and implemented alternative fuels in the maritime shipping sector. These are:

- Ammonia has been proven a viable solution for cargo ships [16]. This fuel is exploited through the combustion in an engine or the injection in a fuel cell for its subsequent conversion to electrical energy [17]. The reduction of CO_2 emissions can be significant compared to traditional fuels. However, the combustion of ammonia produces more nitrous oxide, whose greenhouse gas potential is two hundred and seventy times higher than carbon dioxide [18]. Therefore, its combustion implementation may mitigate CO_2

emissions but still contribute to the greenhouse effect. The first ammonia-fuelled cargo using a reformer and fuel cell called Viridis Bulk Carrier was launched in 2023 [19].

- Methanol is an alternative fuel with a long history in the shipping industry. Currently, methanol is supplied to the 125 biggest ports in the world [20]. This fuel can reduce up to 15% of the carbon dioxide emissions, SO_x (Sulfur Oxides) and PM (Particulate Matter) emissions by more than 95% and NO_x (Nitrogen Oxides) emissions by more than 80% compared to traditional fuels [20]. In 2019, the first dozen ships using methanol as the primary combustible were launched, making it is a tested technology available for deployment [21].

1.3.1.2. Propulsion hybrid systems

This section introduces a new concept in maritime transport called hybridization. The goal is to reduce greenhouse gas emissions by creating hybrid ships that combine various propulsion methods. This allows ships to adjust their energy use according to specific needs, resulting in lower emissions. The mentioned projects are currently in the prototype phase and have a lower technology readiness level (TRL) compared to the previously discussed low-emission solutions.

- Fuel plus batteries: Two projects have successfully implemented this concept. First, LNG (Liquefied Natural Gas) plus batteries created by UECC, where the energy stored in the batteries is limited to propelling the cargo in port and supplying part of the energy when it is docked [22]. The second concept designed by the Soya Group is called a multi-fuel vessel. It combines LNG or LBG (Liquefied Biogas) propulsion with batteries. This prototype only uses batteries for occasional peak demand [23].

- Fuel plus hydrogen: Lloyd's Register's 2023 zero-emission report proposes a propulsion system which combines hydrogen or ammonia as the principal fuel with an HFO (Heavy Fuel Oil) that is combusted in case of emergency. This hybridization drastically decreases the overall emissions as hydrogen is the predominant fuel [24]. A similar concept is employed by the Norwegian MF Hydra prototype. This vessel is powered by liquid hydrogen and two diesel engines, along with batteries to store surplus energy generated during its propulsion. It is the first ferry in the world fuelled by liquid hydrogen driven fuel cell [25].

1.3.2. Zero-emissions solutions for maritime propelling

This section distinguishes between zero-emission and neutral emissions propulsion systems. The roadmaps proposed by Zero-Emission Shipping [17], Lloyd's Register Foundation [24], and Steen et al., 2019 [26] are used for the elaboration of this subsection. These reports describe the potential technologies that could be implemented in the future of maritime transport, their advantages, disadvantages, and economic viability. Although there are differences between these reports, they consider hydrogen, alternative fuels, and biofuels as alternatives for a neutral zero-emission future. The main difference is that the Zero-Emission Shipping report does not consider batteries as a solution. It only considers electricity to generate alternative fuels or biofuels, but not as a propulsion system.

1.3.2.1. Zero-emissions systems

In this category, we find two forms of energy storage, batteries, and hydrogen. Then, the following propulsion systems are possible:

- Electric: This proposal uses batteries that store energy and an electrical motor to propels the vehicle [24]. Projects using this propulsion system are in the prototyping and validation phase. The first all-electric ship was presented in 2021 [27]. This autonomous

cargo launched by Yara has a 6.8MWh battery capacity [27]. A similar prototype is being developed by the company Fleetzero [28]. This cargo uses a modular battery system where the batteries are located in the transported containers.

- Hydrogen-electricity hybridization: This propulsion alternative combines energy storage as hydrogen and batteries. Propulsion is powered by an electric motor that uses the electricity from the batteries or the fuel cell that transforms hydrogen into electricity [24]. The Dutch prototype H_2 Barge 1, launched on May 25 in Rotterdam, is also worth mentioning. This cargo has 800 kW of electric motor, three fuel cells, 900 kg of compressed hydrogen and 1037 kWh of lithium-ion batteries [29]. In addition, two other projects have been found in the early stages of development that combine liquid hydrogen and batteries to propel the cargo [30], [31].
- Hydrogen with fuel cell: This system stores hydrogen, which is then transformed into electrical energy and consumed by an electric motor to propel the ship [24]. No projects have been found, although this system is considered a potential solution.

1.3.2.2. Net zero-emissions systems

This section includes systems with GHG emissions. However, the total cargo propulsion is neutral. These are alternative fuels and biofuels.

The alternative fuels included in the reports are ammonia and methanol.

- Green ammonia: This fuel has to be synthesized with neutral carbon emissions hydrogen and captured carbon dioxide [32]. The technology installed to propel the ships is the same as that used by non-green ammonia. The carbon neutral process of obtaining the fuel is a way of value addition.
- E-methanol: This alternative methanol propels the cargo with a synthetic mix of neutral carbon hydrogen and captured carbon dioxide [32]. E-methanol can reduce overall carbon dioxide emissions, SO_x and PM emissions by more than 95% and NO_x emissions by more than 80% compared to traditional fuels [20]. Similar to ammonia, the added value of this solution lies in obtaining the fuel process despite the propulsion system.
- Biofuels are defined as any fuel produced or derived from organic matter that can replace other petroleum-derived fuels [33], [34]. They are currently available fuels, but biofuels have a scalability problem as these indirectly impact the environment [35]. The report by the European Maritime Safety Agency lists Hydrotreated Vegetable Oil (HVO) from fats, oils, and grease feedstocks (FOGs), together with biomethane manufactured from the digestion of waste and residues, as biofuels with the best availability, sustainability, TRL and cost trends [36]. Last 2019 the Dutch company Royal Boskalis Westminster N.V. (Boskalis) launched a pilot project of the first dredging vessel running on 100% bio-fuel oil, reducing its carbon emissions by 90% [37].

As this section has shown, there are several alternatives for a zero-emission future. However, hydrogen is a vital component in many of them, either as a fuel or as an element used in other synthetic fuels. Hydrogen is listed in the reports analysed for the elaboration of this chapter as one of the major allies for maritime transport to achieve zero emissions, that is why this project focuses on its storage.

1.4. Hydrogen as an energy storage solution

Considering the environmental problems mentioned at the beginning of this section and the urgency of a future led by renewable energies, there is also a need to store this energy without polluting it due to the nature of renewable energies [38]. In the last decade, interest in hydrogen

has increased considerably as an energetic vector and carrier, mainly due to the following factors.

- Hydrogen's molecule properties. It is the most abundant molecule in the universe, accounting for approximately 90% of the visible universe [39]. Being the lightest molecule, hydrogen has the highest energy density per unit weight. However, storage is one of the biggest obstacles to its implementation [40].

The versatility of the use of the hydrogen molecule increases its relevance and attractiveness for a renewable future, whether as a transport fuel, energy vector, synthesis of other fuels, or industry feedstock to sustainably manufacture of other products such as iron or steel [41], [42].

- It is possible to generate hydrogen through a renewable, simple, and reversible process by splitting water [41].
- The decreasing price of renewable energy production has increased the interest in hydrogen [41]. Expectations for the hydrogen price are very favourable, as it is estimated that by excluding taxes on competitors by 2030, green hydrogen could have an equal production cost as natural gas. Additionally, by 2050, the production cost of green hydrogen is expected to be lower than that of blue hydrogen due to the added cost of carbon capture [43].

1.4.1. Hydrogen storage

This section covers how hydrogen is stored. It describes the storage process and relevant or limiting factors. Finally, a table highlights the advantages and disadvantages of each method.

1.4.1.1. Compressed hydrogen

This method compresses hydrogen in a gaseous state by one or multiple compressor's cascade between 20-800 bar[44]. However, 60-95 bar is the most common for static applications, with no space restriction or minimal energy density conditions. This system using low pressure minimize the drawbacks of high-pressure systems as cost and risks. However, for mobile applications which require higher energy density, the pressure increases between 350 and 700 bar [45]. In 2020 the average cost of compressed hydrogen was 2.3-3.2\$ kg^{-1} [46].

1.4.1.2. Liquid hydrogen

This mechanism of storing hydrogen consists of saturated gaseous hydrogen at 1 bar and a cryogenic temperature of around 20K to increase its energy density [47]. The main drawbacks of this process are its 40% efficiency in producing liquified hydrogen and its boiling-off [47]. However, new technologies can increase the efficiency of this process by up to 50%, but these technologies are still under research [48], [49]. Nevertheless, the boiling-off was reduced to zero for 12 days by implementing thermal insulation, optimizing the tank shape and dimensions, and implementing cooling technologies [50]. Its market price is around 14.24 \$ kg^{-1} [51].

1.4.1.3. Slush hydrogen

Slush hydrogen is a cryogenic solid-liquid two-phase fluid. This hydrogen form has solid hydrogen particles (several diameter mm) in the liquid phase [52]. This hydrogen form also suffers boil-off during transport and storage. It requires a lower temperature (13.8K), and it has a greater density (15%) than liquid hydrogen [52]. This form of stored hydrogen is still under research. Several theoretical models have not been implemented yet as they are inefficient [52].

1.4.1.4. Liquid organic hydrogen carriers

LOHCs (Liquid Organic Hydrogen Carriers) are systems composed of aromatic and alicyclic compounds. The aromatic compound has a lower hydrogen concentration than the alicyclic

compound [53]–[55]. The final LOHC is a liquid that can adsorb hydrogen. The loading process is an exothermic reaction, occurring at pressures of 1-5MPa and temperatures of 373-523K [56], [57]. While the unloading process is an endothermic reaction that occurs between 0.5-1MPa and temperatures around 423-673K [58], [59].

1.4.1.5. Liquid hydrogen carriers

Liquid hydrogen carriers combine the hydrogen molecule with other elements to facilitate storage [60]. This section includes the most relevant hydrogen carriers. These are ammonia, methanol and toluene.

Ammonia for hydrogen storage serves as a hydrogen host [61]. One of the main advantages is the know-how on the treatment, production and safety measures needed to treat ammonia, as it is a widespread compound in today's industry [61]. The efficiency of this process is close to 15% [61]. This carrier can be used directly in high-temperature solid oxide fuel cells [62], [63] or decomposed to obtain hydrogen, this is the most complicated part of the process [61].

The methanol production process has two steps regardless of the hydrogen and carbon monoxide origin. First, the reaction of these two components to form methanol, and second, its subsequent purification [64], [65]. This reaction is exothermic and in the presence of a catalyst (commonly $Cu/ZnO/Al_2O_3$ [66]) at low temperatures and high pressures.

The toluene production process has four stages storage, hydrogenation, cooling and recycle compression [67]. The primary reaction that converts hydrogen to toluene occurs most optimally at 10 bar and 240°C [60].

Papadias et al.[60] conclude in their review of these three hydrogen carriers that toluene is the most energy efficient in its production, ammonia has the lowest final carbon dioxide emissions, and methanol has the lowest production cost.

1.4.1.6. Solid hydrogen storage

This method bonds the hydrogen to a material [68]. The created bond between hydrogen and the adsorbent determines the adsorption process. It can be physisorption, chemisorption, or a combination of both [68]. Hydrogen could be stored both within the host material and as compressed hydrogen in the free volume of adsorbent. A physical bond links the hydrogen molecule and the storing material in physisorption. The H-H bond in the H_2 molecule is elongated but not broken. However, in chemisorption, a chemical bond is created between hydrogen and the storing material, the hydrogen molecule is dissociated [69], [70]. The round-trip efficiency of this storage process is around 41.5-43% [71]. This value highly depends on the inlet pressure in the tank and the adsorbent material properties [71].

Van der Waals force dominates the physisorption process. The strength of this link is weak (the enthalpy of adsorption is between 4-10 KJ/mol). The physisorption is characterized by a low-medium storage capacity and high kinetics [72]. This storage mechanism is an area process, so high-surface materials, such as carbon structures, zeolites, metal-organic frameworks, and polymers, of intrinsic porosity have been researched [72].

Chemisorption establishes a more stable link between the adsorbent and the hydrogen than physisorption. This stability implies a superior hydrogen storage capacity and slower kinetics [72]–[75].

The most widely used and studied materials for hydrogen storage were magnesium hydride and lanthanum nickel alloy [76]. First, the main qualities of MgH_2 are its capacity (7.7%*wt* (weight

percentage)) and its low price due to the large availability of magnesium. The main drawback of this material is that it requires high temperatures for hydrogen desorption (300° at 1 bar), which makes its implementation difficult due to the system's working conditions. Second, $LaNi_5$ has faster kinetics than MgH_2, but its capacity is significantly lower, about 1.5 *%wt* [76]. Due to the deep study of these materials in the past, most of the experiments found in the literature use them, even though they are not the best materials for this purpose.

1.4.2. Hydrogen storage solutions comparison

This segment summarizes the working conditions and capacity of the hydrogen storage methods described in the present subsection and argues the hydrogen storage technique on which this project focuses.

Table 1: Summary table of the working conditions and capacity of the various hydrogen storage methods.

Method	Gravimetric density [wt%]	Volumetric density [MJ L^{-1}]	Temperature [K]	Pressure [MPa]	Reference
Compressed	5.7	4.9	293	70	[44]
Liquid	7.5	6.4	20	0.1	[44]
MOF	4.5	7.2	78	2-10	[77], [78]
Carbon structures	2	5	298	10	[79]-[80]
Metal hydrides	1.5-18.5	2.9-23.6	77-673	1.5-18.5	[76], [81], [82]
LOHC	8.5	7	293	0.1	[56], [57]
Liquid Carriers	15.5	11.5	298	1	[64], [65]

Analysing the above table shows that solid storage has theoretical qualities that are advantageous over its competitors. Solid storage has higher gravimetric and volumetric density than currently used methods. It also has lower operating pressures than compressed hydrogen and higher operating temperatures than liquid hydrogen. Moreover, reviewing how the shipping industry is inclined to work with pure forms of hydrogen, solid storage has a competitive advantage over liquid carriers.

Furthermore, considering the different alternatives for hydrogen storage, compressed and liquid hydrogen have been researched and implemented in other industries. Solid-state storage systems have been a less developed alternative, which could be attractive due to their higher energy density and storage stability [76]. For this reason, this project focuses on investigating the feasibility of implementing these systems as a solution for emissions in the maritime sector. Moreover, slush hydrogen has not been chosen as it is a non-developed technology. Additionally, LOHC and liquid hydrogen carriers have not been studied either, as the added value of carrying out a project with these hydrogen carriers lies in different links of their production and use chain to those dealt with in this project.

1.4.3. Solid hydrogen implementation in the Maritime sector

Only two papers linking solid hydrogen storage and maritime transport were found in the literature. First, Bevan et al. reported the hydrogen-powered transformation of a diesel ship using solid storage [83]. This paper focuses on the boat modification process instead of the science behind the installed elements. Second, Fiori et al. developed a study comparing the behaviour of different materials under restricted boundary conditions in a submarine [84].

Moreover, as seen in the following section, the literature provides enough information to reconstruct accurate, validated, and improvable models. Most of the models found in the literature assume the same simplifications, focusing mainly on the simulation of the adsorption

process and not considering other variables such as working conditions, optimization, design, energy balances, hydrogen desorption, etc. These aspects are fundamental to studying the application viability of these systems. Furthermore, the possibility of simplifying the physics behind these modelling methods to diminish the computational costs is a valuable point.

The proposal of this project is significantly different from what has been done so far in the literature by linking the implementation in the maritime sector and solid storage, as it complementary adds value to the hydrogen storage simulation knowledge and employment field.

1.5. Solid hydrogen storage models in the literature

This section describes the models in the literature that simulate solid hydrogen storage, how they work, what they are used for and the assumptions made.

The models found in the literature can be split into three categories: mathematical, Multiphysics and equivalent electric models. These methods solve the physics involved in the hydrogen adsorption process by resolving differential equations. Mathematical and Multiphysics models solve the physical equations governing this process by applying numerical methods. However, the model created with the equivalence of hydrogen adsorption to an electrical circuit solves the current differential equation obtained to simulate this hydrogen storage method. Literature models commonly compute the mass flow, temperature, pressure and hydrogen adsorption. Most models make the same assumptions for the resolution of this process [85]–[91]. These are:

1) The pressure gradient effect is negligible [91].
2) Hydrogen and adsorbent thermo-physical properties are constant during adsorption and desorption.
3) Local thermal equilibrium is assumed between the adsorbent and the gas.
4) Hydrogen is assumed to be an ideal gas.
5) The radiative heat flux of the metal hydride to the gas is neglected.
6) The storage tank is insulated, and no heat radiation is considered.
7) The adsorbent has isotropic properties.
8) Van't Hoff equation computes the equilibrium gas pressure [92].

1.5.1. Modelling limitations in the literature

This sub-section discusses the limitations of the models found in the literature to apply them to this project. Commonly, these models focus on the parameters related to hydrogen absorption. However, the energy balance and the operating conditions have not been considered. Therefore, the viability of implementing these systems cannot be analyzed, as their working conditions are not taken into account for model analysis.

In the literature, the tanks are considered adiabatic. As seen in section 2.1., metal hydrides can reach operating temperatures close to 700K, so their heat radiation to the outside should be evaluated before implementing this system, as it can be a relevant limitation in its final installation.

The above-described models are expensive to compute due to the Navier-Stokes equation for solving the hydrogen flow. There is evidence that the error of simplifying this to a no-flow condition in other parts of the tank is low [91], [93], but how this simplification to the hydrogen

inlet would affect the simulation results has not been explored. Therefore, studying the impact of this simplification and how it affects the results could lead to less expensive and faster simulations.

1.6. Research aim

The main objectives of this project are divided into four different yet synergistic fields: model reconstruction and validation, solution design, feasibility analysis of the proposed solution and comparison with existing models.

To begin with, the base model is reconstructed and validated based on literature models. In this phase, a low computational cost model is created, due to the simplification of the hydrogen flow inside the tank, as it does not model the Navier-Stokes equation. At this point, the effect of the simplification on the result can be studied and its impact on the project in regards to the relationship between the complexity and computational cost of the model to the overall profitability of the project.

Followed by which the analysed model is used to design an optimal solution for the selected implementation. For this purpose, two different tank aspect ratios, refrigeration methods, adsorbent shapes and materials are combined. The included materials differ in the adsorption mechanisms. $LaNi_5$ mainly adsorbs by physisorption and MgH_2 by chemisorption. The described approach allows us to analyse the most convenient design and if this is related to the adsorption mechanism.

Further, the implementation feasibility of the proposed solution is assessed, mainly by examining the operating conditions of the system and its energy efficiency.

Finally, the proposed solution is compared with hydrogen-fuelled solutions available on the market. In this comparison, the hydrogen storage capacity and the system efficiency are considered.

1.7. Thesis Structure

This report is composed of six chapters. The first chapter contextualizes the maritime shipping emissions problem. Moreover, it describes the possible solutions, the current state of the art of these solutions, and the development state of the technology researched in this project. Chapter 2 describes the theoretical background of the project. Chapter 3 explains the methodology followed to create and validate the model and the design of the solution. In Chapter 4, the obtained results are discussed. Then, Chapter 5 analyses the influence of the simplification of hydrogen as an ideal gas, studying the impact of this assumption on the variables that form part of the model that is the subject of this project. Finally, Chapter 6 develops in depth and connects the results obtained in sections 4 and 5, adding the limitations and future lines of research that could complete this project.

Chapter 2: Theoretical background

This chapter describes the technical background required to understand how solid hydrogen storage works, how its performance can be enhanced, how it is modelled, and the implementation design restrictions.

2.1. Solid hydrogen storage

This section focuses on elements that compose a solid hydrogen storage system and their effect on performance. The current segment is based on literature, and it deals with the tank shape, adsorbent material and its configuration, and heat management.

2.1.1. Fuel tank shape

This subsection discusses the variables that influence the shape of the tank and the different configurations that have been mainly researched in the literature. Generally, there are two different configurations:

- Cylindrical tank: Practically, this shape commonly integers two semi-spheres at each extreme to reduce the stress concentration in the joint between the body and extremes of the tank under pressure [94]. However, this geometry is simplified in most of the models to a cylinder shape tank. This tank is the chosen option in most of the papers.
- Spherical tank: Theoretically, this shape is the most optimal shape regarding the tensions in the tank, as it has the lowest stress concentration [95]. These characteristics increase the storage system's performance as the filling pressure can increase, implying higher and faster gas adsorption [96]. Mellouli et al. also stated that spherical tanks have a better filling time due to the enhanced heat management of the device due to its shape [97].

2.1.2. Adsorbent material

This segment explains how hydrogen adsorbent materials are categorized in the literature, their properties, working conditions and the possible configuration alternatives in the tank.

2.1.2.1. Adsorbent material families

The most widely accepted literature differentiation for adsorbent materials relates to the predominant adsorption process. As stated previously in segment 1.4.1.6., the two main mechanisms by which material stores hydrogen are physisorption and chemisorption, or a combination of both, although one is predominant.

Physisorption materials

As explained in Chapter 1, these materials are characterised by the physical bonding between hydrogen and adsorbent. Therefore, one of the main limitations of these materials is their high surface area. These materials have a medium-low capacity and high kinetics [72]. The most studied families of physisorption materials are carbon structures, zeolites, metal-organic frameworks, and polymers of intrinsic porosity [72].

First, most of the studied carbon structures in the literature have a capacity ranging from 2-8.25 %*wt* and require hydrogen adsorption conditions ranging from 77-298K and 20-80 bar pressure [79]. Structures operating at low temperatures and high pressures are at the upper end of the capacity range and vice versa [79]. Second, literature has shown that zeolites have a maximum theoretical gravimetric capacity of 2.86 *wt*% [98]. This family has a hydrogen capacity of 1.81-2.86 *wt* % and working temperatures around 77K and 15 bar [81],[99]. Third, Metal-Organic Frameworks (MOFs) materials such as MOF-17 or MOF-NbO have a weight capacity between

6.5-7.5 *wt%*. They adsorb hydrogen at low temperatures (77K) and high pressures (70 bar) [77], [78]. Finally, organic polymers have a broad range of variability in their capacity and working conditions. Their hydrogen capacity is between 0.5-3 *wt %* [100], [101], their adsorption temperature is 77-298K, and their working pressure is 10-94 bar. For example, Polyaline is at the lower end of the capacity range but adsorbs hydrogen at room temperature, while PIM has a capacity of 2.7 wt% and adsorbs at 77K [100], [101].

Chemisorption materials

This store mechanism establishes a more stable link between the adsorbent and the gas than the physisorption. This strong bond implies a superior hydrogen storage capacity and slower kinetics [73]. The chemisorption materials families are classified into simple or complex metal hydrides and amides, imides and mixtures.

Metal hydrides have a capacity ranging from 1.5-13.5%wt [82], and they can reach up to 18.5%wt [102]. Hydrogen absorption occurs between room temperature and 600K, desorption is at 320-700K, and absorption pressures can be between 2-290 bar [82]. Several references are attached if you wish to read more about this topic [82], [103]–[111].

Moreover, beyond the capacity and material working conditions for the consideration of an adsorbent for this project, extra parameters related to its adsorption kinetics and thermal properties are required to model the system. For this reason, the following table shows the only two materials found in the literature for which all the necessary parameters for modelling hydrogen adsorption are available.

Table 2: Lanthanum nickel and magnesium hydride adsorption modelling parameters.

Material	**$LaNi_5$**	**MgH_2**
Capacity [wt%]	1.5	7.6
Enthalpy of formation [J $mole^{-1}$]	-30000	-750000
The entropy of formation [J $mole^{-1}$]	-108	-135
Activation energy ads. [J $mole^{-1}$]	21170	130000
Activation energy des. [J $mole^{-1}$]	16420	41000
Activation ads. rate [s^{-1}]	59.187	$9.8 \cdot 10^{9}$
Activation des. rate [s^{-1}]	9.57	$9.8 \cdot 10^{10}$
Porosity [-]	0.5	0.74
Density [kg m^{-3}]	8300	1800
Effective thermal conductivity [W m^{-1} K^{-1}]	2.4	4
Specific heat capacity [J $kg^{-1}K^{-1}$]	419	1545
References	[103], [112]	[91], [97], [113]

2.1.2.2. Material adsorbent shape

The present segment covers the different designs proposed in the literature for the material adsorbent. Most of the literature focuses on the four layouts shown in this subsection.

Cylindrical reactor with peripheral hydrogen supply

This configuration has a hydrogen inlet parallel to the adsorbent bed. This form of adsorbent can give two slightly different proposals depending on the percentage of volume the material occupies inside the tank. The design on the left in Figure 1 completes a high volume percentage with the metal hydride, and the non-completed one is filled with compressed hydrogen. Hydrogen is in contact with the first adsorbent layer and diffuses through it [114]. This configuration commonly installs an external cooling jacket to improve the kinetics of the adsorption process [115]. This reactor configuration results in non-uniform adsorption as only one adsorbent surface is in contact with the hydrogen. Therefore, it is mainly implemented in short cylinders for lab purposes as this is a simple design, and it has fast enough kinetics for these small dimensions [116].

However, in the configuration shown on the right of the sketch, the adsorbent occupies a smaller percentage of the total tank volume, allowing the hydrogen to have a larger surface area in contact with the material. This design improves the adsorption kinetics and homogeneity due to the larger available surface.

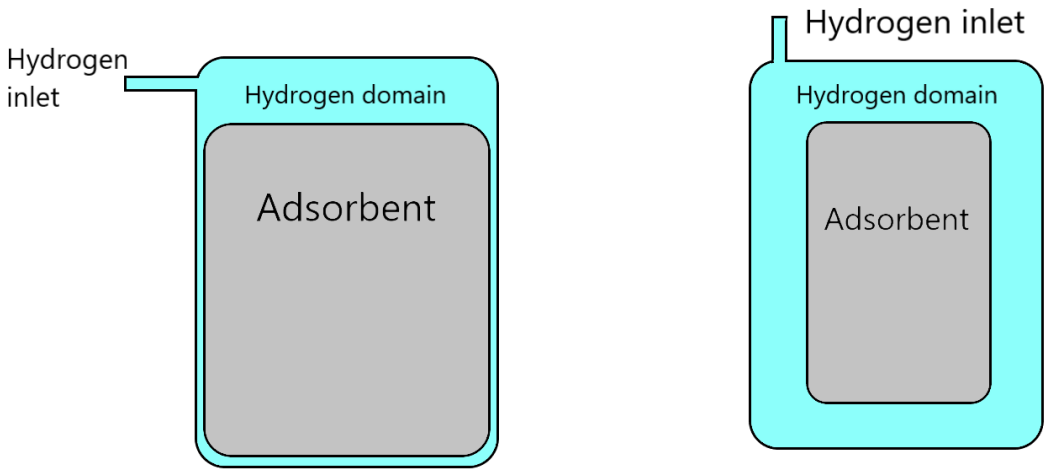

Figure 1: Sketch of the layout of a cylindrical reactor with a peripheral hydrogen inlet. This figure represents the two most common configurations within this category. The schematic on the left shows a tank in which the volume majority is occupied by the material that hosts the hydrogen. Only the upper surface is in contact with the gas. In contrast, in the diagram on the right, the volume available to be occupied by the hydrogen is greater, and the gas is in contact with all the external surfaces of the adsorbent.

Perforated cylindrical reactor

This configuration has an axial hydrogen inlet which crosses the tank and the adsorbent material. Commonly, the inlet diameter is smaller than 2µm and includes non-pressure drop filters to avoid orifice blockage [114].

The literature agrees that this configuration facilitates the application of external heat transfer techniques and allows the introduction of internal heat transfer techniques. These elements increase the dynamic kinetics of the reaction [117]–[119].

The perforated cylindrical reactors can lead to two possible alternative implementations, depending on the application and limitations:

- The external layer of the adsorbent cylinder is in contact with the internal of the tank, , as shown in the left configuration of Figure 2. Hydrogen fills the free volume in the centre of the tank during the charging process. Then, it is adsorbed by the material. This configuration commonly implements external refrigeration systems as Wu et al. [120], Wang and Brikerhoff [87], and Chibani et al. [103] installed.
- The adsorbent material is crossed-wise by refrigeration pipes, and the external layer of the cylinder contacts the pressured hydrogen inside the tank, as illustrated in the right part of Figure 2. This approach is extensively used in the literature [86], [121].

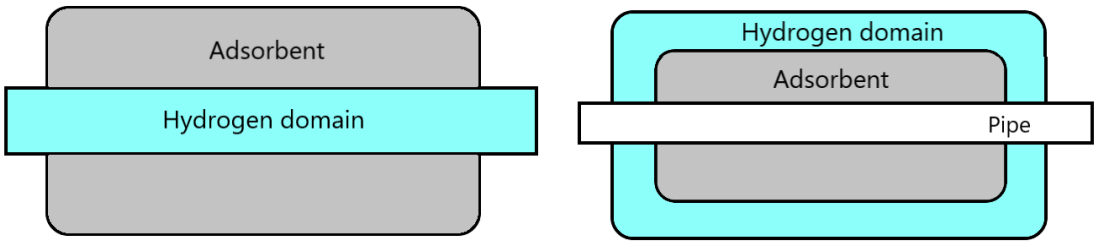

Figure 2: Sketch of the layout of a perforated cylindrical reactor. This configuration is characterized because the adsorbent is perforated. The illustration represents the two most common configurations within this category. The layout on the left shows a tank in which the majority is occupied by the material that hosts the hydrogen. It is in contact with the tank shell, and the hydrogen domain is the empty volume in the adsorbent. Only the internal adsorbent surface is exposed to the gas. In contrast, in the sketch on the right, the available volume to be occupied by the hydrogen is greater, and the gas is in contact with all the external surfaces of the adsorbent. The free space in the adsorbent installs a refrigeration system.

Rectangular reactor

This approach installs a rectangular reactor. Its main advantage is the adsorbent material capacity [114]. The hydrogen is inserted through internal arteries into the material. The combination of its shape and the method of introducing the hydrogen through internal conduits makes this configuration unsuitable for materials adsorbed at high pressure, as stress build-up would lead to premature system failure [114]. Further, as Nam et al. stated in their publication, the high ratio between the external surface and the volume makes internal heat management essential to store hydrogen in the adsorbent [122].

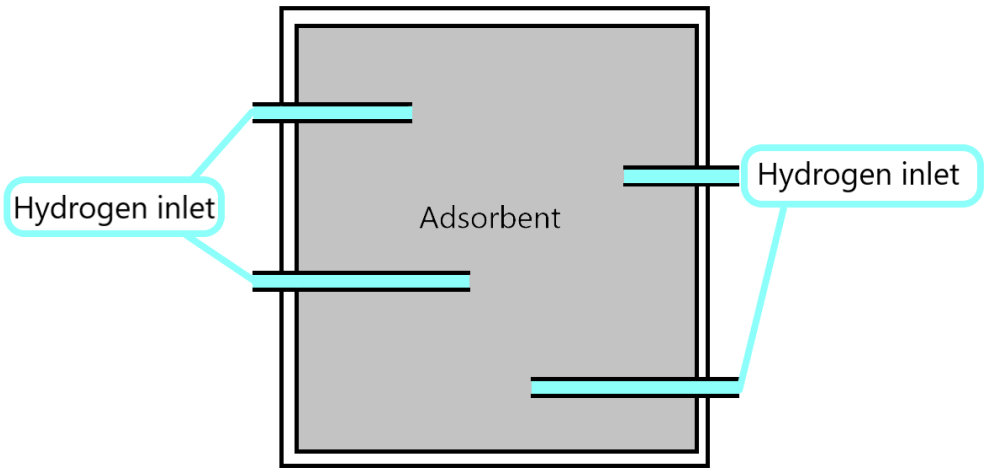

Figure 3: Sketch of the layout of a rectangular reactor. This configuration is characterised by the fact that the entire tank is occupied by the material that hosts the hydrogen. The hydrogen arteries (blue domains) are the only spaces not filled by the adsorbent, and these arteries act as hydrogen inlet pipes. These tanks are not recommended for pressurised systems [115].

Torus reactor

This configuration was used by Yartis et al. [121], Bao et al.[86] , and Delhomme et al.[123]. This design consists of a stack of torus adsorbent materials, where the internal gap of the torus inserts the refrigeration pipe. Theoretically, this solution would lead to a faster kinetics reaction as more area is in contact with the pressured hydrogen [121].

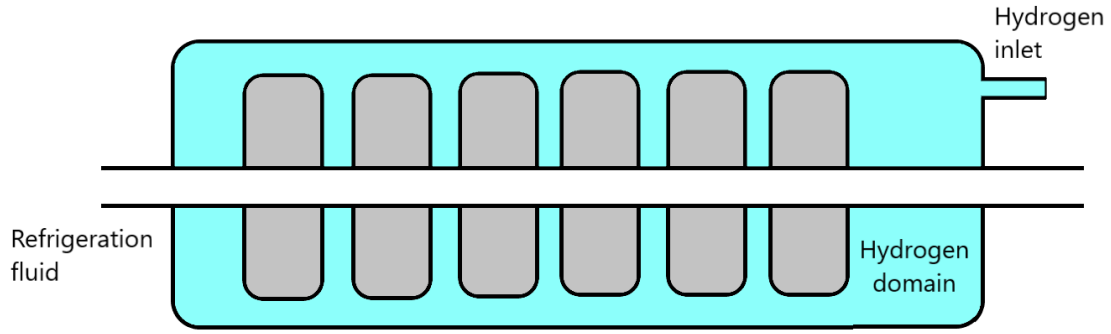

Figure 4: Sketch of a torus reactor geometry. This configuration combines an adsorbents stack and a borehole in the tank that hosts an internal cooling system. The total volume occupied by the adsorbent depends on the system configuration.

2.1.3. Heat management

This subsection includes the most researched heat transfer techniques installed for hydrogen storage in metal hydrides. Heat transfer management is a critical component of solid hydrogen storage to allow adsorption and desorption [124]. Additionally, heat transfer techniques increase the system's endurance, as higher-than-expected temperatures can lead to material degradation [124].

Afzal et al. state that there are four main alternatives to improve the heat management of a metal hydrid [125] e.

- The first option is improving the thermal conductivity of the adsorbent material. This technique is not included in this subsection as it is a material property and relies on its selection.
- The second one is the reduction in the bed radius. Regarding the Fourier law for heat conduction, a reduction in the adsorbent radius decreases the thermal resistance of the system [125]. However, further research evidenced that the radius of the bed will not have a relevant impact on the heat management of the system [126].
- The third alternative is the implementation of systems that increase the heat transfer area. They include the addition of fins in the adsorbent bed, external jackets, and cooling tubes.
- The fourth mechanism is the installation of Phase Changing Material (PCM).

This section only delves into mechanisms that increase the heat transfer area and the implementation of PCMs, as point one is a material property, and the evidence suggests that the influence of point two is minimal.

2.1.3.1. Fins

The principle behind the addition of fins is the increment of the transfer area in the adsorbent material [125]. The literature states that internal horizontal or longitudinal fins improve the heat transfer in the system[127]–[131]. However, this technique induces more failures in the system due to the concentration stresses at the corners of the fins [125].

Additionally, several studies focused on external fins in the tank. MacDonald and Rowe concluded that for small-diameter tanks, fins substantially increased the material adsorption performance (they analyzed a 4 cm reactor). However, for bigger-size tanks, external fins did not improve the adsorption kinetics [132]. Furthermore Andransen et al. demonstrated something similar when they stated that external fins did not enhance the performance of a system cooled by a fluid. However, internal fins increase the performance of the system independently of the effect of any other system [133]. Nyamsi et al. evidenced that internal fins can decrease the system's performance if the adsorbent material already includes metal foam or any other thermal conductivity improver [134].

2.1.3.2. External jackets

This refrigeration system pumps fluid through the external jacket that contacts the tank's outer surface to adsorb the heat released by the adsorbent while filling the tank and increasing the tank temperature for desorbing the hydrogen [125].

In 2009, Kaplan experimentally studied the filling parameters of $LaNi_5$ using different cooling techniques. The first tank did not implement any heat transfer improvement. The second one had 22 external fins. The third tank installed an external water jacket. All the tanks had the same size metal hydride bed. Kaplan stated that the cooling jacket was the most efficient system. It had a more relevant performance when the filling pressure was higher. [135].

Freni et al. made a Finite Element-based model for solid hydrogen storage to compare different cooling methods [136]. They used $LaNi_5$ as the adsorbent material. For this purpose, they simulated three tanks: the first model included seven cooling pipes, the second simulated tank had 12 cooling tubes, and the third included 12 cooling pipes and an external cooling jacket. The diameter of the cooling tubes was the same for all the models [136]. They obtained that the third tank had the best performance, decreasing the maximum achieved temperature in the bed by 4%, and the filling time dropped to 50% [136].

Additionally, the literature suggests that the performance increases for refrigeration fluid speed up to 2 $m\,s^{-1}$ [86], [89]. Furthermore, Bao et al. stated that the cooling effect became nominal for fluid velocities beyond 5 $m\,s^{-1}$, based on a mathematical model. As for those values, the bed metal conductivity is the limiting parameter [86].

2.1.3.3. Cooling tubes

This cooling system refrigerates the temperature of the adsorbent bed by flowing a refrigerant fluid that passes through embedded pipes in the tank.

Askri et al. performed a numerical model comparing four different configurations. The first model did not implement any heat management improvement, the second model implemented external fins, the third tank installed an internal cooling tube, and the fourth alternative combined an embedded cooling tube and internal fins The hydrogenation profiles improved by 10%,56%, and 80% respectively, compared to the first simulated tank [137].

C Na Ranong compared the performance of one single cooling pipe vs multiple cooling tubes. The multi-tubes tank achieved 80% of its capacity in half the time[138]. Nyasmsi et al. also evidenced this based on a semi-analytical model, stating that equally distributed cooling pipes had a more remarkable impact on the performance than one centre-embedded pipe [112]. However, adding multiple cooling tubes can induce an extra passive mass in the system, so this variable must be optimized for each implementation [138], [139].

Moreover, Wu et al.[140] and Nakano et al. [141] studied the performance of spiral heat exchangers. They concluded that it had a more positive impact on hydrogen adsorption than a

single exchange pipe [138], [139]. However, this spiral form suffers more stresses that could induce failure [142].

2.1.3.4. Phase changing materials

The evidence strongly supports the statement that PCM improves the kinetics of solid hydrogen storage [125], [143]. Garrier et al. stated that PCM is a viable option, but the added weight of the PCM drastically decreases the gravimetric capacity of the system by up to 50%[125], [143].

Ben Maad et al. found that the melting enthalpy is the most relevant material property for this implementation [144]. However, its heat capacity is saturated extremely fast. Mellouli et al. observed in their experiment that the PCM achieved its total heat capacity at 1% of the filling time [145].

2.1.4. Optimal theoretical solid hydrogen configuration based on the literature

This sub-section summarizes the gathered information to theoretically describe the characteristics of the best-performing solid hydrogen storage system.

First, the literature has shown that a spherical tank is an optimal shape, as it allows the filling pressure increment [96], hence decreasing the filling time. Additionally, this shape induces a more optimal heat transfer [97]. Secondly, the toroid-shaped materials minimize hydrogen adsorption time due to their larger contact surface area [121]. Thirdly, the evidence shows that combining the external jacket and cooling tube reduces the filling time. Decreasing it by up to 50% [136]. In addition, the multiple cooling tube installation is evidenced to improve the adsorption performance [138]. However, this involves a more complex system and a higher energy expenditure in the operation of the system that could decrease the overall efficiency [138], [139], which is why this project compares both cooling solutions and differentiates the cases in which it is more advantageous to use one or the other cooling system. Furthermore, spiral refrigeration pipe has a more positive impact on the adsorption performance than straight cooling pipes. However, they induce more stress on the material. This stress accumulation means more premature failures. Therefore, its implementation has not been considered [143].

These design improvements would allow the installation of greater capacity absorbers, as this improved heat transfer and increased filling pressure would further enhance the advantages of this method of hydrogen storage.

2.2. Solid hydrogen storage modelling

In Chapter 1, it was mentioned that the models used to simulate the process under investigation in this project rely on solving the governing equations. Typically, the phenomenon is described by Partial Differential Equations (PDEs). Various types of models have been developed to address this problem.

- Mathematical models: These models are programmed by coding the PDEs involved in this process and their subsequent resolution through numerical methods [146]. These numerical methods solve the PDEs implicitly or explicitly. The solution process can influence the form of the equation. They are commonly solved implicitly, as their iteration is more stable and robust [146].
- Multiphysics models: Like mathematical models, these also solve PDEs implicitly or explicitly. The main difference is that they are less customizable than mathematical models since the user interacts with the program interface for the simulation, and the software's configuration is not modifiable. These programs, such as Comsol® [147] or ANSYS® [148], include modules that allow you to simulate models without knowing how

to program. The simulation is defined by a process that starts with the geometry definition, module selection and establishment of the input parameters.

- Equivalent electrical models: These models solve the hydrogen adsorption process by developing an equivalence between hydrogen and an electrical circuit [87]. The analogous model includes current sources, resistors and capacitors. In the same way as the previous ones, they finally obtain PDEs that they solve implicitly or explicitly [87].

2.2.1. Strengths and weaknesses analysis

This section summarises the advantages and disadvantages of the modelling alternatives and argues the case for the one chosen.

Table 3: Summary of the strengths and weaknesses of the three alternatives used in the literature to model solid hydrogen storage.

	Strengths	Weaknesses
Mathematical model	• Customisability • Highly optimizable • Versatility • High integrability	• Potentially unstable • Requires programming skills
Multiphysics model	• Ease of use • Complete and optimise the programme • No programming knowledge is required	• Less customizability • Less possibility of integration with other tools
Equivalent electrical model	• Lowest computational cost [87] • Simple	• Equivalence-induced error • Difficult to connect the output to the physics governing the process • Does not allow for changing model assumptions or simplifications

A mathematical model was deemed the most suitable choice for this project due to its potential for customization, optimization, and integration. These attributes were the primary reasons behind its selection. However, during the coding phase, challenges arose in stabilizing the results obtained from the Partial Differential Equations (PDEs). Eventually, after rigorous experimentation, the model achieved stability using a time step of 10^{-7} seconds. Nevertheless, this fine time-stepping rapidly consumed the program memory, leading to memory-related issues.

In response to this limitation, a transition was made to a multiphysics model, which automatically stabilizes the model, and no memory problems were encountered with this approach. The adoption of the multiphysics model allowed for a more reliable and efficient simulation of the phenomenon under study, addressing the difficulties faced during the implementation of the initial mathematical model.

2.3. Design restrictions based on market implementation

This section develops those constraints considered for the design of the proposed solution. Design constraints may be due to regulations limiting the system's working conditions or implementation.

The applicable regulation has been analysed, and no limitations to the design and working conditions of the storage system have been found. Therefore, it has been decided to opt for a similar proposal to the one made by Fleetzero and Future Proof Shipping. These companies designed an energy storage solution that can be integrated into a standard cargo container. This application could be interesting, as it would allow a modular design, could reduce costs and adapt the solution to the use case. Furthermore, by adopting this standardised design, the performance solution can be compared with the proposed Future Proof Shipping for its H2 Barge 1 prototype.

A more detailed analysis of the modular storage design is advantageous as it would allow the installation of flexible number a storage containers and maximise the cargo capacity depending on the fuel required. In addition, this system would reduce the filling times of the system, as they could be filled before their use in the cargo.

Moreover, considering this type of operation and the final implementation, the most relevant variables to analyse and increase the accuracy of the results are the adsorbent saturation time during filling and the time it would take to discharge. Both variables determine the supply capacity of the system and indirectly show the energy that must be invested to store and extract the hydrogen from the material.

For these reasons, the design constraints of the system are limited to the interior dimensions of a standard 40 ft container and its maximum allowable mass. These boundary conditions are:

Table 4: Standard measurements of a 40 ft container, defined in ISO 668:2020 [149].

Standard 40 ft container, ISO 668:2020	
Internal length	12.03 m
External length	12.19 m
Internal width	2.03 m
External width	2.44 m
Internal height	2.39 m
External height	2.59 m
Maximum additional load	26740 kg

Chapter 3: Methodology

This project focuses on a model development to simulate the process given in solid hydrogen storage, designing a solution for long-distance maritime transport, analyzing its viability, and comparing it with its competitors. Then, the following bullet points summarize the methodology followed in this project:

- First, an accurate model is reconstructed to simulate the physical adsorption process.
- Second, it is validated based on the literature and compared to similar models and empirical data to verify the obtained results.
- Third, the hydrogen desorption process is modelled.
- Fourth, after verifying the model, the design process starts. The literature review and the model limitations are considered for designing an optimal system to increase its performance and viability.
- Finally, the obtained solution is compared to the currently implemented solutions.

This section collects the configuration, equations and boundary conditions that compose the model created in COMSOL® v6.1 [147].

3.1. Reference model validation

This subsection describes the methodology followed to verify the model, as this validation is required to see how accurately it represents the adsorption/desorption process in the host. The simulation results are compared with the paper elaborated by Jemni et al. [150] to verify the model. This project was chosen as a reference, as it allows us to validate the model under different pressure and temperature conditions, and the filling time and emptying of the tank were low, reducing the computation time and cost and accelerating the validation process. Moreover, this publication also includes the results of their proposed model, so this paper allows us to compare this project's model performance with experimental data and models. It is worth noting that its design approach is slightly different as it installs a filter at the hydrogen inlet. However, adjusting the orifice diameter of the proposed model completes the equivalence between the two models.

3.1.1. Adsorption model definition

The geometry sketch was defined using a 2D axisymmetric space definition. Two-dimensional axisymmetric models are used for symmetrical geometries concerning an axis of revolution. Finally, a three-dimensional geometry is generated by combining a 2D geometry and a revolution axis. These are computationally less expensive compared to 3D models. Moreover, the simulation is time-dependent. The COMSOL® modules used for this simulation are heat transfer in solids and fluids and global and domain equations.

This model section shows the model domains. Domain 1 is composed of the cooling fluid. The pipe containing the cooling fluid is domain 2. Domain 3 is composed of the tank containing the system. The compressed hydrogen inside the tank makes up domain 4. Domain 5 is the set of torus elements that constitute the total adsorbent.

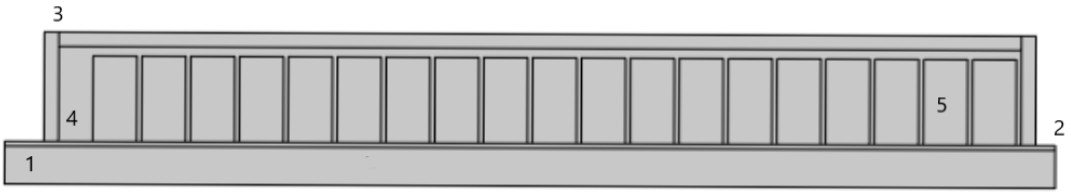

Figure 5: Geometry proposed by Bao et al. [86] *used for the model validation.*

3.1.1.1. Governing equations

The equations implemented in this model are heat flow, mass balance, momentum balance and equilibrium properties and reaction kinetics [146]. Therefore, this section divides the used equations into inlet definition parameters, heat transfer, and gas definition.

Inlet definition parameters

This segment presents the equations used to define the inlet mass flow and velocity. The hydrogen tank is considered a thermodynamic open system that goes through a quasi-steady process.

First, to calculate the inlet mass flow, a mass balance is defined. Then, we get:

$$\frac{dm_c}{dt} = \dot{m}_i \tag{1}$$

where m_c denotes the hydrogen mass inside the tank [m] and $\dot{m}_i$ is the hydrogen inlet mass flow [m s^{-1}].

Second, the hydrogen inlet mass flow is inserted in the model by the following step equation deduced by approximating the tank inlet to a nozzle and assuming that on one side of the nozzle is the reservoir and on the other the hydrogen tank. For the derivation of this equation, see the following reference [151]. These equations are implemented as general variables in the COMSOL® model.

$$\dot{m}_i = C_d\, \rho_R\, A_{Orif} \left(\frac{P_C}{P_R}\right)^{\frac{1}{\gamma}} \left\{\left(\frac{2\gamma}{\gamma-1}\right)\left(\frac{P_R}{\rho_R}\right)\left[1-\left(\frac{P_C}{P_R}\right)^{\frac{\gamma-1}{\gamma}}\right]\right\}^{1/2} \text{ for } \left(\frac{P_C}{P_R}\right) > \left(\frac{2}{\gamma+1}\right)^{\frac{\gamma}{\gamma-1}} \tag{2}$$

$$\dot{m}_i = C_d \sqrt{\gamma\, P_R\, \rho_R}\, A_{Orif} \left(\frac{2}{\gamma+1}\right)^{\frac{\gamma+1}{2\,(\gamma-1)}} \text{ for } \left(\frac{P_C}{P_R}\right) \leq \left(\frac{2}{\gamma+1}\right)^{\frac{\gamma}{\gamma-1}} \tag{3}$$

where $\dot{m}_i$ is the inlet mass flow [kg s^{-1}], C_d is the orifice discharge coefficient [-], ρ_R is the hydrogen reservoir density [kg m^{-3}], A_{Orif} is the inlet orifice area [m^2], P_C is the hydrogen tank pressure [Pa], P_R is the reservoir pressure [Pa], and γ is the isentropic exponent [-].

Third, the inlet hydrogen velocity equation is:

$$v_{e_i} = \frac{\dot{m}_i}{\rho_R A_{Orif}} \tag{4}$$

where v_{e_i} denotes the hydrogen inlet velocity [m s^{-1}].

Gas definition

These equations define the hydrogen properties. In this model, hydrogen is approximated to an ideal gas, so the equation that gives the gas pressure is:

$$P_C = \frac{m_c\, R\, T_C}{V_{avail}\, M_{H_2}\, Z}$$

(6)

where R is the universal gas constant [J K^{-1} mol^{-1}], T_C is the gas temperature [K], $M_{H_2}$is the hydrogen molar mass [kg mol^{-1}], and Z is the compressibility factor at reservoir conditions [-].

The time derivative of the hydrogen internal energy is calculated through an energy balance in the system. This balance integrates the entering energy into the tank by the hydrogen inlet and the leaving the system as heat.

$$\dot{U}_{H_2} = \dot{Q}_{mat} + \dot{Q}_{pipe} + \dot{Q}_{tank} + \dot{m}_i \left(\frac{v_{ei}^2}{2} + h_R\right)$$

(7)

being $\dot{U}_{H_2}$the hydrogen internal energy time derivative [W], $\dot{Q}_{mat}$ is the heat flux balance in the adsorbent material [W], $\dot{Q}_{pipe}$ is the heat flux balance in the pipe [W], $\dot{Q}_{tank}$ is the heat flux balance in the tank's shell [W], and $h_R$is the reservoir specific enthalpy [J kg^{-1}].

Then, the temperature can be calculated using the definition of the internal energy for an ideal gas.

$$T_c = \frac{U_{H_2}}{c_{v_{H_2}}\, m_c}$$

(8)

where U_{H_2} is the hydrogen internal energy [J], and $c_{v_{H_2}}$is the specific heat at constant volume [J kg^{-1} K^{-1}].

Heat transfer

This model's section uses the general heat transfer equation. This equation is in the solid and fluid heat transfer module in COMSOL®. It applies to domains 1,2,3 and 5. The first term of the equation calculates the heat conduction through the different media, the second term represents the heat transfer due to the convection of the fluids with the solid elements, and the third term is the heat generated by the adsorbent with the hydrogen adsorption.

$$\rho\, C_p \frac{\partial T}{\partial t} = \nabla(k\nabla \mathrm{T}) - \nabla(v\, C) + g_r(x, r)$$

(9)

where ρ is the density [kg m^{-3}], $C_p$is the specific heat capacity at constant pressure [J kg^{-1} K^{-1}], T is the temperature [K], C is the fluid temperature [K], t is the time [s], v is the fluid velocity [m s^{-1}], k is the thermal conductivity [W m^{-1} K^{-1}], and $g_r$is the heat production value per unit of volume [W m^{-3}]. The heat production is calculated with the following equation:

$$g_r = \pm \frac{\Delta H \left(\rho_{mat}\, wt\, (1-\varepsilon) \frac{d\xi}{\partial t}\right)}{M_{H_2}}$$

(10)

being ΔH the reaction enthalpy [J mol^{-1}], ρ_{mat} is the material density [kg m^{-3}], wt is the maximum weight percentage of hydrogen into material [%], ε is the material porosity [-], ξ is the hydrogen concentration in the adsorbent, and M_{H_2} is the hydrogen molar mass [kg mol^{-1}].

Reaction kinetics

This equation models the hydrogen adsorption reaction in the material. The equation was extracted from the paper by Chibani et al. [144].

$$\frac{d\xi}{\partial t} = C_a \exp\left(\frac{-E_a}{R\,T_{mat}}\right)\left(\frac{P_C - P_{\text{eq,ads}}}{P_{\text{eq,ads}}}\right)(1-\xi)$$

(11)

where C_a is the adsorption rate [s^{-1}], ξ is the hydrogen load in the adsorbent [-], E_a is the adsorption activation energy [J mol^{-1}], T_{mat} is the material temperature [K], and $P_{\text{eq,ads}}$ is the equilibrium pressure given by the Van't Hoff equation [Pa]. The equilibrium pressure is calculated using the following equation:

$$l_n\left(\frac{P_{\text{eq,ads}}}{P_{\text{ref}}}\right) = \frac{\Delta H}{R\,T_{mat}} - \frac{\Delta S}{R}$$

(12)

being P_{ref} the reference pressure [Pa], and ΔS is the reaction entropy [J mol^{-1} K^{-1}].

3.1.1.2. Boundary conditions

This subsection describes the different boundary conditions applied to the model. These are constraints applied to the heat transfer module in the solid and fluid.

The first boundary condition applied is the one that introduces the convection relation between the hydrogen and the rest of the domains (the tank, adsorbent material and tube). The following expression was extracted from the paper by Deymi-Dashtebayaz et al. [152], see Equation 13. In addition, it is imposed that the boundary between the hydrogen and the domains mentioned above has the same temperature as the hydrogen.

$$Nu = \begin{cases} 22512\,\dot{m}_{RA} + 1163.4 & if\ \dot{m}_{RA} < 0.03 \\ 22358\,\dot{m}_{RA}^{0,7} & if\ \dot{m}_{RA} \geq 0.03 \end{cases}$$

(13)

where $\dot{m}_{RA}$ denotes the mass flow rate inlet ratio [-].

The inlet flow rate and maximum mass flow are defined as:

$$\dot{m}_{RA} = \frac{\dot{m}_i}{\dot{m}_{max}}$$

(14)

$$\dot{m}_{max} = A_{Orif}\sqrt{\gamma \rho_R P_R \left(\frac{2}{\gamma+1}\right)^{\frac{\gamma+1}{\gamma-1}}}$$

(15)

Then, the internal convection heat transfer coefficient can be calculated:

$$\alpha_i = \frac{Nu\ K}{d_i}$$

(16)

where $\alpha_i$is the heat transfer coefficient [W m^{-2} K^{-1}], K is the material thermal conductivity coefficient where the heat transfer coefficient is being calculated [W m^{-1} K^{-1}], and d_i is the inlet diameter [m].

The second boundary condition applied includes in the model the external natural convection. The fluid with which this convection occurs is air at atmospheric pressure and 293.15 K.

The third boundary condition is set on the cooling fluid domain, indicating the fluid inlet, fluid outlet and fluid velocity. COMSOL® internally computes the relationship defining the cooling fluid convection with the cooling pipe.

Fourthly, the boundary condition of surface-to-ambient radiation is applied to the model. It simulates the heat radiated by the tank to the environment. This condition has to include the surface emissivity and the ambient temperature.

Finally, the boundary condition, which includes the thermal resistance due to the contact between two different surfaces, is applied. The thermal resistance applies to the boundaries common to the pipe, tank and adsorbent.

3.1.1.3. COMSOL validation model setup

This section contains the parameters necessary for the reference model configuration used for the adsorption model validation.

Table 5: Summary of the parameters used for the validation of the COMSOL® adsorption model. The discharge coefficient value (C_d) was extracted from references [151], and [152], and the rest of the values used for model validation appears in the verification reference model [150].

Symbol	Value
C_d	1
P_c	0.5 and 1MPa
T_R	293 K
M	0.002 kg mol^{-1}
$C_{p\ h2}$	14890 J kg^{-1} K^{-1}
R	8.314 J mol^{-1} K^{-1}
C_a	59.187 s^{-1}
E_a	21179.6 J mol^{-1}
T_0	297K
P_0	0.1 MPa
ΔH	30800 J mol^{-1}
ΔS	108 J mol^{-1} K^{-1}
ε_{por}	0.5
ρ_{sm}	8300 kg m^{-3}
$C_{p\ ads}$	419 J kg^{-1} K^{-1}
λ_e	2.4 W m^{-1} K^{-1}
wt	1.42%
k_s	78·10^{-9} Pa s
ε_{emiss}	0.6
$h_{tank\text{-}pipe}$	3000 W m^{-2} K^{-1}
$h_{ads\text{-}pipe}$	4000 W m^{-2} K^{-1}

3.1.2. Desorption model definition

This subsection describes the configuration applied to the reconstructed model to verify its performance. This segment only includes those different points from these explained in section 3.1.1. In the same way as the previous model, this one has been executed in COMSOL®.

3.1.2.1. Governing equations

The differences between the adsorption and desorption models are the mass flow computation, the relations used to simulate the hydrogen convection with the rest of the domains and the desorption reaction kinetics equation.

Hydrogen outflow

This model assumes a predefined leaving mass flow. This preset mass flow is the maximum mass flow value, even if the pressure inside the tank allows a higher hydrogen outflow. Otherwise, if the hydrogen outflow is inferior, it depends on the adsorbent capacity to desorb hydrogen. Furthermore, the outflow velocity of the fluid is set by Equation 5, and the fluid-defining properties can be computed as shown in section 3.1.1.1.

$$v_{e_o} = \frac{\dot{m}_o}{\rho_C A_{Orif}} \tag{17}$$

being v_{e_o} the hydrogen outlet velocity [m s^{-1}], $\dot{m}_o$ is the outlet mass flow [kg s^{-1}], and ρ_C is the hydrogen inside the tank density [kg m^{-3}].

Reaction kinetics

This equation proposed by Ram and Srinivasa represents the desorption reaction on the storage bed [153].

$$\frac{d\xi}{\partial t} = -C_d \cdot \exp \cdot \left(\frac{-E_d}{R\,T_{mat}}\right)\left(\frac{P_C - P_{\text{eq,des}}}{P_{\text{eq,des}}}\right)\xi$$

(18)

where C_{des} is the desorption rate [s^{-1}], E_{des} is the desorption activation energy [J mol^{-1}], $P_{\text{eq,des}}$ is the desorption equilibrium pressure given by the Van't Hoff equation [Pa], and ξ is the hydrogen load in the adsorbent [-].

3.1.2.2. Boundary conditions

For the emptying process, the boundary conditions simulating the hydrogen convection with the other elements are calculated by approximation, as the expression developed by Deymi-Dashtebayaz et al. [152] was validated for the tank-filling process, and no relationship has been found in the literature to compute the specific internal heat transfer coefficient for the desorption stage. Therefore, the relations are approximations of well-known convection scenarios. Then, the following equations have been used:

First, the Reynolds number is defined for the Nusselt's number calculations [144].

$$\text{Re} = \frac{v_{e_o}\, d\, \rho_C}{\nu}$$

(19)

where Re is the Reynolds number [-], v_{e_o} is the outlet hydrogen velocity [m s^{-1}], d is the characteristic length where the convection is calculated [m], ρ_C is the hydrogen density [kg m^{-3}], and ν is the hydrogen viscosity [kg $m^{-1}s^{-1}$].

Second, the convection process given in the adsorbent-hydrogen interface was approximated to a turbulent boundary layer on a fully rough flat plate [154].

$$C_f = [3{,}476 + 0{,}707\ln\,(x/k_s)]^{-2.46}$$

(20)

where C_f is the local skin friction coefficient [-], x is the plate length [m], and k_s is the grain size [m].

$$S_t = \frac{C_f\ /\ 2}{0{,}9\,\sqrt{C_f/2}\,\left(0.55\,h^{+\frac{1}{2}}\left(P_r^{\frac{2}{3}} - 1\right) + 9.5 - 7.65\right)}$$

(21)

being S_t the Stanton number [-], h^+ the characteristic roughness height [-], and P_r the Prandt number [-].

$$Nu_{mat} = \text{Re}\ S_t\ P_r$$

(22)

Third, the convection process present in the hydrogen-tank boundary has been simplified to a turbulent flow in smooth conduct with fully developed hydrodynamics and heat transfer [154].

$$f = (0{,}79\ln(Re) - 1.64)^{-2.46} \tag{23}$$

Where denotes f the friction factor [-] [154].

$$Nu_{tank} = \frac{\frac{f}{8}(Re - 1000)P_R}{1 + 12.7\sqrt{f/8}\,(P_R^{2/3} - 1)} \tag{24}$$

Fourth, the convection given in the pipe-hydrogen surface has been approximated to external forced flow in a pipe [154].

$$Nu_{pipe} = 0.193\ Re^{0.618} P_R^{1/3} \tag{25}$$

These are the simplification uses to compute the hydrogen convection in the desorption model.

3.1.2.3. COMSOL validation model setup

This section contains the values for defining the reference model configuration used for the desorption model validation.

Table 6: Parameters used for the desorption validation model. The discharge coefficient (Cd) was extracted from references [151] and [152], the parameters that are part of the convection of the model were taken from the reference manual [154], the values of the thermal resistance between different surfaces were selected from the work of Lemmon et al. [155], and the remaining values involved in the model validation were extracted from the reference model for verification [150].

Symbol	Value
C_d	1
P_{des}	85 mbar
P_c	0.1MPa
T_0	303 K
M	0.002 kg mol^{-1}
$C_{p\,h2}$	14890 J kg^{-1} K^{-1}
ν	9.0055 μ Pa s
C_{des}	9.57 s^{-1}
R	8.314 J mol^{-1} K^{-1}
E_{des}	164000 J mol^{-1}
T_0	303 K
P_0	1 MPa
ΔH	30800 J mol^{-1}
ΔS	108 J mol^{-1} K^{-1}
ε_{por}	0.5
ρ_{sm}	8417 kg m^{-3}
$C_{p\,ads}$	419 J kg^{-1} K^{-1}
λ_e	2.4 W m^{-1} K^{-1}
wt	1.42%
k_s	$78 \cdot 10^{-9}$ Pa s
h^+	0.01
ε_{emiss}	0.6
$h_{tank\text{-}pipe}$	3000 W m^{-2} K^{-1}
$h_{ads\text{-}pipe}$	4000 W m^{-2} K^{-1}

3.1.3. Validation model meshing

This section describes the approach employed to select the appropriate mesh shape and study the influence of the element mesh size on the obtained result. It is divided into two subsections: the mesh shape definition and the meshing size selection.

3.1.3.1. Mesh shape

This sub-section defines the shape of the mesh in each domain. For this purpose, a distinction is made between the fluid flow domains, i.e. domains one and six, and the rest. These flowing flow domains have a quad mesh, used to reduce the calculation error induced by the shape of the mesh on the results [155]. Although, in the rest of the domains, a triangular mesh is used, due to its speed and efficiency in adapting to the geometry, increasing the overall quality of the mesh and improving the accuracy of the results [156].

3.1.3.2. Validation process mesh size

This section covers the study followed to set the maximum grid size, as the mesh size has an inverse relationship with the result's accuracy and computational cost. Therefore, employing the appropriate mesh size reduces the error and the simulation computational cost.

For this purpose, the accuracy of the hydrogen saturation in the adsorbent and the material temperature results are evaluated to research the model reliability and simulation cost. The meshes simulated have a maximum element size of 1-3-5-7-9 mm and a minimum of 0.1 mm. This meshing analysis is executed over the validation adsorption model at 0.5 MPa, described in section 3.1.1.3. This mesh size computation was run on two Intel(R) Xeon(R) Gold 6248R CPUs at 3.00GHz, using two sockets with 48 cores in total, and the available memory was 191.99 GB.

3.2. Proposed designs definition

This section covers the 32 simulated models created to evaluate how the design parameters affect the system's performance and select the most viable solution. Sections 3.1.1 and 3.1.2 explain the equations and boundary conditions used in these models.

First, the simulated prototypes could be classified by the installed adsorbent materials: magnesium hydride and lanthanum nickel. Each geometry is simulated for both materials. Second, the model's dimensions can be grouped by the two possible tank orientations in the container, i.e. the tanks designed to be positioned vertically or horizontally. This restriction leads to two alternative tank measures, which allow us to evaluate how the AR (aspect ratio) modification affects the system's performance. Third, the heat management techniques and the adsorbent shape are modified to see their influence on the system's operation.

The alternative sketches shown in this section are defined by changing only the three variables highlighted in the figure: the tank length, the radius, and the adsorbent material radius. If you want to see each simulated geometry in this project in detail, see Annex A.

3.2.1. Layout 1

Figure 6 shows the section of the first geometry studied in this project. This model installs a torus adsorbent stack and an internal refrigeration pipe, similar to the Bao et al. [86] proposed solution in the referenced publication. The first domain corresponds to the cooling fluid, the second is the tube that contains the cooling fluid, the third is composed of the walls that form the tank, the fourth is the volume occupied only by the hydrogen, and finally, the fifth domain is the one that includes the material responsible for storing the hydrogen.

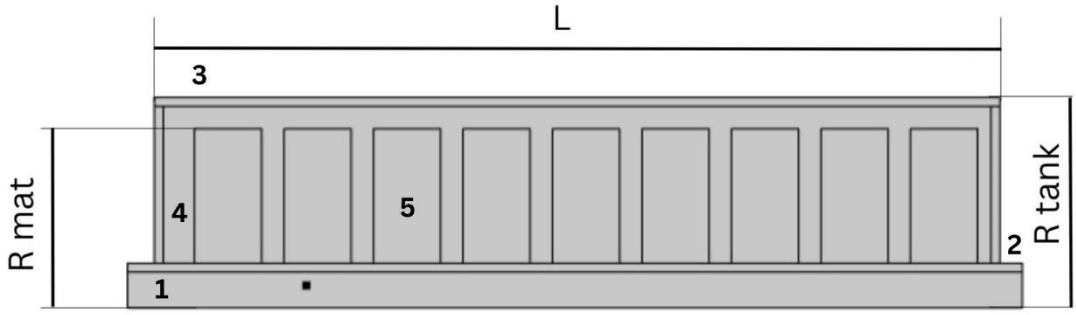

Figure 6: Geometry 1 simulated and compared with the other alternatives. This geometry contains the following domains: 1-coolant fluid, 2-pipe, 3-tank external shell, 4-hydrogen, and 5-adsorbent.

Table 7: Geometric combinations simulated for geometry one.

Variable	Geometry 1	Geometry 2	Geometry 3	Geometry 4
Tank longitude	1.89 m	1.89 m	10.89 m	10.89 m
Torus adsorbent thickness	0.15 m	0.15 m	0.15 m	0.15 m
Tank external radius	0.37 m	0.47 m	0.37 m	0.47 m
Adsorbent radius	0.3 m	0.4 m	0.3 m	0.4 m

3.2.2. Layout 2

Sketch 7 depicts the second geometry analysed within this project. In contrast to geometry 1, this alternative installs a solid cylindrical adsorbent. The domains compounding this geometry are defined in 3.2.1.

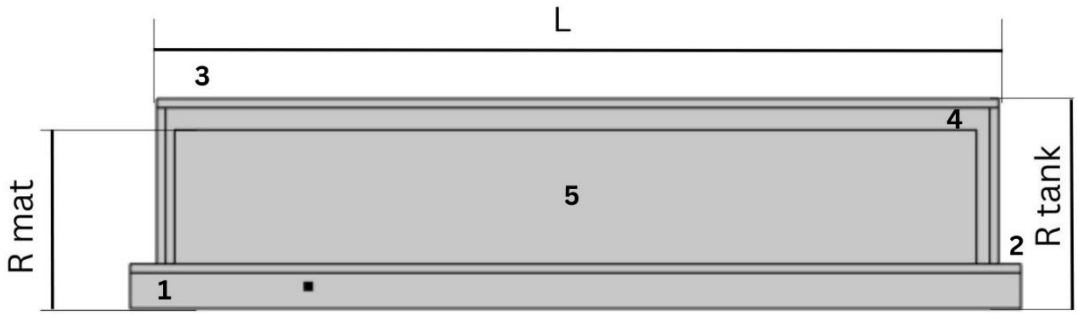

Figure 7: Geometry 2 simulated and compared with the other alternatives. This geometry contains the following domains: 1-coolant fluid, 2-pipe, 3-tank external shell, 4-hydrogen, and 5-adsorbent.

Table 8: Geometric combinations simulated for geometry two.

Variable	Geometry 5	Geometry 6	Geometry 7	Geometry 8
Tank longitude	1.89 m	1.89 m	10.89 m	10.89 m
Adsorbent longitude	1.80 m	1.80 m	10.80 m	10.80 m
Tank external radius	0.37 m	0.47 m	0.37 m	0.47 m
Adsorbent radius	0.3 m	0.4 m	0.3 m	0.4 m

3.2.3. Layout 3

Illustration 8 shows the third geometry simulated in this project, which uses geometry one as a basis and adds an external jacket to improve heat management. This model aims to quantify the performance improvement of this implementation and analyse whether it was cost-effective to install it. The first domain corresponds to the cooling fluid, the second is the tube that contains the cooling fluid, the third is composed of the walls that form the tank wall, the fourth is the

volume occupied only by the hydrogen, the fifth domain is the adsorbent, sixth is the external jacket refrigeration fluid, and finally the seventh domain constitutes the shell of the jacket.

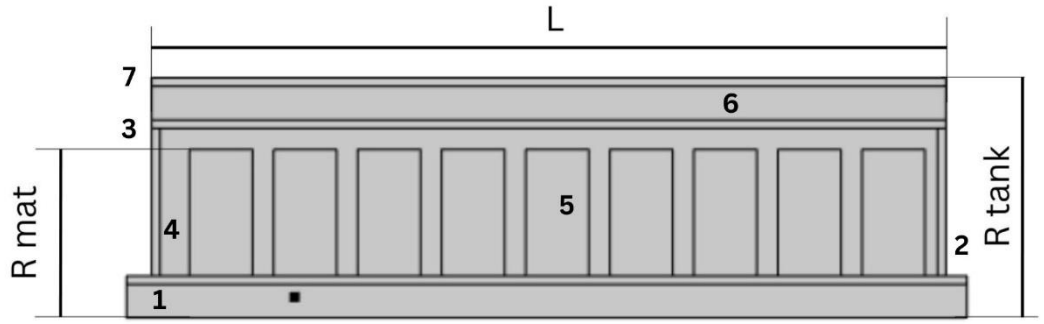

Figure 8: Geometry 3 simulated and compared with the other alternatives. This geometry contains the following domains: 1-coolant fluid, 2-pipe, 3-tank external shell, 4-hydrogen, 5-adsorbent, 6-refrigeration fluid, and 7-external jacket.

Table 9: Geometric combinations simulated for geometry one.

Variable	Geometry 9	Geometry 10	Geometry 11	Geometry 12
Tank longitude	1.89 m	1.89 m	10.89 m	10.89 m
Torus adsorbent thickness	0.15 m	0.15 m	0.15 m	0.15 m
Tank external radius	0.47 m	0.57 m	0.47 m	0.57 m
Adsorbent radius	0.3 m	0.4 m	0.3 m	0.4 m

3.2.4. Layout 4

Figure 9 depicts the fourth simulated geometry run in this project. It builds upon the foundation of geometry two and introduces an additional external jacket to enhance heat management. The objective of modelling this heat transfer technique was to assess its performance enhancement and evaluate the cost-effectiveness of the implementation. The specific domains that constitute this geometry are outlined in section 3.2.3.

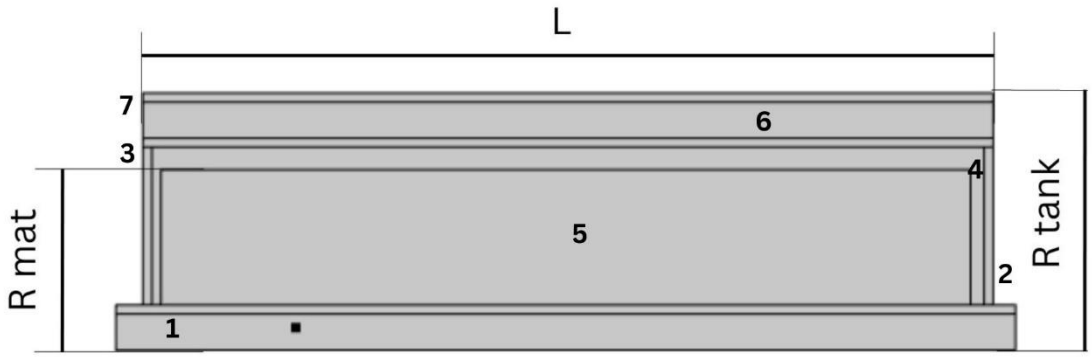

Figure 9: Geometry 4 simulated and compared with the other alternatives. This geometry contains the following domains: 1-coolant fluid, 2-pipe, 3-tank external shell, 4-hydrogen, 5-adsorbent, 6-refrigeration fluid, and 7-external jacket.

Table 10: Geometric combinations simulated for geometry one.

Variable	Geometry 13	Geometry 14	Geometry 15	Geometry 16
Tank longitude	1.89 m	1.89 m	10.89 m	10.89 m
Adsorbent longitude	1.80 m	1.80 m	10.80 m	10.80 m
Tank external radius	0.47 m	0.57 m	0.47 m	0.57 m
Adsorbent radius	0.3 m	0.4 m	0.3 m	0.4 m

3.2.5. Shared parameters in alternative models

This sub-section collects all these layouts' parameters for the different models. The adsorbent values are extracted from Table 2.

Table 11: Alternative proposed models standard modelling parameters. The discharge coefficient (Cd) was extracted from references [151] *and* [151]*, the parameters that are part of the convection of the model were taken from the reference manual* [154]*, the values of the thermal resistance between different surfaces were selected from the work of Lemmon et al.* [157]*, the magnitudes related with the refrigeration system were picked from the Bao et al.* [86] *work, and the remaining values involved in the model validation were extracted from the reference model for verification [150].*

Symbol	Value
C_d	1
r_{orif}	0.01 m
P_R	3 MPa
T_R	293.15 K
h_R	$3873 \cdot 10^3$ J kg^{-1}
M	0.002 kg mol^{-1}
$C_{p\,h2}$	14890 J kg^{-1} K^{-1}
ν	9.0055 µ Pa s
$T_{0,a}$	293.15 K
$P_{0,a}$	0.1 MPa
$T_{0,d}$	293.15 K
$P_{0,d}$	0.1 MPa
T_{amb}	293.15 K
R	8.314 J mol^{-1} K^{-1}
k_s	$78 \cdot 10^{-9}$ Pa s
h^+	0.01
ε_{emiss}	0.6
u_f	5 m s^{-1}
T_f	293.15 K
ρ_f	810.1 kg m^{-3}
λ_f	0.0944 W m^{-1} K^{-1}
$C_{p\,f}$	2350 J kg^{-1} K^{-1}
μ_f	$2.15 \cdot 10^{-4}$ Pa s
ρ_s	800 kg m^{-3}
λ_s	15 W m^{-1} K^{-1}
$C_{p\,s}$	500 J kg^{-1} K^{-1}
r_{pipe}	0.08 m
t_s	0.02 m
t_{torus}	0.15 m
$T_{ext\,fl}$	0.08 m
n_1	9
n_2	54

3.2.6. Hydrogen extraction approach during desorption for the alternative designs

The approach followed for emptying the tank is different to the validation procedure. It has been modified to improve the system's performance. Since the tank temperature drops due to the hydrogen extraction added to the heat removal from the system, caused by hydrogen desorption (as it is an endothermic process) could significantly slow or stop the desorption process. This temperature decrease reduces the hydrogen extracted from the adsorbent as the steady state is achieved with a higher hydrogen load in the material, and this scenario would affect the system's efficiency since the total hydrogen mass extracted from the tank is inferior.

Therefore, for the proposed model's simulation, the tank is preheated with the refrigeration fluid at 373K without extracting any mass flow from the system. Once the hydrogen load in the adsorbent is less than 20%, hydrogen extraction starts at a mass flow rate of 0.01 kg/s. When the steady state is reached in the adsorbent, this mass flow increases to 0.05kg/s. This approach reduces the temperature drop in the tank, favouring the fluid desorption and improving the system's performance.

3.2.7. Alternative geometries' meshing

This segment defines the mesh used for the geometries simulation described in section 3.2 since the size meshing must be modified from the one described in section 3.1.3 due to a memory limitation in the execution hardware. This mesh size change is due to the modelled tank size, as the proposed geometries are at least ten times bigger than the validation model. Therefore, the memory required for the execution of this increases significantly. Moreover, the mesh shape remains the same as described in section 3.1.3.1.

First, the mesh used in the geometries designed for vertical positioning inside the container is defined with the grid configuration described below:

- Element size calibrated for "General physics".
- Size predefined "Normal".

Secondly, the settings described below determine the mesh applied to the geometries designed for horizontal positioning within the vessel:

- The element size is calibrated for "General physics".
- The size is predefined as "Coarser".

With the described configuration, the model resolution is lower, but it is the only viable alternative for the studied geometries simulation.

3.3. Solver configuration

This subsection lists the required changes to the default settings of the COMSOL solver to find a solution due to the unstable physical nature of the modelled problem. Hence, the configuration of the COMSOL Time-Dependent solver should be changed to prevent the model crash:

First, in the tab of steps taken by the solver within the Time-Dependent solver **strict** should be selected instead of free.

Second, in the section of a fraction of the initial step for Backward Euler, the value of the initial step is reduced to **0.001**. This change reduces the error in the first iteration and eases the model convergence.

3.4. Exergy analysis

This subsection presents the methodology followed to perform the exergy analysis of the proposed system. This calculation applies to the model considered the most viable solution after observing its performance, stored hydrogen and operating conditions. The result obtained from this analysis is used to compare the efficiency of this system with its competitors.

The exergy analysis performed in this project considers the overall computation of tank operation, using the chemical energy introduced during filling as the energy entering the system and the energy extracted with hydrogen desorption as the energy obtained from hydrogen. For this study, the following equation is computed:

$$\psi_{tank} = \frac{\Sigma E_{in}}{\Sigma E_{\text{out}}}$$

(24)

where $E_{in}$is the energy getting into the system [J], and it is defined as:

$$E_{in} = m_{h_2 in}\, h_R$$

- *(25)*

being $m_{h_2 in}$the hydrogen mass inside the tank [kg] and $h_R$the reservoir specific enthalpy [J kg^{-1}].

E_{out} denotes the energy leaving the system [J], defined as:

$$E_{out} = m_{out}[u - u_0 + P_0\,(v - v_0) - T_0\,(s - s_0)]$$

- *(24)*

where m_{out} is the hydrogen mass leaving the tank [kg], u is the hydrogen specific internal energy [J kg^{-1}], $u_0$is the initial hydrogen specific internal energy [J kg^{-1}], $P_0$is the initial desorption tank pressure [Pa], v is the hydrogen molar density [m^3 mol^{-1}], $v_0$is the initial hydrogen molar density [m^3 mol^{-1}], T_0 is the initial desorption hydrogen temperature [K], s is the hydrogen specific entropy [J kg^{-1} K], and s_0 is the initial hydrogen specific entropy [J kg^{-1} K].

Chapter 4: Results

This chapter presents the results obtained in this project. It is divided into four sections: the first exposes the results obtained in the model during the verification process; the second shows the adsorbent material comparison; the third section includes the simulation's outcome from alternative designs proposed, including tank configuration and materials for the use case of this project; finally, the proposed tank geometry is compared with its competitors in the market.

4.1. Validation results

This section presents the results obtained during the model validation process. For the model verification, the two variables compared are the hydrogen proportion in the material and the hydrogen temperature. The hydrogen proportion in the host was selected as the validation variable because it shows the reaction kinetics, evolution, and adsorbent saturation state. Then, the hydrogen temperature was chosen as it is the factor that triggers the heat transfer in the system and impacts the adsorption/desorption process.

4.1.1. Adsorption

This subsection presents the results obtained during the verification process of the adsorption model. As mentioned in segment 3.1.1, the model was simulated at reservoir pressures of 0.5 and 1 MPa. This double verification aims to evaluate the filling pressure influence on the model performance. First, the results obtained in the simulation of the filling process at 1MPa are analyzed, and second, the one obtained for the 0.5MPa scenario. Jemni et al. [150] did not report hydrogen temperature data for the filling process at 5 bars, so only the hydrogen saturation in the host is compared in this scenario.

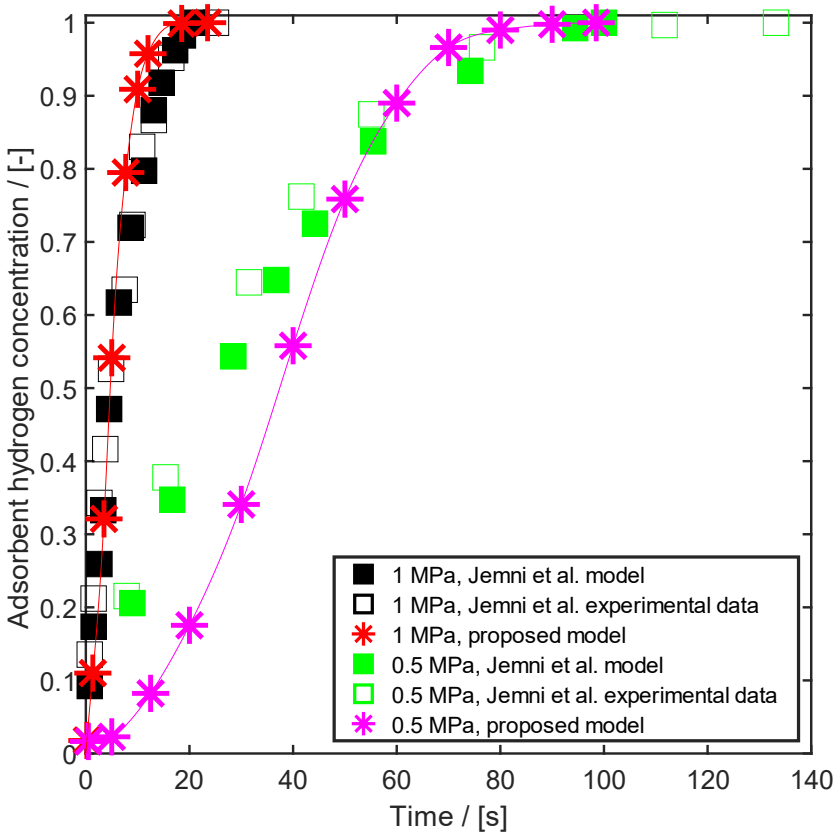

Figure 10: Results obtained in the validation process for hydrogen adsorption. This figure contains the following scenarios: a) results obtained by the model of Jemni et al. at 1MPa [150]*, represented with black squares; b)*

experimental data collected by Jemni et al. [150]*, plotted as empty black squares; c) results obtained by the model realised in this project, represented as red stars; d) results obtained by the model of Jemni et al.* [150] *at 0.5MPa, represented with green squares; e) experimental data collected by Jemni et al.* [150]*, empty green squares; f) results obtained by the model realised in this project, magenta stars.*

The results of the validation adsorption process are presented in the figure above. The data plotted in black and red represents the results obtained for the hydrogen concentration in the host at 1MPa filling pressure. These plots contain the values of the hydrogen saturation in the adsorbent according to the model proposed by Jemni et al. [150] (black squares), the experimental data collected (coloured black squares) by this research group and the proposed model in this project (red stars). Then, analysing the filling time, it can be seen how the proposed model filling time (last point of each curve) is closer to the experimental data than the result obtained by the Jemni et al. [150] model. The error in the adsorbent saturation time is almost 50% inferior to that achieved in the model proposed by Jemni et al. [150]. However, observing how the gas adsorption develops, we can see that the Jemni et al. [150] model performs better. The trend of the proposed model is more abrupt, having a slower start and faster adsorption after exceeding 0.55 saturation. In addition, the material saturation is slow, and in the second half of the simulation, only the last 5% available for saturation is filled. Next, looking at 0.5MPa plots, the highlighted observations in the filling scenario at 1MPa are accentuated. The total filling time of the proposed model is closer to the experimental data than that obtained by the model of Jemni et al. [150]. Although, their model's trend converges better with the experimental data. In this scenario, a sharper behaviour is observed than in the previous case, obtaining up to a 50% error in the first adsorption phases. This deviation is compensated later with faster adsorption.

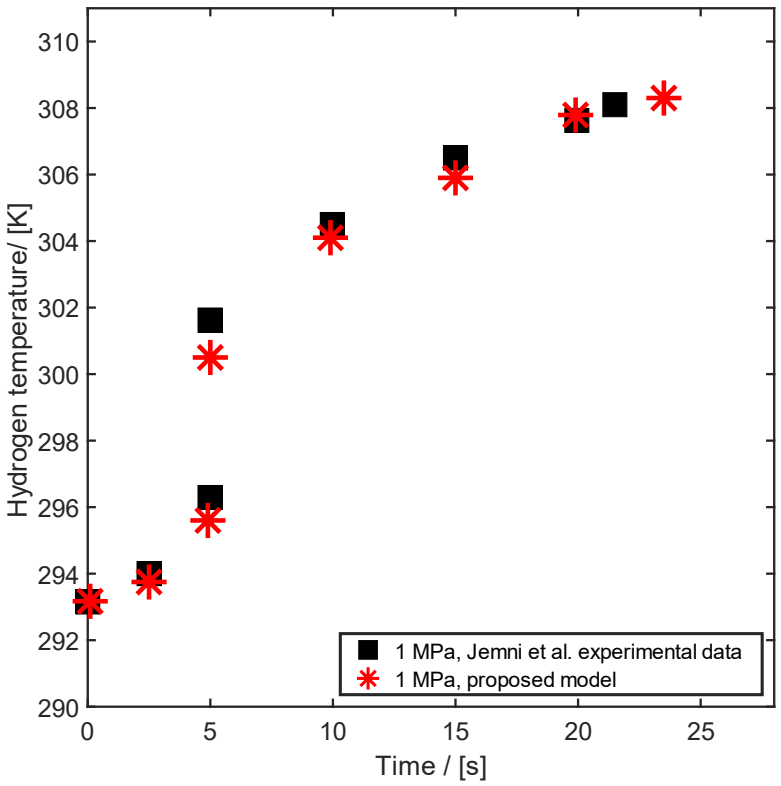

Figure 11: Results obtained in the validation process for hydrogen temperature during the filling process at 1MPa. This figure represents a) experimental data collected by Jemni et al. at 1MPa, represented with black squares; b) results obtained by the model realised in this project, red starts.

Figure 11 illustrates the hydrogen temperature in the tank during the validation filling process at 1MPa. The temperature calculated by the model follows the trend of the experimental data, with the highest deviation occurring in the abrupt rise near 5 seconds of filling. In this time frame, a maximum error of 2.45% is obtained compared to the experimental data. Moreover, in the last adsorption seconds, the values provided by the model highly converge with the measured data. Then, even though adsorption is faster, which would imply more heat generation during the reaction, it is observed that the model temperature is lower than that measured in experimental data during almost all the filling time.

4.1.2. Desorption

This subsection shows the results obtained in the desorption validation process. The conditions of this process are 0.5MPa in the tank and an initial gas temperature of 303K. In this segment, only the saturation of the adsorbent is represented since the reference paper covers the material temperature until the initial temperature of the material is recovered. The desorption process takes approximately 250 seconds, and the graph shown by Jemni et al. [150] plots 16000 seconds, so there is not enough resolution in the figure to accurately extract the temperature values. However, the minimum values can be compared. The lowest temperature measured by Jemni et al. [150] was 260K, and the minimum temperature achieved in the adsorbent during the simulation was 249K.

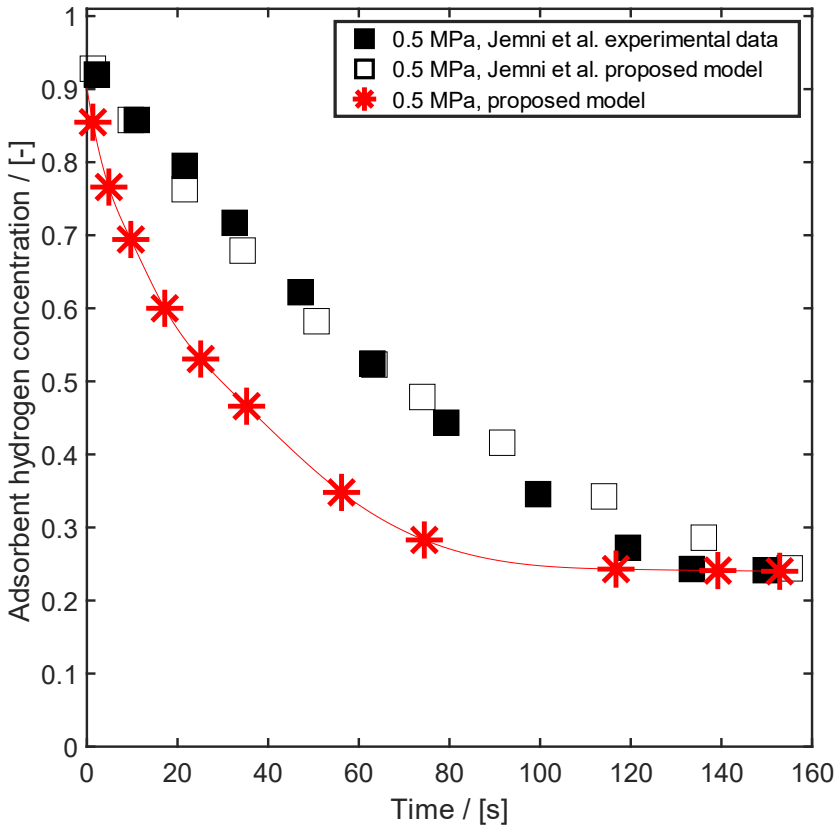

Figure 12: Results obtained in the validation process for hydrogen desorption with a tank pressure of 0.5MPa, an initial gas temperature of 303K and an emptying pressure of 85mbar. This figure shows in red stars the results obtained by the model presented in this work, and the black squares the values obtained by Jemni et al. [150].

Figure 12 shows the hydrogen load given in the desorption process. One point to note is that lanthanum nickel does not desorb all the hydrogen stored within it. The material releases 24% of the adsorbed hydrogen at this operation condition. In black is the data extracted from the

reference paper, and in red is the model outcome. Again, as observed in the adsorption validation, the model performed by Jemni et al. [150] presents a better correlation with the experimental data during the desorption process. Although, again, the total desorption time obtained from the model described in this report is more accurate, reducing the error of this parameter by almost 40%.

4.1.3. Mesh size analysis results

This subsection presents the results obtained from the optimal maximum mesh size analysis for the validation model, as mentioned in section 3.3.2. These simulations run the adsorption model at 0.5 MPa, described in segment 3.1.1. Next, the errors obtained by calculating the hydrogen saturation in the material and the adsorbent temperature are studied to select the optimal grid size.

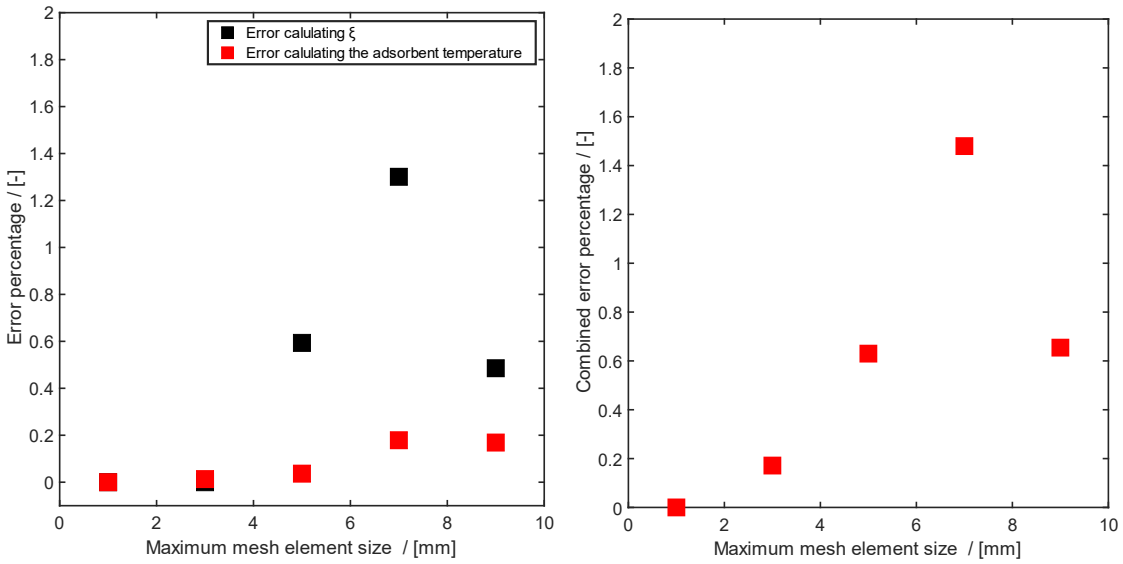

Figure 13: Error in the hydrogen saturation and adsorbent temperature calculation with six mesh sizes (1-3-5-7-9 mm). In the left section of the figure, the black square represents the error in the material saturation, and the red square represents the error in the calculation of the material temperature.

First, in the left portion of Figure 13, the errors in the computation of hydrogen saturation and adsorbent temperature are plotted separately. It can be seen that the errors in the temperature results are significantly lower than the errors in the material saturation for the bigger mesh size. A defined trend can be observed as a smaller mesh size leads to an inferior error in the hydrogen saturation in the material, except for the 9mm mesh size. However, this trend is not remarkable in the temperature of the material, as the error is close to cero. Then, returning to the saturation error data, if we analyse the 7 and 9mm mesh parameters in depth, they have a mesh quality of 0.6006 and 0.5949, respectively, and the minimum mesh quality for the 9 mm mesh is 28.23% lower. Hence, the 7 mm mesh should fit better the geometry. Therefore, the higher accuracy in the results of these variables for the 9 mm mesh could be due to the transition zone between the quad and triangular mesh. Second, observing the right-hand side of Figure 13, a more determined trend can be noted for the maximum mesh size and the added result errors for both variables, except for the 9mm mesh.

The left sector of Figure 14 shows the simulation time of the model with different maximum mesh element sizes. As expected, the smaller the element size, the longer the computation time of the model, with a significant reduction of the run time when increasing the mesh size from 5 to 7 mm. In the right sector of the figure, a marked trend relates to the increase in computation

time and reduction of the error in the previously mentioned variable calculation, except for the 9 mm mesh. Therefore, the 9 mm value was chosen as the maximum mesh size for the validation model, as the geometry studied gives more accurate results with fewer nodes and computational time.

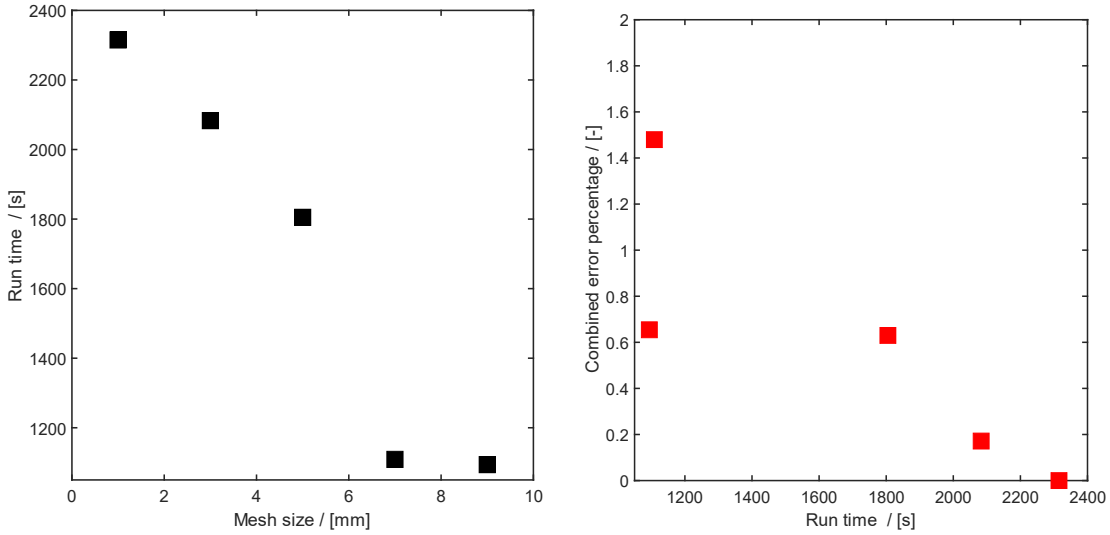

Figure 14: Correlation between the maximum mesh element size to model simulation time and the relation of the combined error in the simulation of hydrogen loading in the material and material temperature to simulation time for meshes with maximum element size 1-3-5-7-9 mm.

4.2. Material comparison

This subsection includes the results obtained in the simulations executed to compare the performance of both materials under the conditions described in section 3.4.5, whose aim is to choose the most viable material for this implementation.

First, it should be highlighted that the systems' initial and working conditions were for both materials to compare their performance. With the conditions described in section 3.4.5. of this project, no adsorption occurred in the magnesium hydride during the first 5000 seconds of the simulation. This result is a consequence of the two points described below:

- The enthalpy of formation of the reaction is almost three times higher than that of lanthanum nickel. Analysing the Van't Hoff equation, this value directly affects the equilibrium pressure at which adsorption starts. This high equilibrium pressure implies that it is necessary to preheat the material to decrease the adsorption equilibrium pressure and trigger this process, as seen in the literature cases exposed by Bao et al. [86] and Chaise et al. [113].
- The activation energy of MgH_2 is four times higher than that of $LaNi_5$. This characteristic implies that the applied energy for the reaction to take place is almost four times higher for each mole.

These two factors meant that hydrogen adsorption on MgH2 did not occur, and the only alternative was to preheat the tank or choose LaNi5. Finally, LaNi5 was the adsorbent selected to increase the overall system performance and avoid a more energy-intensive system due to the mandatory preheat. As these previously mentioned points also affect hydrogen desorption, installing magnesium hydride would make this process energetically very costly and unfeasible for the chosen application. For this reason, $LaNi_5$ is the adsorbent material used in this project.

4.3. Design results of alternative geometries

This segment shows the results obtained in the simulation of the hydrogen adsorption and desorption of the designs presented in section 3.4. The present section is divided into the results obtained in the alternative geometries for the adsorption process and the desorption result of the selected geometry due to the adsorption performance. The simulation of all possible desorption scenarios was omitted, as better adsorption kinetic implies more favourable desorption. Therefore, this allows us to save computational capacity and accelerate the obtaining results process. Unfortunately, the adsorption simulations of geometries 7, 8, 11, and 15 could not be computed due to a memory limitation in the cluster where the models run. However, their performance can be inferred by analysing the results of the rest of the models. Therefore, this section discussed the expected performance and whether they would be viable for this implementation.

4.3.1. Adsorption

This subsegment presents the results obtained in the simulation of the alternative geometries for the adsorption process. The results study leads to the selected design proposed as this project solution. The analysis of the model solutions can be divided into two phases. The first one compares the performance of the models themselves. The second part discusses the conclusions derived from evaluating the modifications applied to the adsorbent shape, cooling system and aspect ratio.

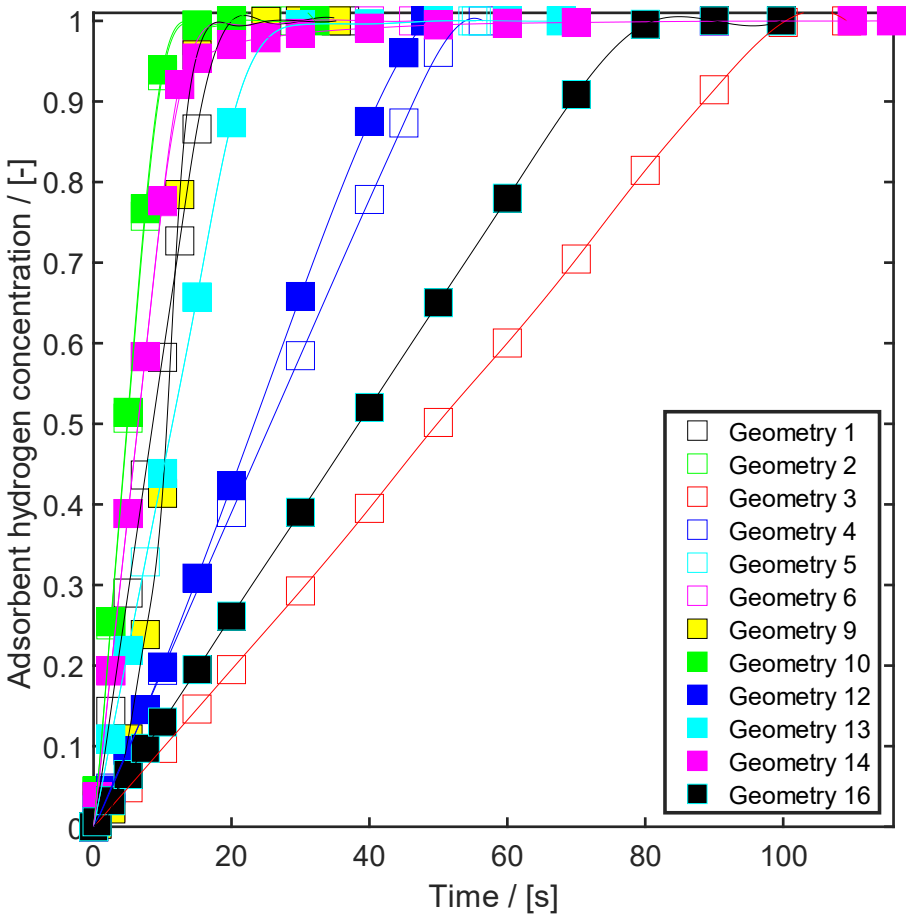

Figure 15: Comparison of the average hydrogen saturation level during the tank filling process in the adsorbent in the twelve geometries simulated in this project. The hydrogen loading in the material ranges from zero to one, where zero means that the adsorbent is empty, and one means that the adsorbent is fully saturated. The geometries represented

are a) Geometry 1-black squares with white filling, b) Geometry 2-green squares with white filling, c) Geometry 3-red squares with white filling, d) Geometry 4-blue squares with white filling, e) Geometry 5-cyan squares with white filling, f) Geometry 6-pink squares with white filling, g) Geometry 9-black squares with yellow filling, h) Geometry 10-green squares, i) Geometry 12-blue squares, j) Geometry 13-cyan squares k) Geometry 14-pink squares, l) Geometry 16-cyan squares with black filling.

As expected in Figure 15, these smaller tanks have lower filling times. This decrement is because the inlet was standardised for the alternative designs. Therefore, the entering mass flow is equal, and the total saturation of the adsorbent is lower due to the larger tank volume. This statement has the exception of geometry 14, which, despite being designed to be positioned vertically and consequently having a smaller size, takes the longest to complete the saturation of the adsorbent. This case is due to the combination of higher kinetics in the initial filling stages and more adsorbent volume, causing the adsorbent to release considerably more heat than the geometry that does not install the external jacket. Subsequently, this scenario slows down the adsorption of hydrogen due to the increase in temperature in the tank, which raises the total filling time of the tank compared to the geometry that does not install the external jacket, reaching the extreme case of having a filling time up to 3 times longer (comparison of geometry 5 and 14). Then, the plots shown in Figure 15 illustrate that the design proposed for vertical positioning in the container, which has the shortest filling time, is number two. While number 16 is the one that takes the shortest time and is positioned horizontally in the tank.

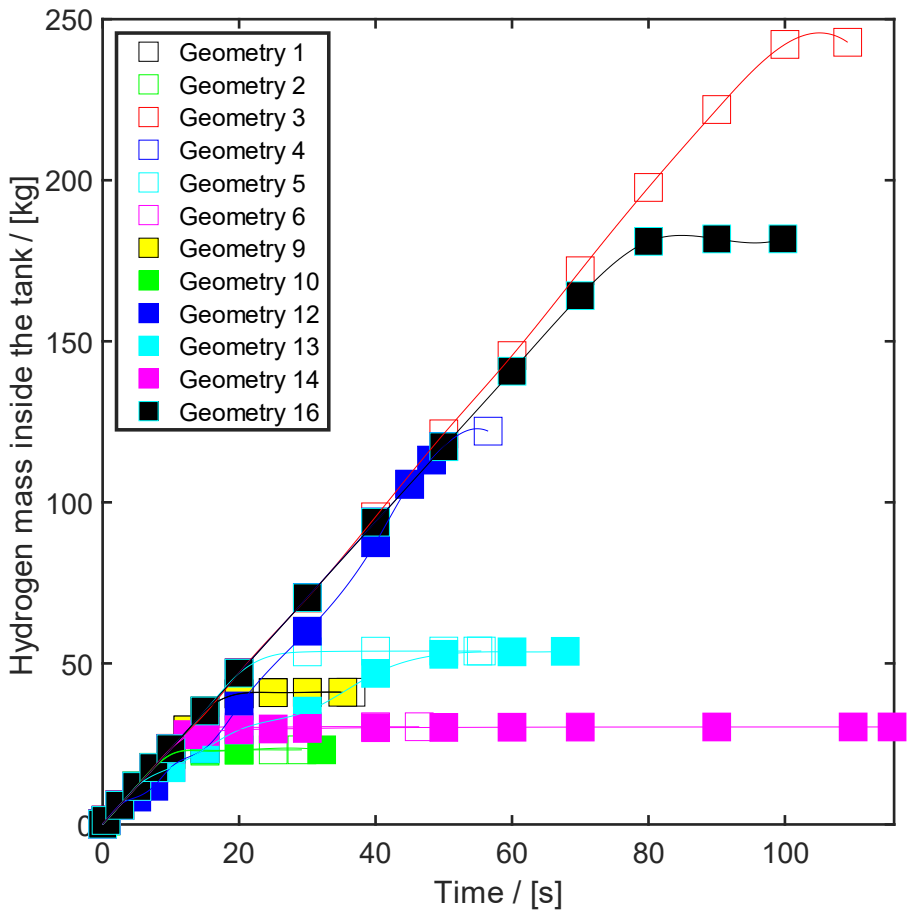

Figure 16: Comparison of the mass of hydrogen in the tank during the charging process of the tank in the adsorbent in the eleven geometries simulated in this project. The initial mass in the tank is different due to the volume not occupied by the adsorbent in each geometry. The final square indicates the total amount of hydrogen stored in the tank. The eleven geometries represented are a) Geometry 1-black squares with white filling, b) Geometry 2-green squares with white filling, c) Geometry 3-red squares with white filling, d) Geometry 4-blue squares with white filling,

e) Geometry 5-cyan squares with white filling, f) Geometry 6-pink squares with white filling, g) Geometry 9-black squares with yellow filling, h) Geometry 10-green squares, i) Geometry 12-blue squares, j) Geometry 13-cyan squares k) Geometry 14-pink squares, l) Geometry 16-cyan squares with black filling.

The results plotted in Figure 16 show a linear relationship between the adsorbent volume and the hydrogen mass stored, independently of the shape. Therefore, we can affirm that the adsorbent shape influences the kinetics of the process but not its total capacity, which is related to the total volume of the material. Design two has the lowest hydrogen storage capacity, and design three has the highest capacity, 23,168 and 242.82 kg. However, we can infer without having the results that geometry 7 and 15 would have the highest hydrogen capacity as they have the highest adsorbent volume. The ratio between the amount of hydrogen stored is equal to the ratio between the volume of adsorbent in both tanks.

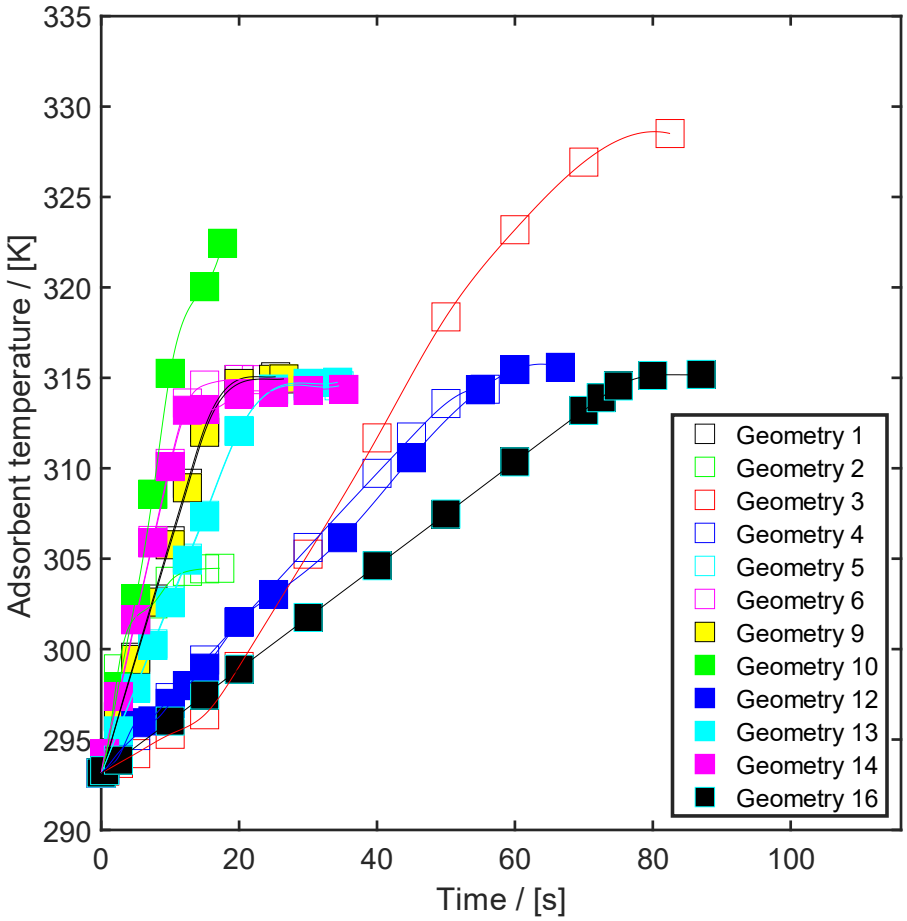

Figure 17: Comparison of the adsorbent temperature during the charging process of the tank for the eleven geometries simulated in this project. The initial temperature for all the scenarios is 293.15K. The final square indicates the adsorbent temperature at the end of the adsorption. The eleven geometries represented are a) Geometry 1-black squares with white filling, b) Geometry 2-green squares with white filling, c) Geometry 3-red squares with white filling, d) Geometry 4-blue squares with white filling, e) Geometry 5-cyan squares with white filling, f) Geometry 6-pink squares with white filling, g) Geometry 9-black squares with yellow filling, h) Geometry 10-green squares, i) Geometry 12-blue squares, j) Geometry 13-cyan squares k) Geometry 14-pink squares, l) Geometry 16-cyan squares with black filling.

Figure 17 shows the evolution of the adsorbent temperature during the hydrogen adsorption process. First, this plot shows that the final material temperature of Geometry 3 is the highest of all simulated scenarios, as it stores the maximum hydrogen amount. This maximal hydrogen adsorption implies that it generates a superior amount of heat. Furthermore, by analysing the behaviour of the different models, two points can be highlighted to improve the design

performance. First, if we compare two homologous geometries with and without an external jacket (geometry 3 and 10), we can observe how the installation of the jacket accelerates reaction kinetics. Although, despite the installation of an extra cooling system, the maximum temperature reached is higher due to the faster adsorption. Second, if we want to analyse the impact of the external jacket on larger tanks' performance, geometries 3 and 16 should be observed. After 40 seconds of filling, it can be seen in Figure 15 that the hydrogen load in the adsorbent is higher in geometry 16 by approximately 10%. Next, looking at Figure 16 at this instant, it can be observed that the amount of mass inside the tank is similar. However, in Figure 17, the adsorbent temperature is approximately 10 K lower in the model that installs the jacket. Therefore, by combining the information obtained with these scenarios comparison, it can be inferred that the influence of the external refrigeration in small tanks could be counter-productive due to the increment in the heat generation by hydrogen adsorption. Even though, in larger tanks, the installation of this cooling method could considerably reduce the temperature of the material, making the increment temperature of the material 41.3% smaller.

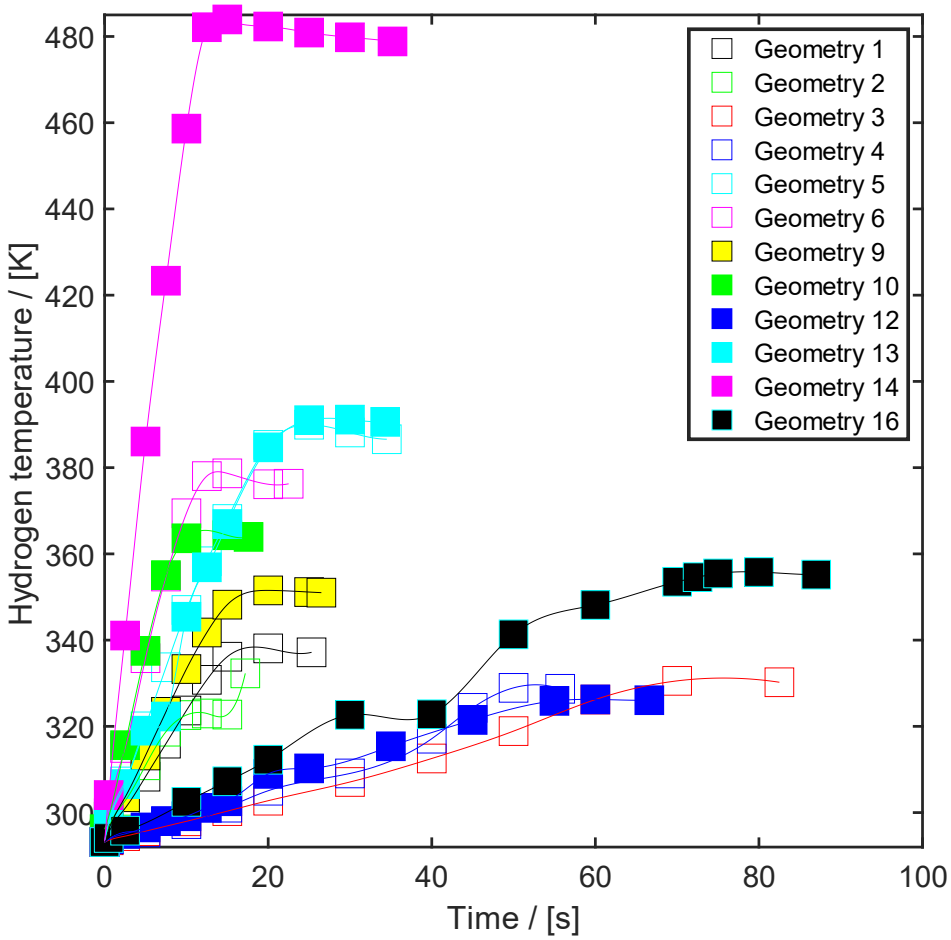

Figure 18: Comparison of the hydrogen temperature during the charging process of the tank for the eleven geometries simulated in this project. The initial temperature for all the scenarios is 303K. The final square indicates the hydrogen temperature at the end of the adsorption. The eleven geometries represented are a) Geometry 1-black squares with white filling, b) Geometry 2-green squares with white filling, c) Geometry 3-red squares with white filling, d) Geometry 4-blue squares with white filling, e) Geometry 5-cyan squares with white filling, f) Geometry 6-pink squares with white filling, g) Geometry 9-black squares with yellow filling, h) Geometry 10-green squares, i) Geometry 12-blue squares, j) Geometry 13-cyan squares k) Geometry 14-pink squares, l) Geometry 16-cyan squares with black filling.

In illustration 18, the highest temperature reached in hydrogen is in model 14. Comparing this geometry with its counterpart that does not install an external jacket, the only difference

between geometry 6 and 14 is the speed at which this reaction is given. Therefore, we can state that the heat transfer from the material to the gas greatly influences the gas temperature, doubling in this comparison, the temperature increase in the gas. Additionally, if we analyse the pairs of analogous designs with different diameters, a higher increase in hydrogen temperature is observed in these layouts with a smaller diameter for the small length designs, as the gas available volume is smaller. However, in the larger tanks, the difference in the final gas temperature is imperceptible, as is the case in geometry 3 and 4.

Then, the selected geometry is number three as it has the highest hydrogen capacity, the filling time is low, the round trip efficiency is higher than its homologous that installs an external jacket, its adsorbent shape improves the desorption kinetics compared to Geometry number seven, and this geometry allows doubling the number of installed tanks in the container compared to its homologous design which installs external refrigeration due to the space constraints.

To conclude this segment, we dive into how each modification affects the tank's performance. First, if we analyse the shape of the adsorbent, as expected, cylindrical adsorbent has a higher capacity and slower kinetics since the torus stack of adsorbents has more contact surface. On average, on cylindrical reactors, we see an increment in the hydrogen capacity of 31% and the adsorption process was 55% slower. Additionally, it was observed that the final saturation on the cylindrical adsorbent was more lagging due to inferior surface contact with the gas. Therefore, equalling the adsorbent volume, a stack of torus adsorbents performs better than a cylindrical host. Second, analysing the results obtained for homologous layouts with different Aspect ratios (AR), the same behaviour described in the literature is observed, where designs with higher AR have a faster adsorption process [125]. Third, the external jacket installation has been shown to accelerate the kinetics in the early stages of adsorption reaction. However, this increase in the rate of hydrogen load in the adsorbent can slow down the adsorption process due to the heat generated in this exothermic process. In addition, a more significant influence of this system on the system's temperature has been observed in larger tanks. Although, this technique would reduce the overall efficiency of the assembly and its weight capacity to store hydrogen due to the mass added to the system.

4.3.2. Desorption

This section presents the results obtained in the desorption process for geometry 3, shown in Annex A, under the conditions listed in section 3.2.6. Desorption configuration.

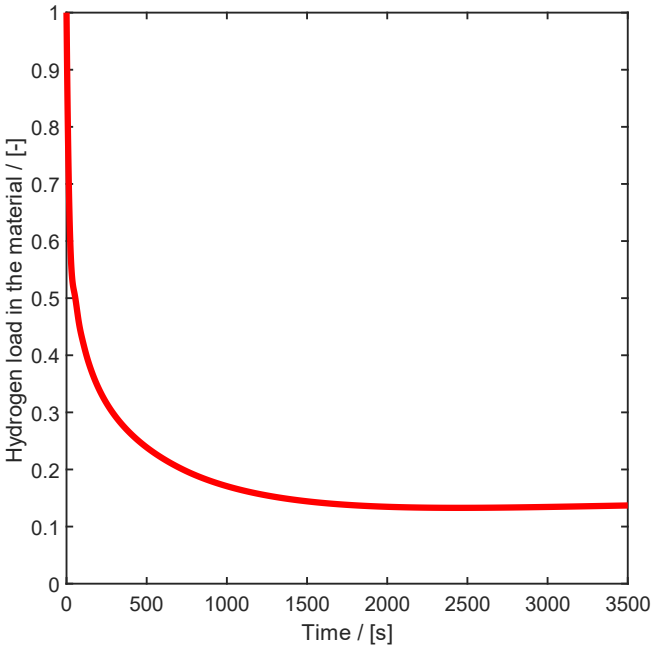

Figure 19: Hydrogen load during the desorption process for geometry three under the conditions described in section 3.2.6. for 3500 seconds. The red line represents the average hydrogen concentration in the adsorbent.

Figure 19 illustrates the hydrogen load on the host during the desorption process. It can be seen in this plot how the hydrogen release during the first 250 seconds is fast, being gradually slowed down by the adsorbent temperature decrease to be stabilised later at a hydrogen load of 0.136. The steady state is achieved at 1870 seconds of the simulation. If this value is compared with the validation scenario, this design discharges 14.47% more than the verification model. This superior desorption value is a consequence of the preheating system and the higher AR of the selected layout, thus improving the kinetics of the reaction. Then, the hydrogen mass extracted from the tank is 210.91 kg and takes 5840.02 seconds to release.

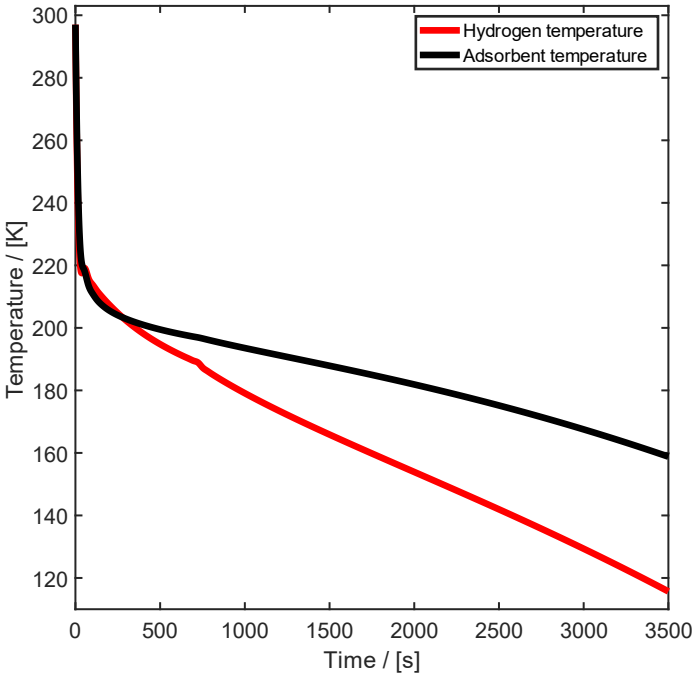

Figure 20: Hydrogen and adsorbent temperatures during the desorption process for geometry three under the conditions described in section 3.2.6. for 3500 seconds. The red line represents the hydrogen temperature in the tank, and the black line illustrates the average adsorbent temperature in the material. Both domains have an initial temperature of 297K.

Figure 20 shows the hydrogen and adsorbent temperature evolution in the hydrogen release process. Both temperatures drop drastically in the first 100 seconds due to the abrupt hydrogen desorption that requires a large amount of energy to be produced and the compression of hydrogen that occurs after the expulsion of hydrogen from the adsorbent and its displacement to the free volume occupied by the rest of the hydrogen. Once the first decrease in gas temperature has occurred, the temperature decrement is almost linear. This trend is observed by the compensation of the hydrogen removal and the hydrogen leaving the adsorbent. The material cools down due to the energy requirement for hydrogen desorption.

4.4. Comparison with current solutions

After studying the solutions mentioned in section 1.3, the most similar and the one whose comparison would be logical due to its target niche, implementation, boundary conditions, and design would be the solution installed in the H2 Barge 1 prototype. First, this prototype stores 450 kg of hydrogen per container compressed at 300 bar [159]. Then, looking at the simulated geometries, this hydrogen capacity per container can be improved considering the container volume restrictions. However, this solution would exceed the maximum container load. With the use of Lanthanum nickel as an adsorbent, it would not be possible to improve the H2 Barge 1 solution without exceeding the maximal container load, i.e. we can state that in the same volume, the system designed in this project would store more hydrogen, but the total weight would be higher. Hence, to achieve the 450 kg of stored hydrogen with a maximum container load of 26740 kg, the adsorbent capacity should be doubled, or the adsorbent density should be reduced to half.

Second, comparing the efficiency of both solutions, it is known from the literature that the efficiency of compressed hydrogen storage systems is between 90-84.5% for systems at 200-800 bar[158]. Therefore, compared with the result obtained following the methodology proposed in section 3.5, the proposed solution efficiency is 44.3%. The inability of the adsorbent to release all of the hydrogen stored reduces the system's overall efficiency.

Chapter 5: Ideal gas simplification influence

This section focuses on the impact of the non-ideal gas model for hydrogen on the main variables influencing the solid hydrogen storage simulation. This chapter covers the code methodology used for this analysis and the results obtained. This estimation has been added as an extra chapter to the project because it is considered a point neglected in the literature that could have a remarkable impact on the storage model. However, solid hydrogen storage with a non-ideal gas behaviour could not be accomplished as a new model was required, and no time was available to develop it.

5.1. Methodology

This section sets out the code used to study how the ideal gas simplification impacts the parameters that influence the solid hydrogen model. For this purpose, we research how this simplification affects C_p, C_v, internal energy, isentropic exponent *and* mass flow. The working conditions and design parameters used in this section replicate the set-up studied by Bao et al. [86]. Matlab®[159] and CoolPROP® [160] are used for this analysis.

5.1.1. C_p, C_v and isentropic exponent analysis

First, to study the ideal gas assumption impact on C_v and C_p, a Matlab loop was performed with an initial temperature of 300K and increasing up to 700K, as this is the most common range of operation of the adsorbent materials. Additionally, three different pressures were defined to study how real gas behaviour changes under rising pressure. Next, for the ideal gas scenario, C_p and C_v were chosen as CoolProp reference values and compared with the values extracted from CoolProp by fixing five increasing pressures (0.1, 10, 30, 60, and 90MPa) and including the temperature increase from 300 to 700K. Moreover, to compute these scenarios, the command py.CoolProp.CoolProp. in Matlab was used to access CoolProp through a Python library, as CoolProp and Matlab do not have a direct link.

Second, how ideal gas simplification affects the isentropic exponent is analysed. Ideal gases only have one isentropic exponent due to the assumption nature. Although real gases have three isentropic exponent forms, these are corrected values of the isentropic exponent based on the gas behaviour. The isentropic exponent used in this project is γ_{Pv}. γ_{Pv} is a corrected isentropic exponent in the *Pv* diagram [161]. This isentropic exponent is rectified in low-density gases, such as hydrogen, which are much more compressible than other fluids with higher density [161]. Moreover, the γ_{Pv}derivation can be found in the Nederstigt, P. [161] report.

The isentropic exponent for the ideal gas assumption is calculated as the ratio between the reference state C_p and C_v (equation 23).

$$\gamma_{Pv} = \frac{C_P}{C_v} \tag{23}$$

Then, the γ_{Pv}using the Peng-Robinson equation of state is obtained by a Matlab loop ranging from 300-670K. This temperature range and the reference model working conditions define the hydrogen pressure using the Peng-Robinson EOS. Finally, the γ_{Pv} value is computed by the isentropic exponent definition, see equation 24.

$$\gamma_{Pv} = -\frac{v_{moc}}{P}\frac{C_\rho}{C_v}\left(\frac{\partial P}{\partial v}\right)_T$$

(24)

where $v_{moc}$is the molecular volume [m^3mol^{-1}].

Moreover, a second definition calculates the γ_{Pv} value from CoolPROP data. This equation depends on gas state definition variables, which can be obtained from CoolPROP. Then, the compressibility factor derivative is approximated to the quotient between increments to calculate the γ_{Pv} value. Finally, the isentropic exponent is calculated by extracting the compressibility factor at the defined temperatures at constant pressure and volume from CoolPROP.

$$\gamma_{Pv} = \frac{C_\rho}{C_v}\left[\frac{Z + T\left(\frac{\partial Z}{\partial T}\right)_P}{Z + T\left(\frac{\partial Z}{\partial T}\right)_v}\right]$$

(25)

being Z the compressibility factor [-].

5.1.2. Internal energy analysis

This section presents a Matlab code executed to analyse the implicit error obtained by calculating the hydrogen temperature through the internal energy under the ideal gas assumption. The run loop started at $2701 \cdot 10^6$ J kg^{-1} as the initial internal energy value and had a maximum of $6300 \cdot 10^6$ J kg^{-1}.

First, the CoolProp C_v reference state was used to calculate the temperature, assuming hydrogen as an ideal gas to equal the initial state of the comparison and avoid mismatches at the reference state that can induce errors in the results. Then, equation 8 computed the hydrogen temperature. In this way, the temperature obtained with this simplification is calculated for different values of the internal energy, replicating what executes the model.

Second, the internal energy definition and the Peng-Robinson EOS calculate the hydrogen temperature by looping the internal energy and the reference model working parameters. Finally, the following equation allows us to obtain the temperature using internal energy as the only variable.

$$du = C_v\, dT - \left[P - T\left(\frac{\partial P}{\partial T}\right)_V\right] dV$$

(26)

$$A = \left(a^2 M^2 \operatorname{atan}\left(\frac{b\,M + V}{\sqrt{2}\,b\,M}\right)\right)^2$$

(27)

$$B = 2\sqrt{2}\; a\; C_v M\; \operatorname{atan}\left(\frac{b\,M + V}{\sqrt{2}\,b\,M}\right)$$

(28)

$$T_1 = \frac{A\,k^4}{b^2 T_{crit}} + \frac{2\,A\,k^3}{b^2 T_{crit}} + \frac{A\,k^2}{b^2 T_{crit}} + \frac{B\,k^2}{b} + \frac{2\,B\,k}{b} + 4\,(u - u_0)\,C_v + C_v^2 T_0 + \frac{B}{b}$$

(29)

$$T_2 = T_1^2$$

(30)

$$T_3 = \frac{8C_v^2}{b}\left(\frac{A\,k^4}{b^2} + \frac{2\,A\,k^3}{b^2} + \frac{3\,A\,k^4}{b^2} + \frac{B\,(u-u_0)}{b} + \frac{B\,T_0}{b} + \frac{2\,A\,k^3}{b^2} + \frac{2\,B\,k\,(u-u_0)}{b} + \frac{2\,B\,T_0}{b} + 2\,(u-u_0)^2 + 2\,C_v^2 T_0 + \frac{A}{b^2} + 4\,(u-u_0)\,C_v T_0 + \frac{B\,(u-u_0)}{b} + C_v\,T_0\,B\right)$$

(31)

$$T = \frac{T_1 - \sqrt{T_2 - T_3}}{T_4}$$

(32)

where a is the Peng-Robinson value, b is a Peng-Robinson parameter, k is the substance constant characteristic, u is the internal energy [J kg^{-1}], T is the hydrogen temperature[K], and $u_0$is the reference state internal energy [J kg^{-1}].

Being *a* defined as: $a = 0.45724\,\frac{R^2\,T_c^2}{P_c}$ [kg m^{4}s^{-2}mol^{-2}].

where T_{crit} is the hydrogen critical temperature [K] and $P_{crit}$is the hydrogen critical pressure [Pa].

Then, *b* is calculated using the following equation:

$$b = 0.7780\,\frac{R\,T_c}{P_c}\ [\text{m}^3\text{s}^{-1}\text{mol}^{-1}].$$

Finally, the *k* is defined as: $k = 0{,}37464 + 1{,}54226\omega - 0{,}26992\omega^2$. Where ω is the acentric factor.

Third, to obtain the CoolProp temperature value, the PR EOS was used to calculate the gas pressure, as this program requires two inputs to compute the temperature. Then, using the `py.CoolProp.CoolProp.` command, the temperature was obtained by inserting the predefined internal energy and previously calculated pressure. CoolProp uses Peng-Robinson to calculate some properties, so the error induced by this auxiliary calculation using the PR EOS to compute the pressure is considered negligible.

5.1.3. Mass flow comparison

This final section studies the ideal gas simplification influence on mass flow. This analysis was researched using a Matlab loop, which started at the initial tank pressure and went up to the reservoir pressure. This code simulated two reservoir pressures of 2.6MPa and 26MPa to analyse how this simplification behaved when increasing the pressure.

First, for the hydrogen filling mass flow calculation as an ideal gas, equations 2 and 3 were used, together with the C_p, C_v and γ calculated in this section.

Second, to calculate the hydrogen mass flow as a real gas using CoolPROP, the process described in segments 5.1.1 and 5.1.2 was repeated to obtain C_p, C_v, and γ_{Pv} using CoolPROP. Then, the Nederstigt, P. [161] equation computed the Mach number under the working conditions (Equation 33). Its value was restricted to values less than or equal to 1.

$$Ma = \frac{\sqrt{2}\, P_R \left(\frac{P_R}{P_c}\right)^{\sqrt{-1/\gamma_{Pv} - P_c}}}{\sqrt{\gamma_{Pv}\, P_c - P_c}}$$

(33)

being Ma the Mach number [-].

Finally, the following expression computed the mass flow. The equations shown below were derived using the work of Nederstigt, P. [161] as starting point.

$$\dot{m} = A_{Orif}\, \rho_n\, v_n$$

(34)

where $[161]$ is the inlet mass flow [kg s^{-1}] and $\rho_n$is the hydrogen density at the nozzle [kg m^{-3}], defined as:

$$\rho_n = \frac{\rho_R}{1 + Ma^2 \left(\frac{\gamma_{Pv} - 1}{2}\right)^{\frac{1}{\gamma_{Pv} - 1}}}$$

(35)

Where v_n is the hydrogen velocity at the nozzle [m s^{-1}]. It is calculated by the following equation:

$$v_n = \frac{c_0 Ma^2}{1 + Ma^2 \cdot \left(\frac{\gamma_{Pv} - 1}{2}\right) \sqrt{\frac{\gamma_{Pv} + 1}{2}} \sqrt{\frac{2}{\gamma_{Pv} + 1}}}$$

(36)

being $c_0$the stagnation velocity [m s^{-1}], defined as:

$$c_0 = \sqrt{\frac{\gamma_{Pv} + P_R}{\rho_R}}$$

(36)

5.1.4. Matlab code set up

This segment contains the code configuration used to analyse the influence of the gas definition on the different parameters that have a remarkable impact on the model behaviour.

5.1.4.1. C_p, C_v and isentropic exponent code parameters

Table 12: Parameters definition for studying the ideal gas assumption impact on the Cp, Cv and isentropic exponent.

Symbol	Value
$C_{p\ ideal\ gas}$	14550 J kg^{-1} K^{-1}
$C_{v\ ideal\ gas}$	10330 J kg^{-1} K^{-1}
T_0	300 K
T_{final}	700 K
ΔT	7 K
P_{R1}	0.1 MPa
P_{R2}	30 MPa
P_{R3}	90 MPa

5.1.4.2. Internal energy

Table 13: Parameters definition for analysing the ideal gas assumption influence on the internal energy calculation.

Symbol	Value
w	-0.21869
T_{crit}	32.893 K
P_{crit}	1.3 MPa
R	8.314 J mol^{-1} K^{-1}
M	0.002 kg mol^{-1}
T_0	298.15 K
$C_{v\ ideal\ gas}$	10330 J kg^{-1} K^{-1}
u_0	2701.3 MJ kg^{-1}
u_f	6300 MJ kg^{-1}
V	$12 \cdot 10^{-5}$ m^3

5.1.4.3. Mass flow

Table 14: Parameters definition for studying the ideal gas assumption influence on the inlet hydrogen mass flow.

Symbol	Value
w	-0.21869
T_{crit}	32.893 K
P_{crit}	1.3 MPa
R	8.314 J mol^{-1} K^{-1}
M	0.002 kg mol^{-1}
$C_{p\ ideal\ gas}$	14550 J kg^{-1} K^{-1}
$C_{v\ ideal\ gas}$	10330 J kg^{-1} K^{-1}
T_R	297 K
P_{R1}	2.6 MPa
P_{R2}	26 MPa
P_0	0.13 MPa
ΔP	0.001 MPa
V	0.11 m^3

5.2. Results

This section compares the results obtained for the previously mentioned variables under the assumption of hydrogen as a real and an ideal gas under the defined working conditions. The methodology followed for this study is described in subsection 5.1. The results' presentation has been divided into three fields. These are the thermodynamic properties of the gas, internal energy and mass flow. The reference results for the error percentages and the most accurate values are the data extracted from CoolPROP.

5.2.1. C_p, C_v and isentropic exponent results

This section presents the results obtained from the Matlab code that compares the gas heat properties behaviour under working conditions for an ideal and non-ideal gas.

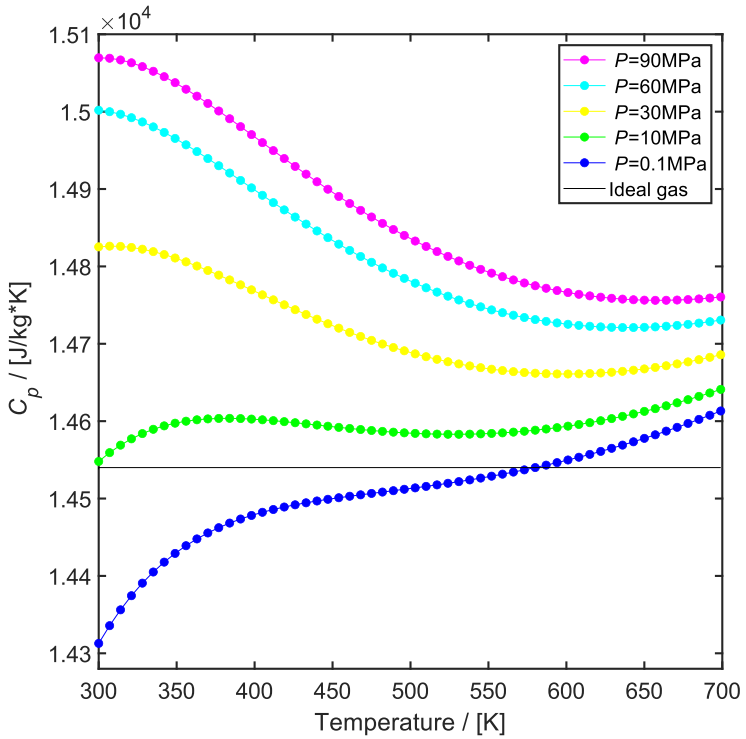

Figure 21: Comparison between the Cp results assuming ideal gas (black line) and the results obtained by the real gas definition code described in Chapter 5. For the cases of a) hydrogen pressure of 0.1MPa and a temperature range of 300-700K - blue dotted line, b) hydrogen pressure of 10MPa and a temperature range of 300-700K - yellow dotted line, c)hydrogen pressure of 30MPa and a temperature range of 300-700K - purple dotted line, d) hydrogen pressure of 60MPa and a temperature range of 300-700K - green dotted line, and e)hydrogen pressure of 90MPa and a temperature range of 300-700K - cyan dotted line.

Figure 21 shows C_p behaviour by comparing non-ideal and ideal gas models. This figure includes six lines: the constant C_p value depicted in black shows the ideal gas scenario, and the rest considers real gas behaviour at increasing pressures ranging from 0.1-90MPa and evolving from 300-700K. For the real gas scenarios, the C_p value increases with pressure and decreases with temperature for pressures above 30 MPa, while it increases with temperature for values of 0.1 and 10 MPa. The error in the C_p when considering hydrogen as an ideal gas for these scenarios analyzed is less than 3.5%.

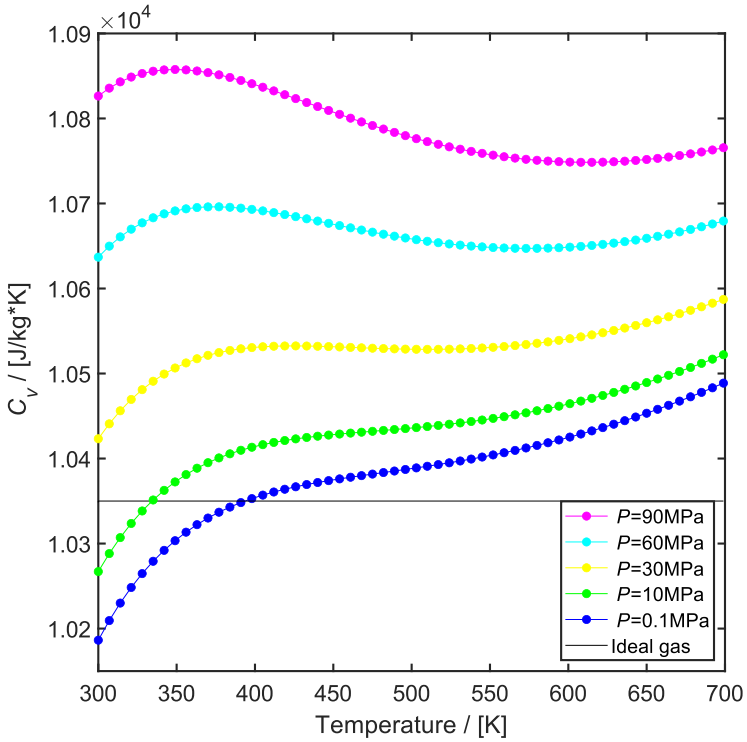

Figure 22: Comparison between the C_v results assuming ideal gas (black line) and the results obtained by the real gas definition code described in Chapter 5. For the cases of a) hydrogen pressure of 0.1MPa and a temperature range of 300-700K - blue dotted line, b) hydrogen pressure of 10MPa and a temperature range of 300-700K - yellow dotted line, c)hydrogen pressure of 30MPa and a temperature range of 300-700K - purple dotted line, d) hydrogen pressure of 60MPa and a temperature range of 300-700K - green dotted line, and e)hydrogen pressure of 90MPa and a temperature range of 300-700K - cyan dotted line.

Figure 22 represents the C_v error due to assuming hydrogen as an ideal gas. This illustration contains six curves, where the black line represents the ideal gas assumption with a constant C_v value, and the remaining curves depict hydrogen as a real gas under varying pressures from 0.1 to 90 MPa and temperatures increasing from 300 to 700 K. As for C_p, in the case of the real gas scenarios, the C_v value shows an upward trend with increasing pressure and a downward trend with increasing temperature for pressures exceeding 30 MPa. However, the C_v value increases at rising temperatures for pressures of 0.1 and 10 MPa. In this case, the maximum error of this simplification for the collected plots is less than 5%.

Figure 23 illustrates the gamma behaviour of hydrogen as an ideal gas and real gas at three pressures (0.1, 30 and 90 MPa). The difference between the real and ideal gas results is negligible for 0.1 MPa result and increases with rising temperature. However, as the pressure increases, this difference increments and this error decreases as the hydrogen temperature increases, showing the opposite behaviour to the lower-pressure results. Therefore, for adsorbents working at temperatures close to room temperature and high pressures, the error induced by this simplification for computing gamma could be close to 37%. Moreover, a good correlation is observed between the results obtained using the EOS PR and the experimental data extracted from CoolPROP.

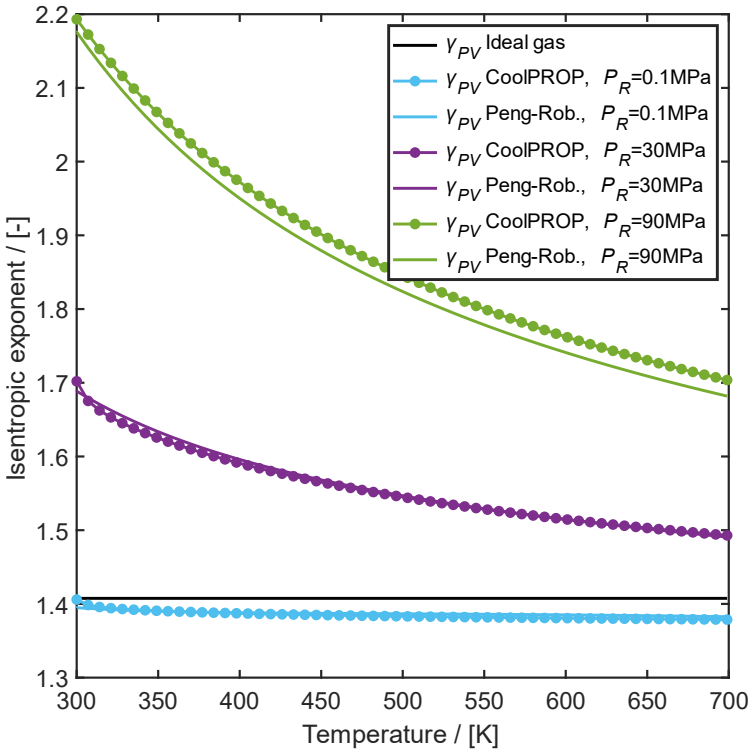

Figure 23: Comparison between the values of the isentropic exponent corrected for pressure and volume assuming that this is an ideal gas (black line) and the results obtained by the code described in chapter 5, for the cases of a) hydrogen pressure of 0.1MPa and a temperature range of 300-700K, computed by PR EOS - blue line, b) hydrogen pressure of 0.1MPa and a temperature range of 300-700K, computed by CoolProp- blue line and dots, c) hydrogen pressure of 30MPa and a temperature range of 300-700K, computed by PR EOS - purple line, d) hydrogen pressure of 30MPa and a temperature range of 300-700K, computed by CoolProp- purple line and dots, e) hydrogen pressure of 90MPa and a temperature range of 300-700K, computed by PR EOS - green line, and f) hydrogen pressure of 90MPa and a temperature range of 300-700K, computed by CoolProp- blue line and dots.

5.2.2. Internal energy

This section exposes the results obtained by computing the temperature of hydrogen through its internal energy, assuming that it is an ideal and real gas.

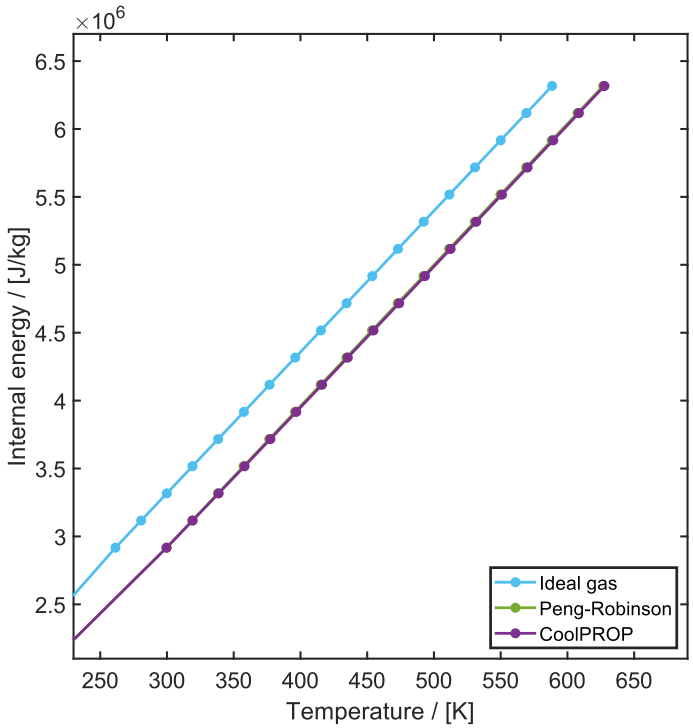

Figure 24: Hydrogen temperature results using the internal energy of hydrogen, considering the following scenarios: a) ideal gas - blue dotted line, b) real gas calculated using PR EOS- green dotted line, and c) real gas computed by CoolProp-purple dotted line.

Figure 24 contains three scenarios. They represent hydrogen as an ideal and real gas (the PR EOS and CoolPROP were used to calculate the real gas temperature). The results obtained using the PR EOS and CoolPROP highly converge. These methods' results difference was close to 0.1%. However, the ideal gas result had an error of up to 13% compared to non-ideal gas results, and this difference is approximately constant for all the temperature ranges.

5.2.3. Mass flow

This section presents the results obtained from the simulation run with a Matlab code that compares the mass flows assuming hydrogen as an ideal and real gas using different methodologies. In this simulation, the error of computing the hydrogen temperature by the internal energy is not included, as the code did not simulate the heat transfer module, only the mass flow equation.

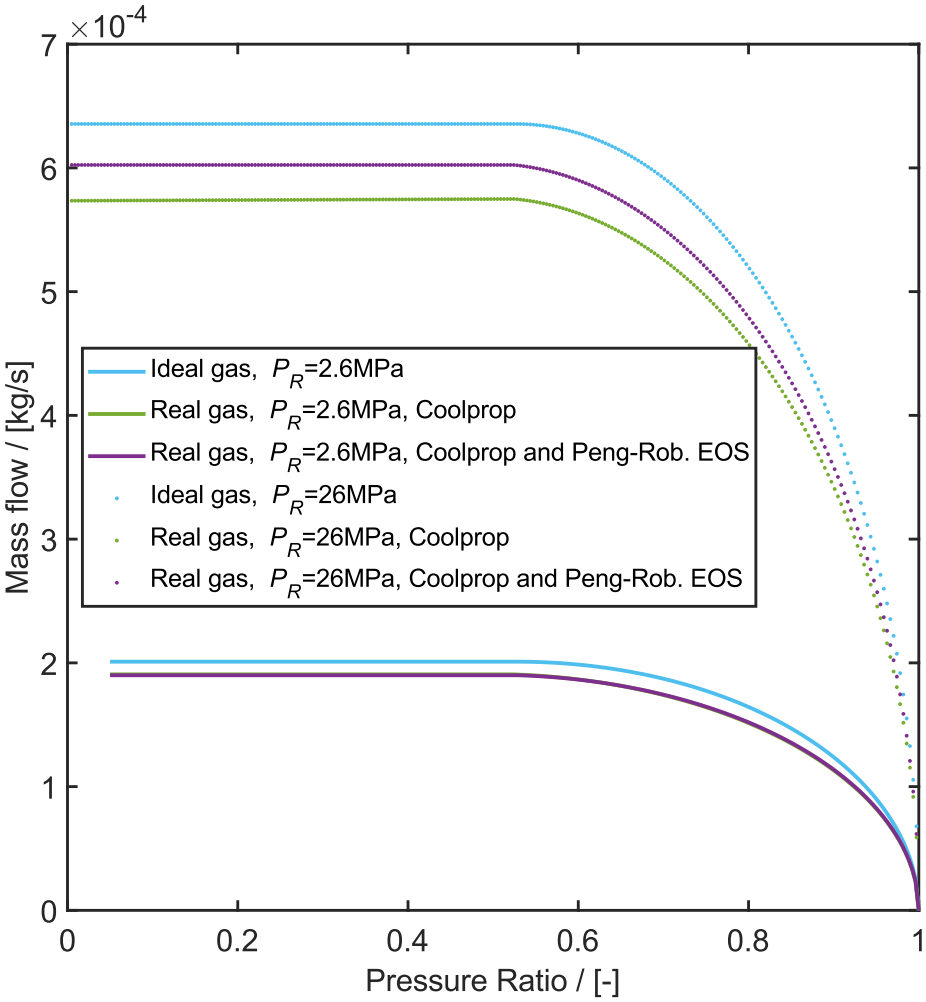

Figure 25: Mass flow results in reference to the pressure ratio, considering the following scenarios: a) ideal gas at 2.6 MPa - blue line, b) real gas calculated using PR EOS at 2.6 MPa- green line, c) real gas computed by CoolProp at 2.6 MPa-purple line, e) ideal gas at 26 MPa - blue dots, f) real gas calculated using PR EOS at 26 MPa- green dots, and g) real gas computed by CoolProp at 26 MPa-purple dots.

This figure shows the hydrogen mass flow entering the tank as a function of the given pressure ratio between the tank and the reservoir pressure. This figure shows two cases for filling pressures at 2.6 and 26MPa using three alternatives for calculating the hydrogen properties. Then, two approaches define real gas scenarios, using CoolPROP and combining CoolPROP and the Peng-Robinson EOS.

First, at a reservoir pressure of 2.6MPa, it is observed that the results obtained for the two real gas variants are exceptionally close, with a maximum difference between the two values of 1%. However, if we compare the results obtained with the ideal gas simplification, the error increases to 5%.

Second, for the 26MPa pressure, there is a noticeable difference between the three scenarios, with the ideal gas being the furthest away from the CoolPROP. There is a maximal error close to 10.84%. In contrast, the Peng-Robinson EOS gives a more accurate result, with a maximum error of 5.2%.

Chapter 6: Conclusions

This section summarises the critical results obtained in this project, connects the findings of chapters four and five, highlights this project's key findings, and includes the limitations of this work. This segment elaborates on the results and conclusions drawn in each section in the order presented in this report.

First, the validation model analysis proved that the hydrogen non-flow simplification in the tank gives good results, closely matching other models and experimental data. This project employs an equation that simulates the reaction kinetics without adapting it to experimental data to ensure accuracy. Therefore, it can be expected that the results obtained by the Jemni et al. [150] model would be closer to experimental data than the one presented in this report, as they use a semi-empirical equation fitted for lanthanum nickel at the specific working condition in their project. The sharper behaviour observed in the reaction on the validation results could be a consequence of either the non-flow simplification, the use of a different kinetics reaction equation, or both. Although, the hydrogen load behaviour of the Jemni et al. [150] model is closer to the experiment, the final adsorbent saturation and emptying time results given by our model are more accurate than the Jemni et al. model [150]. Therefore, we can expect lower reaction kinetics in a future prototype compared to the model speed reaction. Upon analyzing the meshing for the validation scenario, it was observed that larger meshes proved to have more accurate results than smaller meshes. This unexpected mesh result could be because, for inferior mesh sizes, the transition between the quadratic grid and the triangular mesh reduces the local mesh quality, decreasing the results' accuracy. As described in section 3.2, all the parameters which described the fitting were higher for the cases of a lower mesh size.

Second, this project has been limited by the materials available to be simulated as adsorbent. As discussed in section 4.2, MgH_2 cannot be implemented under similar working conditions to other hydrogen storage methods, as it requires preheating to trigger the hydrogen adsorption, making the system significantly more energy intense and hinders its subsequent desorption. Furthermore, as discussed in section 4.3, the $LaNi_5$ use may not improve compressed hydrogen within a maximum mass limit container. However, by only considering the volume restriction, the proposed solution can potentially store up to 841 kg, doubling the amount of hydrogen stored at 300 bar by the H2 Barge 1 prototype. Therefore, to improve the current solutions using the geometry three described in this project, a material would be required which, with all other parameters equal to $LaNi_5$, would have half the density or double the capacity. Nevertheless, it has been demonstrated that it is possible to design systems in working conditions similar to compressed hydrogen that improve this solution.

Third, the simulation of the alternative geometries designed in this project has made it possible to research the influence of combining internal and external cooling systems, the shape of the adsorbent and the tank AR. Summarizing the external jacket's impact on the tank performance, the following observations can be highlighted: The installation of this cooling technique has improved the adsorption rate of hydrogen in the material in the early stages of this process, however, in some configurations, it has been marked that this improvement in the adsorption rate has led to a higher heat release, which has increased the system's temperature and slowed down its saturation reaction, this consideration was not found in literature; in addition, it has been observed that the external jacket has a superior impact on system temperature in designs with a higher AR and larger size; next, continuing with the adsorbent shape, it was observed that reactors with a larger surface area had faster reaction kinetics, in agreement with the literature

review findings of chapter two of this report; it was also noticed that the adsorbent volume is the main factor that determines the total amount of hydrogen stored; finally, it was confirmed that designs with a higher AR performed better than those with a lower AR, again in line with the papers reviewed during this project.

Fourth, after comparing the total efficiency of the system designed in this project and the solution installed in H2 Barge 1, it was observed that the solid hydrogen efficiency is considerably lower compared to compressed hydrogen. In both the verification scenarios and simulation of the proposed final solution, a considerable amount of hydrogen, 24% and 13%, respectively, remain in the adsorbent. Therefore, reducing the percentage of hydrogen that is not desorbed would notably improve this efficiency. Equation 24 suggests that more mass extracted from the tank is translated into an increase in the efficiency.

Examining the results obtained in the analysis that studied the impact of simplifying hydrogen as an ideal gas on the variables with the most significant impact on the model, it is observed that there is indeed an error in this simplification as this assumption induces an error in the computation of variables such as the internal energy and the mass flow entering into the system. However, in the verification process, we have seen how the models presented in this project and by Jemni et al. [150] have accurate results, and both models include this simplification. Therefore, it suggests that the integrated ideal gas model would give better results than the separate variables due to the cancellation of errors. This cancellation could happen because obtaining a higher mass hydrogen flow implies a higher mass of hydrogen inside the tank. Furthermore, as seen in section 5.2.2, the hydrogen temperature was underestimated under the ideal gas simplification, as the ideal gas internal energy is inferior to the real gas internal energy at the same temperature. Hence, this increase in temperature and the mass decrease would make the error in calculating the gas pressure smaller for the non-ideal gas scenario. However, we do not know only by calculating the impact of this simplification on these variables how this temperature increase would affect the hydrogen adsorption and whether this pressure error would compensate for the error induced in the gas adsorption. Therefore, a complete model is needed to know how this assumption would affect the model's behaviour. Even though the evidence suggests that the impact of this assumption is minimal, the models accurately fit the experimental data. Additionally, the modelling error in the literature is smaller than the addition of the variables error obtained in Chapter 5.

To summarize, this project demonstrated that solid hydrogen storage is a viable alternative to other storage methods, with similar working conditions and significantly lower pressures. However, more research is needed to determine the thermal properties of the adsorbents. As mentioned in section 2.1.2.1, research on these materials have focused more on variables related to their capacity and working conditions instead of their definition to integrate them into system modelling, limiting the simulation alternatives. Furthermore, the design of these tanks has shown that the available contact surface between the absorbent and hydrogen is a vital parameter for improving the system's performance. Also, combining internal and external cooling techniques has proven to significantly improve system performance, although both techniques' integration could be counterproductive for smaller tanks. Next, it was assessed that a higher AR improved the tank's performance. Lastly, the simplification of hydrogen as an ideal gas has been studied, noting that its impact is considerable in variables such as the inlet mass flow and gas internal energy in the tank. Even though the total error observed in these variables seems to be higher than the one obtained when comparing experimental data with ideal gas

models, this could be due to the errors obtained using this simplification cancelling each other out, improving the final accuracy of the model.

Chapter 7: Limitations and Outlook

This chapter covers the different limitations of this project and some research lines that could be covered in the future using this project as a reference. This project should be understood as an initial phase of the potential tangibility of the proposed storage system. Next, the limitations observed in this project are:

1. Despite having a first approximation of how the ideal gas simplification affects the model variables, it is considered that a complete non-ideal solid hydrogen model is required to research the impact of this simplification on the results, even though there is a good correlation between the literature modelling and the experimental data. Ideal gas models have an error inferior to the addition of the variable error computed in section five. Therefore, the increment in computational cost and complexity of a real gas model could be unworthy, but we do not have enough information to state this.
2. It is considered that a more detailed exergy analysis could add value to the model, as it could optimize these variables that have the most significant impact on the system's performance and efficiently increase the overall system efficiency.
3. As mentioned at the beginning of this section, this model is considered an initial modelling approximation that allows one to analyze the system's behaviour and extract useful information to compare its performance with its competitors. Moreover, tests on physical prototypes would be necessary to prove that there would not be any problem in the operation of the system.
4. Research on the required adsorbent parameters for their integration in system modelling can add value to the existing knowledge, as the literature mainly focuses on improving the adsorbent performance, and there is not enough information to model them. The properties required for their modelling are enthalpy of formation, the entropy of formation, activation energy for the adsorption and desorption, activation rate for the adsorption and desorption process, porosity, density, effective thermal conductivity and specific heat capacity.
5. After solving the layouts proposed in this project, it was observed that the memory required for the execution of these models is the main limitation found for their simulation despite having access to a supercomputer. The evidence suggested that the meshing initial properties definition was the process that saturated the hardware memory. Therefore, model meshing development would add extra value as this optimization would allow us to simulate more complex systems and research their performance.
6. This model ideally assumes that the hydrogen and refrigerant inlet conditions in the different tanks integrated into the container are equal and constant. Therefore, a more in-depth analysis is required to study the influence of the tanks on each other to simulate the performance of the tank farm more accurately as a modular storage unit.

Bibliography

[1] Intergovernmental Panel on Climate Change., "Fifth Assessment Report, Climate Change 2014," 2014. Accessed: Feb. 18, 2023. [Online]. Available: https://issuu.com/unipcc/docs/syr_ar5_final_full_wcover?utm_medium=referral&utm_source=archive.ipcc.ch

[2] UNFCCC, "The Paris Agreement," 2015. Accessed: Feb. 18, 2023. [Online]. Available: https://unfccc.int/process-and-meetings/the-paris-agreement

[3] "Mitigation of Climate Change Climate Change 2022 Working Group III contribution to the Sixth Assessment Report of the Intergovernmental Panel on Climate Change," 2022, Accessed: Feb. 18, 2023. [Online]. Available: www.ipcc.ch

[4] European Commission, "Reducing emissions from the shipping sector," 2022. https://climate.ec.europa.eu/eu-action/transport-emissions/reducing-emissions-shipping-sector_en (accessed Nov. 21, 2022).

[5] European Environment Agency, "Transport and mobility," *Topics*, May 12, 2023. https://www.eea.europa.eu/en/topics/in-depth/transport-and-mobility (accessed May 25, 2023).

[6] UNESCO World Heritage Centre, "Norwegian parliament adopts zero-emission regulations in World Heritage fjords," 2018. https://whc.unesco.org/en/news/1824 (accessed Nov. 21, 2022).

[7] M. Nilsen, "Zero emissions in the World Heritage fjords by 2026," *Norwegian Maritime Authority*, Apr. 29, 2022.

[8] Maritime and Port Authority of Singapore, "Maritime Singapore Decarbonisation Blueprint: Working Towards 2050," in *Maritime and Port Authority of Singapore*, Mar. 2022. Accessed: May 29, 2023. [Online]. Available: https://www.mpa.gov.sg/media-centre/details/cos-2022---media-factsheet---maritime-singapore-decarbonisation-blueprint-working-towards-2050

[9] International Maritime Organization, "Initial IMO GHG Strategy." https://www.imo.org/en/MediaCentre/HotTopics/Pages/Reducing-greenhouse-gas-emissions-from-ships.aspx (accessed Nov. 21, 2022).

[10] European Parliament, "FuelEU Maritime – Sustainable maritime fuels," Oct. 2022, Accessed: Nov. 27, 2022. [Online]. Available: http://www.europarl.europa.eu/thinktank

[11] O. B. Inal, B. Zincir, and C. Dere, "Hydrogen as Maritime Transportation Fuel: A Pathway for Decarbonization," *Energy, Environment, and Sustainability*, pp. 67–110, 2022, doi: 10.1007/978-981-16-8344-2_4/FIGURES/17.

[12] Scopus, "Hydrogen and maritime, analyze search results," 2023. https://www-scopus-com.tudelft.idm.oclc.org/results/results.uri?sort=plf-f&src=s&st1=maritime+hydrogen&sid=37f5b4c175aa33d1a5772e9c62d70f5c&sot=b&sdt=b&sl=32&s=TITLE-ABS-KEY%28maritime+hydrogen%29&origin=searchbasic&editSaveSearch=&yearFrom=Before+1960&yearTo=Present (accessed Mar. 27, 2023).

[13] L. van Hoecke, L. Laffineur, R. Campe, P. Perreault, S. W. Verbruggen, and S. Lenaerts, “Challenges in the use of hydrogen for maritime applications,” *Energy Environ Sci*, vol. 14, no. 2, pp. 815–843, Feb. 2021.

[14] International Energy Agency, “Energy Technology Perspectives,” 2020. [Online]. Available: www.iea.org/t&c/

[15] D. Thomas, “Amazon, Ikea and Unilever pledge zero-carbon shipping by 2040,” *BBC News*, 2022. https://www.bbc.com/news/business-58970877 (accessed Jun. 02, 2023).

[16] ABS, CE-DELFT, and ARCSILEA, “Potential of Ammonia as Fuel in Shipping,” 2022. [Online]. Available: www.emsa.europa.eu

[17] ZERO-EMISSION SHIPPING MISSION, “INDUSTRY ROADMAP FOR ZERO-EMISSION SHIPPING MISSION,” *ZERO-EMISSION SHIPPING MISSION*, vol. 1, 2022, Accessed: May 29, 2023. [Online]. Available: http://mission-innovation.net/missions/shipping/

[18] BUREAU VERITAS MARINE & OFFSHORE, “AN OVERVIEW OF AMMONIA AS FUEL FOR SHIPS,” *Marine Future Fuels*, 2023. https://marine-offshore.bureauveritas.com/shipping-decarbonization/future-fuels/ammonia (accessed May 29, 2023).

[19] Green car congress, “Amogy and Amon Maritime partner to advance ammonia power solutions for shipping,” Sep. 05, 2022. Accessed: May 29, 2023. [Online]. Available: https://www.greencarcongress.com/2022/09/20220905-amogy.html

[20] Methanex, “Methanol as a Marine Fuel,” 2022. Accessed: May 29, 2023. [Online]. Available: https://www.methanex.com/about-methanol/marine-fuel/

[21] L. Ming Main Author, L. Ming, L. Chen, and L. Siu Lee Jasmine Sze Jia Yin Koh Eng Kiong Yang Mengyao Gou Xueni, “Methanol as a Marine Fuel-Availability and Sea Trial Considerations Alternative Fuels for International Shipping A Study on the Future Energy Options of Singapore Harbour Craft Electrification of Singapore Harbour Craft-Shore and Vessel Power System Considerations Executive Summary,” 2020.

[22] UECC, “World’s first dual-fuel LNG battery hybrid PCTC to start trading,” Nov. 29, 2021. https://www.uecc.com/news/2021/november/debut-delivery-world-s-first-dual-fuel-lng-battery-hybrid-pctc-to-start-trading/ (accessed Nov. 27, 2022).

[23] C. Fagergren and P. Tunell, “Multi-fuel: a step towards sustainable shipping.” https://www.soyagroup.com/en/shipping/multi-fuel-a-step-towards-sustainable-shipping/ (accessed Nov. 27, 2022).

[24] Lloyd’s Register, “Zero-Emission Vessels 2030. How do we get there?,” 2018.

[25] J. Hunter, “MF HYDRA CAR FERRY NORWAY LIQUEFIED LIQUIDE HYDROGEN,” Aug. 2021. http://elizabethqueenseaswann.com/HISTORY/LH2_Ships_Ferries_Yachts_Hydrogen_Projects/MF_Hydra_Norled_Car_Ferry_Norway_Liquefied_Hydrogen_Liquide.html (accessed May 29, 2023).

[26] M. Steen, H. Bach, Ø. Bjørgum, T. Hansen, and A. Kenzhegaliyeva, “A technological innovation system (TIS) analysis of hydrogen, battery electric, liquefied biogas, and biodiesel in the maritime sector,” *SINTEF Digital Innovation and Leadership Greening the fleet*, 2019.

[27] Yara International, “Yara Birkeland,” *News and media*, 2021. https://www.yara.com/news-and-media/media-library/press-kits/yara-birkeland-press-kit/ (accessed May 29, 2023).

[28] Fleetzero, “Shipping electrified,” 2023. https://www.fleetzero.com/ (accessed May 29, 2023).

[29] Holland Shipyards Group, “DELIVERY OF THE FIRST HYDROGEN DRIVEN INLAND VESSEL,” May 25, 2023. https://www.hollandshipyardsgroup.com/news/delivery-of-the-first-hydrogen-driven-inland-vessel (accessed May 29, 2023).

[30] Energy Observer, “Energy Observer 2, a demonstrator vessel that runs on liquid H2.” https://www.energy-observer.org/resources/energy-observer-2-liquid-hydrogen (accessed May 29, 2023).

[31] HyShip, “About HyShip,” *About*, 2021. https://hyship.eu/about/ (accessed May 29, 2023).

[32] A. Nemmour, A. Inayat, I. Janajreh, and C. Ghenai, “Green hydrogen-based E-fuels (E-methane, E-methanol, E-ammonia) to support clean energy transition: A literature review,” *Int J Hydrogen Energy*, Apr. 2023.

[33] A. Demirbas, A. Bafail, W. Ahmad, and M. Sheikh, “Biodiesel production from non-edible plant oils,” *Energy Exploration & Exploitation*, 20116.

[34] N. York, “United Nations Conference on Trade and Development Biofuel production technologies: status, prospects and implications for trade and development,” 2008.

[35] K. Dawe, R. Krantz, L. Mouftier, and E. Skov Christiansen, “Future biofuels for shipping,” Aug. 2021. Accessed: May 30, 2023. [Online]. Available: https://www.globalmaritimeforum.org/news/future-biofuels-for-shipping

[36] R. ; Laursen and D. ; Barcarolo, “Update on Potential of Biofuels for Shipping Authors: Legal notice: Copyright notice,” 2022. [Online]. Available: www.emsa.europa.eu

[37] A. Schikker, “World first for Boskalis by operating a dredging vessel on 100% bio-fuel oil,” Papendrecht, Oct. 17, 2019. [Online]. Available: www.boskalis.com.

[38] M. Carmo and D. Stolten, “Energy Storage Using Hydrogen Produced From Excess Renewable Electricity: Power to Hydrogen,” *Science and Engineering of Hydrogen-Based Energy Technologies: Hydrogen Production and Practical Applications in Energy Generation*, pp. 165–199, Jan. 2019.

[39] D. L. Heiserman, *Exploring chemical elements and their compounds*, 1st ed. c1992, 1992. Accessed: May 31, 2023. [Online]. Available: https://www.worldcat.org/title/1034660716

[40] M.-R. de Valladares, “GLOBAL TRENDS AND OUTLOOK FOR HYDROGEN,” 2017.

[41] Z. Abdin, A. Zafaranloo, A. Rafiee, W. M Erida B, W. Lipi Nski C, and K. R. Khalilpour, “Hydrogen as an energy vector,” *Renewable and Sustainable Energy Reviews*, vol. 120, p. 109620, 2020.

[42] F. Zhang, P. Zhao, M. Niu, and J. Maddy, “The survey of key technologies in hydrogen energy storage,” *International Journal of Hydrogen Energy*, vol. 41, no. 33. Elsevier Ltd, pp. 14535–14552, Sep. 07, 2016.

[43] H. Nami, O. B. Rizvandi, C. Chatzichristodoulou, P. V. Hendriksen, and H. L. Frandsen, “Techno-economic analysis of current and emerging electrolysis technologies for green hydrogen production,” *Energy Convers Manag*, vol. 269, p. 116162, Oct. 2022, doi: 10.1016/J.ENCONMAN.2022.116162.

[44] E. Rivard, M. Trudeau, and K. Zaghib, “Hydrogen storage for mobility: A review,” *Materials*, vol. 12, no. 12. MDPI AG, Jun. 01, 2019.

[45] I. A. Hassan, H. S. Ramadan, M. A. Saleh, and D. Hissel, “Hydrogen storage technologies for stationary and mobile applications: Review, analysis and perspectives,” *Renewable and Sustainable Energy Reviews*, vol. 149, p. 111311, Oct. 2021.

[46] G. Parks, R. Boyd, J. Cornish, R. Remick, and I. Review Panel, “Hydrogen Station Compression, Storage, and Dispensing Technical Status and Costs: Systems Integration,” 2020, Accessed: Jun. 08, 2023. [Online]. Available: http://www.osti.gov/bridge

[47] G. Valenti, “Hydrogen liquefaction and liquid hydrogen storage,” in *Compendium of Hydrogen Energy*, Elsevier, 2016, pp. 27–51.

[48] G. Valenti and E. Macchi, “Proposal of an innovative, high-efficiency, large-scale hydrogen liquefier,” 2008.

[49] B. Ghorbani, M. Mehrpooya, M. Aasadnia, and M. S. Niasar, “Hydrogen liquefaction process using solar energy and organic Rankine cycle power system,” *J Clean Prod*, vol. 235, pp. 1465–1482, Oct. 2019.

[50] J. Andersson and S. Grönkvist, “Large-scale storage of hydrogen,” *Int J Hydrogen Energy*, vol. 44, no. 23, pp. 11901–11919, May 2019, doi: 10.1016/J.IJHYDENE.2019.03.063.

[51] Department of Energy, “Hydrogen Storage.” https://www.energy.gov/eere/fuelcells/hydrogen-storage (accessed Jun. 08, 2023).

[52] K. Ohira, “Slush hydrogen production, storage, and transportation,” in *Compendium of Hydrogen Energy*, Elsevier, 2016, pp. 53–90.

[53] C. M. Araujo *et al.*, “Fuel selection for a regenerative organic fuel cell/flow battery: thermodynamic considerations,” *Energy Environ Sci*, vol. 5, no. 11, pp. 9534–9542, Oct. 2012.

[54] K. Müller, J. Völkl, and W. Arlt, “Thermodynamic Evaluation of Potential Organic Hydrogen Carriers,” *Energy Technology*, vol. 1, no. 1, pp. 20–24, Jan. 2013.

[55] F. Sotoodeh, B. J. M. Huber, and K. J. Smith, “The effect of the N atom on the dehydrogenation of heterocycles used for hydrogen storage,” *Appl Catal A Gen*, vol. 419–420, pp. 67–72, Mar. 2012.

[56] F. Sotoodeh and K. J. Smith, “An overview of the kinetics and catalysis of hydrogen storage on organic liquids,” *Can J Chem Eng*, vol. 91, no. 9, pp. 1477–1490, Sep. 2013.

[57] C. G. Ramos, S. A. Sousa, A. M. Grilo, J. R. Feliciano, and J. H. Leitão, “Retraction for Ramos et al., The second RNA chaperone, Hfq2, is also required for survival under stress and full

virulence of Burkholderia cenocepacia J2315," *J Bacteriol*, vol. 196, no. 22, pp. 3980–3980, 2014.

[58] M. Amende *et al.*, "Size and structure effects controlling the stability of the liquid organic hydrogen carrier dodecahydro- N -ethylcarbazole during dehydrogenation over pt model catalysts," *Journal of Physical Chemistry Letters*, vol. 5, no. 8, pp. 1498–1504, Apr. 2014.

[59] M. Amende *et al.*, "Model Catalytic Studies of Liquid Organic Hydrogen Carriers: Dehydrogenation and Decomposition Mechanisms of Dodecahydro- N-ethylcarbazole on Pt(111)," *ACS Catal*, vol. 4, no. 2, pp. 657–665, Feb. 2014.

[60] D. D. Papadias, J. K. Peng, and R. K. Ahluwalia, "Hydrogen carriers: Production, transmission, decomposition, and storage," *Int J Hydrogen Energy*, vol. 46, no. 47, pp. 24169–24189, Jul. 2021.

[61] A. Klerke, C. H. Christensen, J. K. Nørskov, and T. Vegge, "Ammonia for hydrogen storage: challenges and opportunities," *J Mater Chem*, vol. 18, no. 20, pp. 2304–2310, May 2008.

[62] G. Meng, C. Jiang, J. Ma, Q. Ma, and X. Liu, "Comparative study on the performance of a SDC-based SOFC fueled by ammonia and hydrogen," *J Power Sources*, vol. 173, no. 1, pp. 189–193, Nov. 2007

[63] G. G. M. Fournier, I. W. Cumming, and K. Hellgardt, "High performance direct ammonia solid oxide fuel cell," *J Power Sources*, vol. 162, no. 1, pp. 198–206, Nov. 2006.

[64] T. B. H. Nguyen and E. Zondervan, "Methanol production from captured CO 2 using hydrogenation and reforming technologies_ environmental and economic evaluation," 2019.

[65] É. Simões Van-Dal and C. Bouallou, "Design and simulation of a methanol production plant from CO 2 hydrogenation," 2013.

[66] C. N. Hamelinck and A. P. C. Faaij, "Future prospects for production of methanol and hydrogen from biomass".

[67] A. H. Zahid, N. Amin, F. Nisar, and S. Saghir, "Analysis of MTH-System (Methylcyclohexane-Toluene-Hydrogen-System) for hydrogen production as fuel for power plants," *Int J Hydrogen Energy*, vol. 45, no. 56, pp. 32234–32242, Nov. 2020.

[68] P. Bénard and R. Chahine, "Storage of hydrogen by physisorption on carbon and nanostructured materials," *Scr Mater*, vol. 56, no. 10, pp. 803–808, May 2007

[69] L.-J. Ma, T. Han, J. Jia, and H.-S. Wu, "Cooperative physisorption and chemisorption of hydrogen on vanadium-decorated benzene †," 2020.

[70] A. Züttel, "Materials for hydrogen storage," 2003.

[71] E. Rozzi, F. D. Minuto, and A. Lanzini, "Dynamic modeling and thermal management of a Power-to-Power system with hydrogen storage in microporous adsorbent materials," *J Energy Storage*, vol. 41, p. 102953, Sep. 2021.

[72] P. Prachi R., W. Mahesh M., and G. Aneesh C., "A Review on Solid State Hydrogen Storage Material," *Advances in Energy and Power*, vol. 4, no. 2, pp. 11–22, Jun. 2016.

[73] A. Yadav, A. Dashora, N. Patel, A. Miotello, M. Press, and D. C. Kothari, “Study of 2D MXene Cr2C material for hydrogen storage using density functional theory,” *Appl Surf Sci*, vol. 389, pp. 88–95, 2016, Accessed: Jun. 08, 2023. [Online].

[74] G. K. Sunnardianto, G. Bokas, A. Hussein, Walters Carey, O. A. Moultos, and P. Dey, “Efficient hydrogen storage in defective graphene and its mechanical stability: A combined density functional theory and molecular dynamics simulation study,” *International Journal of Hydrogen*, 2021.

[75] J. Ren, N. M. Musyoka, H. W. Langmi, M. Mathe, and S. Liao, “Current research trends and perspectives on materials-based hydrogen storage solutions: A critical review,” *International Journal of Hydrogen*, vol. 42, pp. 289–311, 2017, Accessed: Jun. 08, 2023. [Online].

[76] P. Prachi R., W. Mahesh M., and G. Aneesh C., “A Review on Solid State Hydrogen Storage Material,” *Advances in Energy and Power*, vol. 4, no. 2, pp. 11–22, Jun. 2016.

[77] X. Lin *et al.*, “High H2 adsorption by coordination-framework materials,” *Angew Chem Int Ed Engl*, vol. 45, no. 44, pp. 7358–7364, Nov. 2006.

[78] H. Furukawa, M. A. Miller, and O. M. Yaghi, “Independent verification of the saturation hydrogen uptake in MOF-177 and establishment of a benchmark for hydrogen adsorption in metal–organic frameworks,” *J Mater Chem*, vol. 17, no. 30, pp. 3197–3204, Aug. 2007.

[79] L. Zhou, Y. Zhou, and Y. Sun, “Enhanced storage of hydrogen at the temperature of liquid nitrogen,” *Int J Hydrogen Energy*, vol. 29, no. 3, pp. 319–322, Mar. 2004.

[80] S. H. Ye *et al.*, “Characteristics of mixed hydrogen storage electrode,” *J Alloys Compd*, vol. 292, no. 1–2, pp. 191–193, Nov. 1999.

[81] H. W. Langmi *et al.*, “Hydrogen storage in ion-exchanged zeolites,” *J Alloys Compd*, vol. 404–406, no. SPEC. ISS., pp. 637–642, Dec. 2005.

[82] J. Jepsen *et al.*, “Fundamental Material Properties of the 2LiBH4-MgH2 Reactive Hydride Composite for Hydrogen Storage: (II) Kinetic Properties,” *Energies 2018, Vol. 11, Page 1170*, vol. 11, no. 5, p. 1170, May 2018.

[83] A. I. Bevan, A. Züttel, D. Book, and I. R. Harris, “Performance of a metal hydride store on the ‘Ross Barlow’ hydrogen powered canal boat,” *Faraday Discuss*, vol. 151, no. 0, pp. 353–367, Aug. 2011.

[84] C. Fiori, A. Dell’Era, F. Zuccari, A. Santiangeli, A. D’Orazio, and F. Orecchini, “Hydrides for submarine applications: Overview and identification of optimal alloys for air independent propulsion maximization,” *Int J Hydrogen Energy*, vol. 40, no. 35, pp. 11879–11889, Sep. 2015.

[85] A. A. Rabienataj Darzi, H. Hassanzadeh Afrouzi, A. Moshfegh, and M. Farhadi, “Absorption and desorption of hydrogen in long metal hydride tank equipped with phase change material jacket,” *Int J Hydrogen Energy*, vol. 41, no. 22, pp. 9595–9610, Jun. 2016.

[86] Z. Bao, F. Yang, Z. Wu, X. Cao, and Z. Zhang, “Simulation studies on heat and mass transfer in high-temperature magnesium hydride reactors,” *Appl Energy*, vol. 112, pp. 1181–1189, 2013.

[87] C.-S. Wang and J. Brinkerhoff, “Low-cost lumped parameter modelling of hydrogen storage in solid-state materials.,” *Energy Convers Manag*, 2022.

[88] Y. Wang, X. C. Adroher, J. Chen, X. G. Yang, and T. Miller, “Three-dimensional modeling of hydrogen sorption in metal hydride hydrogen storage beds,” *J Power Sources*, vol. 194, no. 2, pp. 997–1006, Dec. 2009.

[89] M. Bhouri, J. Goyette, B. J. Hardy, and D. L. Anton, “Numerical modeling and performance evaluation of multi-tubular sodium alanate hydride finned reactor,” *Int J Hydrogen Energy*, vol. 37, no. 2, pp. 1551–1567, 2012.

[90] Z. Wu, F. Yang, Z. Zhang, and Z. Bao, “Magnesium based metal hydride reactor incorporating helical coil heat exchanger: Simulation study and optimal design,” *Appl Energy*, vol. 130, pp. 712–722, Oct. 2014.

[91] A. Chaise, P. Marty, P. de Rango, and D. Fruchart, “A simple criterion for estimating the effect of pressure gradients during hydrogen absorption in a hydride reactor,” *Int J Heat Mass Transf*, vol. 52, no. 19–20, pp. 4564–4572, Sep. 2009.

[92] C. A. Chung and C.-J. Ho, “Thermal-fluid behavior of the hydriding and dehydriding processes in a metal hydride hydrogen storage canister,” *Int J Hydrogen Energy*, vol. 34, pp. 4351–4364, 2009.

[93] H. Choi and A. F. Mills, “Heat and mass transfer in metal hydride beds for heat pump applications,” *Int J Heat Mass Transf*, vol. 33, no. 6, pp. 1281–1288, Jun. 1990.

[94] A. K. Rao, “Stress Concentrations and Singularities at Interface Corners,” *ZAMM - Journal of Applied Mathematics and Mechanics / Zeitschrift für Angewandte Mathematik und Mechanik*, vol. 51, no. 5, pp. 395–406, 1971.

[95] M. Negahban, “Beams with axial loads,” *University of Nebraska*. 2000. Accessed: Feb. 10, 2023. [Online]. Available: http://emweb.unl.edu/negahban/em325/18-pressure-vessels/pressure%20vessels.htm

[96] D. Mori and K. Hirose, “Recent challenges of hydrogen storage technologies for fuel cell vehicles,” *Int J Hydrogen Energy*, vol. 34, no. 10, pp. 4569–4574, May 2009.

[97] S. Mellouli, N. ben Khedher, F. Askri, A. Jemni, and S. ben Nasrallah, “Numerical analysis of metal hydride tank with phase change material,” 2015.

[98] J. G. Vitillo, G. Ricchiardi, G. Spoto, and A. Zecchina, “Theoretical maximal storage of hydrogen in zeolitic frameworks,” *Physical Chemistry Chemical Physics*, vol. 7, no. 23, pp. 3948–3954, Nov. 2005.

[99] H. W. Langmi *et al.*, “Hydrogen adsorption in zeolites A, X, Y and RHO,” *J Alloys Compd*, vol. 356–357, pp. 710–715, Aug. 2003.

[100] P. M. Budd *et al.*, “The potential of organic polymer-based hydrogen storage materials,” *Physical Chemistry Chemical Physics*, vol. 9, no. 15, pp. 1802–1808, Apr. 2007.

[101] B. S. Ghanem *et al.*, “A triptycene-based polymer of intrinsic microposity that displays enhanced surface area and hydrogen adsorption,” *Chemical Communications*, no. 1, pp. 67–69, Dec. 2006.

[102] M. Sturini *et al.*, "Combined Layer-by-Layer/Hydrothermal Synthesis of Fe3O4@MIL-100(Fe) for Ofloxacin Adsorption from Environmental Waters," *Nanomaterials (Basel)*, vol. 11, no. 12, Dec. 2021.

[103] A. Chibani, C. Bougriou, and S. Merouani, "Simulation of hydrogen absorption/desorption on metal hydride LaNi5-H2: Mass and heat transfer," *Appl Therm Eng*, vol. 142, pp. 110–117, Sep. 2018.

[104] A. Züttel, P. Wenger, S. Rentsch, P. Sudan, P. Mauron, and C. Emmenegger, "LiBH4 a new hydrogen storage material," *J Power Sources*, vol. 118, no. 1–2, pp. 1–7, May 2003.

[105] B. Bogdanovic and M. Schwickardi, "Ti-doped alkali metal aluminium hydrides as potential novel reversible hydrogen storage materials".

[106] L. Morris *et al.*, "A manganese hydride molecular sieve for practical hydrogen storage under ambient conditions," *Energy Environ Sci*, vol. 12, no. 5, pp. 1580–1591, May 2019,.

[107] S. Zhao, L. Liang, B. Liu, L. Wang, and F. Liang, "Superior Dehydrogenation Performance of α-AlH3 Catalyzed by Li3N: Realizing 8.0 wt.% Capacity at 100 °C," *Small*, vol. 18, no. 17, Apr. 2022.

[108] L. Liang, Q. Yang, S. Zhao, L. Wang, and F. Liang, "Excellent catalytic effect of LaNi5 on hydrogen storage properties for aluminium hydride at mild temperature," *Int J Hydrogen Energy*, vol. 46, no. 78, pp. 38733–38740, Nov. 2021.

[109] M. Ismail, Y. Zhao, X. B. Yu, and S. X. Dou, "Effect of different additives on the hydrogen storage properties of the MgH 2 -LiAlH 4 destabilized system," *RSC Adv*, vol. 1, no. 3, pp. 408–414, Sep. 2011.

[110] C. Pratthana and K. F. Aguey-Zinsou, "LiAlH4Nanoparticles Encapsulated within Metallic Titanium Shells for Enhanced Hydrogen Storage," *ACS Appl Nano Mater*, vol. 5, no. 11, pp. 16413–16422, Nov. 2022

[111] M. Ismail, N. Juahir, and N. S. Mustafa, "Improved hydrogen storage properties of MgH2 Co-doped with FeCl3 and carbon nanotubes," *Journal of Physical Chemistry C*, vol. 118, no. 33, pp. 18878–18883, Aug. 2014.

[112] S. N. Nyamsi, F. Yang, and Z. Zhang, "An optimization study on the finned tube heat exchanger used in hydride hydrogen storage system e analytical method and numerical simulation," 2012.

[113] A. Chaise, P. De Rango, P. Marty, and D. Fruchart, "Experimental and numerical study of a magnesium hydride tank," *Int J Hydrogen Energy*, vol. 35, no. 12, pp. 6311–6322, Jun. 2010.

[114] R. Sreeraj, A. K. Aadhithiyan, and S. Anbarasu, "Integration of thermal augmentation methods in hydride beds for metal hydride based hydrogen storage systems: Review and recommendation," *J Energy Storage*, vol. 52, p. 105039, Aug. 2022.

[115] M. Raju and S. Kumar, "Optimization of heat exchanger designs in metal hydride based hydrogen storage systems," 2011.

[116] P. D. Goodell, “Thermal conductivity of hydriding alloy powders and comparisons of reactor systems,” *Journal of the Less Common Metals*, vol. 74, no. 1, pp. 175–184, Oct. 1980.

[117] B. Delhomme *et al.*, “Large scale magnesium hydride tank coupled with an external heat source,” 2012.

[118] J.-G. Park, S.-C. Han, H.-Y. Jang, S.-M. Lee, P. S. Lee, and J.-Y. Lee, “The development of compressor-driven metal hydride heat pump (CDMHHP) system as an air conditioner,” *Int J Hydrogen Energy*, vol. 27, pp. 941–944, 2002, Accessed: Feb. 13, 2023. [Online]. Available: www.elsevier.com/locate/ijhydene

[119] S.-G. Lee, H.-H. Lee, K.-Y. Lee, and J.-Y. Lee, “A~OY~ AND CO~POUND5 Dynamic reaction characteristics of the tubular hydride bed with large mass,” *J Alloys Compd*, vol. 235, pp. 84–92, 1996.

[120] G. Wu, J. Zhang, Q. Li, and K. Chou, “A new model to describe absorption kinetics of Mg-based hydrogen storage alloys,” *Int J Hydrogen Energy*, vol. 36, no. 20, pp. 12923–12931, Oct. 2011.

[121] I. Tolj *et al.*, “Hydride4Mobility, European Commission, Prototype of advanced MH container for on-board hydrogen storage (hardware & documentation),” 2019.

[122] J. Nam, J. Ko, and H. Ju, “Three-dimensional modeling and simulation of hydrogen absorption in metal hydride hydrogen storage vessels,” 2011.

[123] B. Delhomme *et al.*, “Large scale magnesium hydride tank coupled with an external heat source,” *Int J Hydrogen Energy*, vol. 37, no. 11, pp. 9103–9111, Jun. 2012.

[124] J. Zhang, T. S. Fisher, P. V. Ramachandran, J. P. Gore, and I. Mudawar, “A Review of Heat Transfer Issues in Hydrogen Storage Technologies,” *J Heat Transfer*, vol. 127, no. 12, pp. 1391–1399, Dec. 2005.

[125] M. Afzal, R. Mane, and P. Sharma, “Heat transfer techniques in metal hydride hydrogen storage: A review,” *Int J Hydrogen Energy*, vol. 42, no. 52, pp. 30661–30682, Dec. 2017.

[126] D. W. Sun and S. J. Deng, “A theoretical model predicting the effective thermal conductivity in powdered metal hydride beds,” *Int J Hydrogen Energy*, vol. 15, no. 5, pp. 331–336, Jan. 1990.

[127] D. W. Sun and S. J. Deng, “A theoretical model predicting the effective thermal conductivity in powdered metal hydride beds,” *Int J Hydrogen Energy*, vol. 15, no. 5, pp. 331–336, 1990.

[128] T. Oi, K. Maki, and Y. Sakaki, “Heat transfer characteristics of the metal hydride vessel based on the plate-fin type heat exchanger,” *J Power Sources*, vol. 125, no. 1, pp. 52–61, Jan. 2004.

[129] M. Botzung *et al.*, “Simulation and experimental validation of a hydrogen storage tank with metal hydrides,” *Int J Hydrogen Energy*, vol. 33, no. 1, pp. 98–104, Jan. 2008.

[130] Z. Guo, “Enhancement of heat and mass transfer in metal hydride beds with the addition of Al plates,” *Warme- und Stoffubertragung Zeitschrift*, vol. 34, no. 6, pp. 517–523, 1999.

[131] S. Garrier *et al.*, “MgH2 intermediate scale tank tests under various experimental conditions,” *Int J Hydrogen Energy*, vol. 36, no. 16, pp. 9719–9726, Aug. 2011.

[132] B. D. MacDonald and A. M. Rowe, “Impacts of external heat transfer enhancements on metal hydride storage tanks,” *Int J Hydrogen Energy*, vol. 31, no. 12, pp. 1721–1731, Sep. 2006.

[133] G. Andreasen *et al.*, “Hydrogen desorption from a hydride container under different heat exchange conditions,” *Int J Hydrogen Energy*, vol. 38, no. 30, pp. 13352–13359, Oct. 2013.

[134] S. N. Nyamsi, F. Yang, and Z. Zhang, “An optimization study on the finned tube heat exchanger used in hydride hydrogen storage system – analytical method and numerical simulation,” *Int J Hydrogen Energy*, vol. 37, no. 21, pp. 16078–16092, Nov. 2012

[135] Y. Kaplan, “Effect of design parameters on enhancement of hydrogen charging in metal hydride reactors,” *Int J Hydrogen Energy*, vol. 34, no. 5, pp. 2288–2294, Mar. 2009.

[136] A. Freni, F. Cipitì, and G. Cacciola, “Finite element-based simulation of a metal hydride-based hydrogen storage tank,” *Int J Hydrogen Energy*, vol. 34, no. 20, pp. 8574–8582, Oct. 2009.

[137] F. Askri, M. ben Salah, A. Jemni, and S. ben Nasrallah, “Optimization of hydrogen storage in metal-hydride tanks,” *Int J Hydrogen Energy*, vol. 34, no. 2, pp. 897–905, Jan. 2009.

[138] C. Na Ranong *et al.*, “Concept, Design and Manufacture of a Prototype Hydrogen Storage Tank Based on Sodium Alanate,” *Chem Eng Technol*, vol. 32, no. 8, pp. 1154–1163, Aug. 2009.

[139] G. A. Lozano *et al.*, “Optimization of hydrogen storage tubular tanks based on light weight hydrides,” 2011.

[140] M. Lototskyy, J. M. Sibanyoni, R. v. Denys, M. Williams, B. G. Pollet, and V. A. Yartys, “Magnesium–carbon hydrogen storage hybrid materials produced by reactive ball milling in hydrogen,” *Carbon N Y*, vol. 57, pp. 146–160, Jun. 2013.

[141] A. Nakano, T. Maeda, H. Ito, T. Motyka, J. M. Perez-Berrios, and S. Greenway, “Experimental Study on a Metal Hydride Tank for the Totalized Hydrogen Energy Utilization System,” *Energy Procedia*, vol. 29, pp. 463–468, Jan. 2012.

[142] A. Nakano *et al.*, “Study on a metal hydride tank to support energy storage for renewable energy,” *J Alloys Compd*, vol. 580, no. SUPPL1, pp. S418–S422, Dec. 2013.

[143] S. Garrier, B. Delhomme, P. de Rango, P. Marty, D. Fruchart, and S. Miraglia, “A new MgH 2 tank concept using a phase-change material to store the heat of reaction,” 2013.

[144] H. Ben Mâad, F. Askri, and S. Ben Nasrallah, “Heat and mass transfer in a metal hydrogen reactor equipped with a phase-change heat-exchanger,” *International Journal of Thermal Sciences*, vol. 99, pp. 271–278, Jan. 2016.

[145] S. Mellouli, F. Askri, E. Abhilash, and S. ben Nasrallah, “Impact of using a heat transfer fluid pipe in a metal hydride-phase change material tank,” 2016.

[146] S. S. Mohammadshahi, E. M. A. Gray, and C. J. Webb, “A review of mathematical modelling of metal-hydride systems for hydrogen storage applications,” *Int J Hydrogen Energy*, vol. 41, no. 5, pp. 3470–3484, Feb. 2016.

[147] COMSOL AB, “COMSOL Multiphysics® v. 6.1. .” Stockholm, Sweden, 2022.

[148] Inc. ANSYS, “ Ansys® Academic Research Mechanical.” 2022.

[149] I. International Organization for Standardization, “ISO 668:2020,” 2020.

[150] A. Jemni, S. Ben Nasrallah, and J. Lamloumi, “Experimental and theoretical study of ametal–hydrogen reactor,” *Int J Hydrogen Energy*, vol. 24, no. 7, pp. 631–644, Jul. 1999.

[151] P. H. Oosthuizen and W. E. Carscallen, “Compressible fluid flow,” p. 548, 1997, Accessed: Feb. 07, 2023. [Online].

[152] M. Deymi-Dashtebayaz, M. Farzaneh-Gord, N. Nooralipoor, and H. Niazmand, “The complete modelling of the filling process of hydrogen onboard vehicle cylinders,” *Brazilian Journal of Chemical Engineering*, vol. 33, no. 2, pp. 391–399, Apr. 2016.

[153] M. Ram Gopal and S. Srinivasa Murthy, “Parametric studies on heat and mass transfer in metal hydride beds,” *Chemical Engineering and Processing: Process Intensification*, vol. 32, no. 4, pp. 217–223, Aug. 1993.

[154] A. F. Mills and C. F. M. Coimbra, *Basic heat and mass transfer*, Third. 2015.

[155] T. B. Belytschko and J. M. Kennedy, “Computer models for subassembly simulation,” *Nuclear Engineering and Design*, vol. 49, no. 1–2, pp. 17–38, Jul. 1978.

[156] C. Wollbland, “Your Guide to Meshing Techniques for Efficient CFD Modeling,” 2018. https://www.comsol.com/blogs/your-guide-to-meshing-techniques-for-efficient-cfd-modeling/ (accessed Jul. 11, 2023).

[157] E. W. Lemmon, H. Bell, M. L. Huber, and M. O. McLinden, “NIST Standard Reference Database 23: Reference Fluid Thermodynamic and Transport Properties-REFPROP, Version 10.0, National Institute of Standards and Technology,” 2018.

[158] M. Steilen and L. Jörissen, “Hydrogen Conversion into Electricity and Thermal Energy by Fuel Cells: Use of H2-Systems and Batteries,” *Electrochemical Energy Storage for Renewable Sources and Grid Balancing*, pp. 143–158, Jan. 2015.

[159] Inc. The MathWorks, “MATLAB version: 9.13.0 (R2022b).” 2022.

[160] I. H. Bell, J. Wronski, S. Quoilin, and V. Lemort, “Pure and Pseudo-pure Fluid Thermophysical Property Evaluation and the Open-Source Thermophysical Property Library CoolProp,” *Ind Eng Chem Res*, vol. 53, pp. 2498–2508, 2014.

[161] P. Nederstigt, “Real Gas Thermodynamics and the isentropic behavior of substances,” 2017.

Annex A

This annexe details each geometry studied in this project, specifying the value of the parameterised variables mentioned in subsection 3.4. Proposed designs definition, in each of the configurations. As explained in this segment, the alternative designs were evaluated implementing magnesium hydride and lanthanum nickel as adsorbents. The enumeration followed in this Annex corresponds to the name given to the attached models.

Geometry 1

This layout was designed to be installed vertically in the container, and considering the interior volume, 12 tanks could be installed. This geometry has a tank longitude of 1.89m, an external radius of 0.47 m, an adsorbent radius of 0.4m, and 9 torus adsorbent.

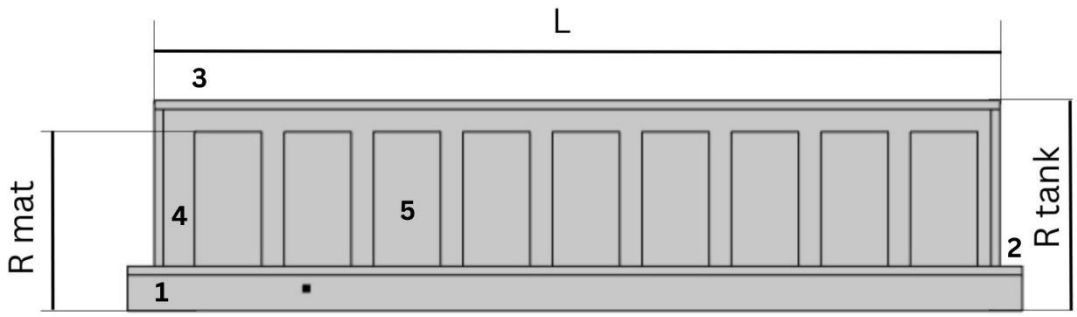

Figure 26: Geometry 1 section layout.

Geometry 2

This tank was created for vertical installation within the container. It is possible to install 12 tanks according to the container's interior volume. The tanks in this design have a length of 1.89 meters, an outer radius of 0.37 meters, an adsorbent radius of 0.3 meters, and 9 torus material pieces.

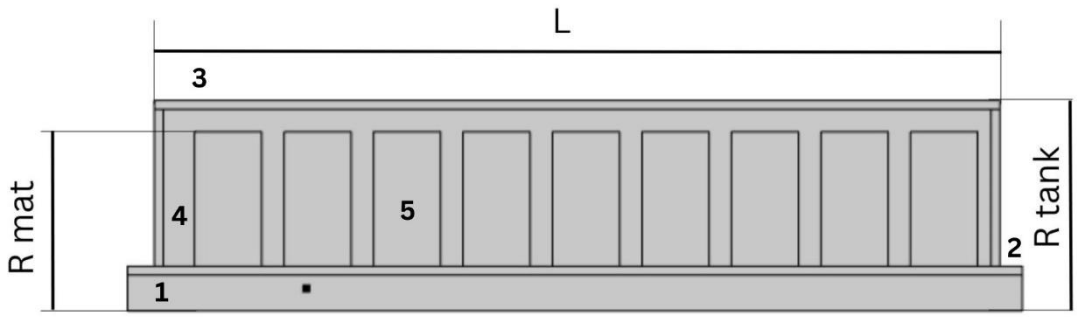

Figure 27: Geometry 2 section configuration.

Geometry 3

This design was conceptualized to be installed horizontally in the container, and considering the interior volume restrictions, 4 tanks could be employed. This geometry has a tank longitude of 10.89m, an external radius of 0.47 m, an adsorbent radius of 0.4m, and 54 torus adsorbent.

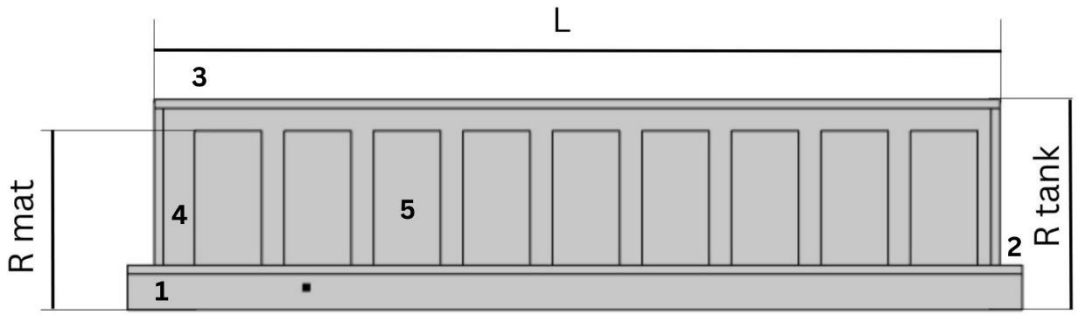

Figure 28: Geometry 3 design concept.

Geometry 4

This configuration was designed for a horizontal implementation in the container, and considering the container interior volume restrictions, 4 tanks could be employed. This geometry has a tank longitude of 10.89m, an external radius of 0.37 m, an adsorbent radius of 0.3m, and 54 torus material pieces.

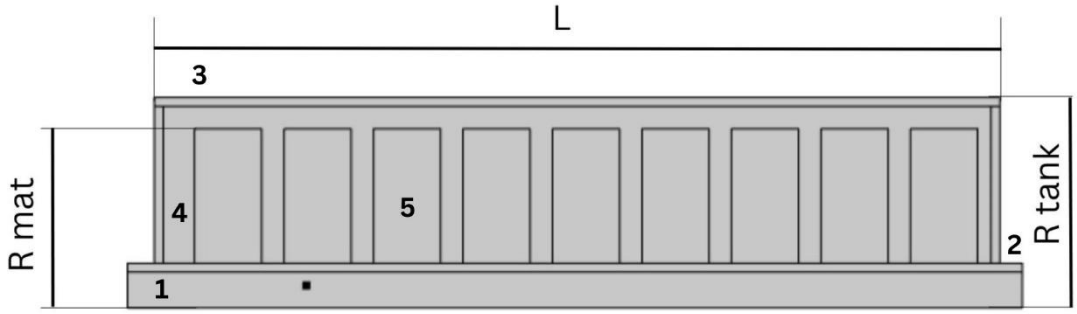

Figure 29: Geometry 4 section layout.

Geometry 5

This layout was designed to be installed vertically in the container, and considering the interior volume, 12 tanks could be installed. This geometry has a tank longitude of 1.89m, an external radius of 0.47 m, an adsorbent radius of 0.4m, and a longitude of the hydrogen host of 1.8 m.

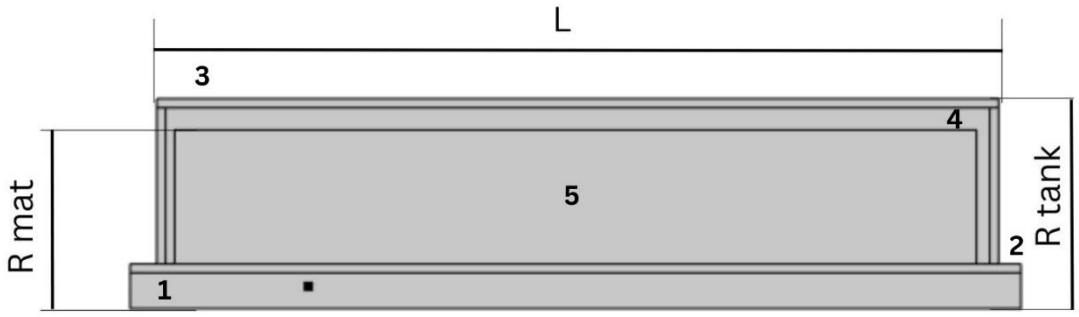

Figure 30: Geometry 5 definition

Geometry 6

This tank was created for vertical installation within the container. It is possible to install 12 tanks according to the container's interior volume. The tanks in this design have a length of 1.89

meters, an outer radius of 0.37 meters, an adsorbent longitude of 1.8 meters, and a host radius of 0.3m.

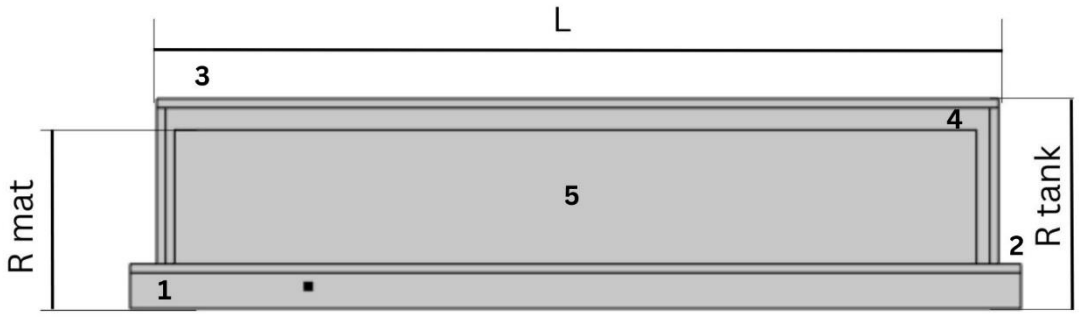

Figure 31: Geometry 6 layout.

Geometry 7

This design was conceptualized to be installed horizontally in the container, and considering the interior volume restrictions, 4 tanks could be employed. This geometry has a tank longitude of 10.89m, an external radius of 0.47 m, an adsorbent radius of 0.4m, and an adsorbent length of 10.8m.

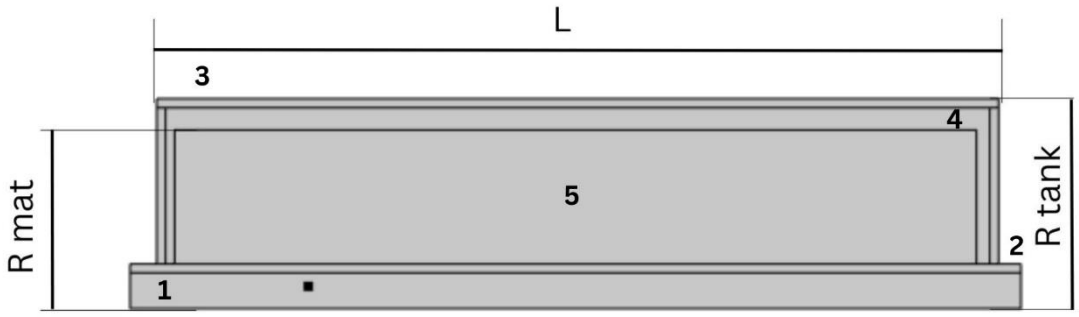

Figure 32: Geometry 7 section design.

Geometry 8

This configuration was designed for a horizontal implementation in the container, and considering the container interior volume restrictions, 4 tanks could be employed. This geometry has a tank longitude of 10.89m, an external radius of 0.37 m, an adsorbent radius of 0.3m, and material longitude of 10.8m.

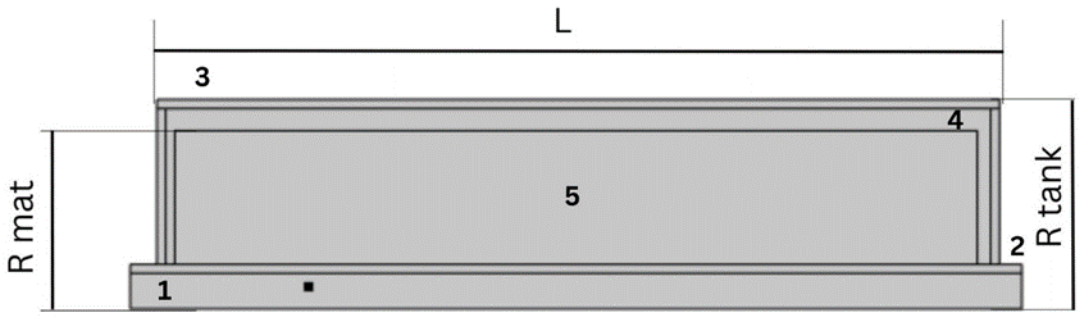

Figure 33: Geometry 8 configuration.

Geometry 9

This layout was designed to be installed vertically in the container, and considering the interior volume, 6 tanks could be installed. This geometry has a tank longitude of 1.89m, an external radius of 0.57 m, an adsorbent radius of 0.4m, and 9 torus adsorbent.

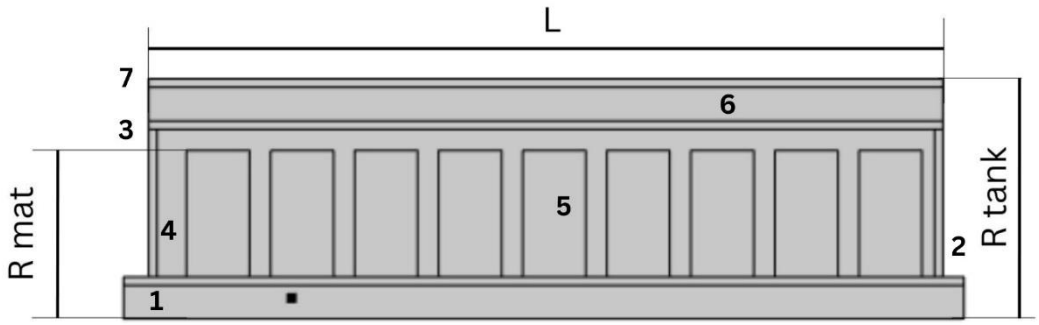

Figure 34: Geometry 9 section configuration.

Geometry 10

This tank was created for vertical installation within the container. It is possible to install 12 tanks according to the container's interior volume. The tanks in this design have a length of 1.89 meters, an outer radius of 0.47 meters, an adsorbent radius of 0.3 meters, and 9 torus material pieces.

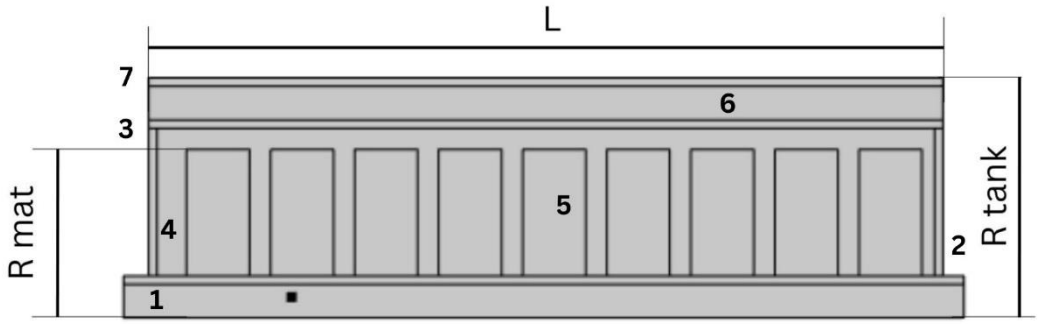

Figure 35: Geometry 10 layout.

Geometry 11

This design was conceptualized to be installed horizontally in the container, and considering the interior volume restrictions, 4 tanks could be employed. This geometry has a tank longitude of 10.89m, an external radius of 0.57 m, an adsorbent radius of 0.4m, and 54 torus adsorbent.

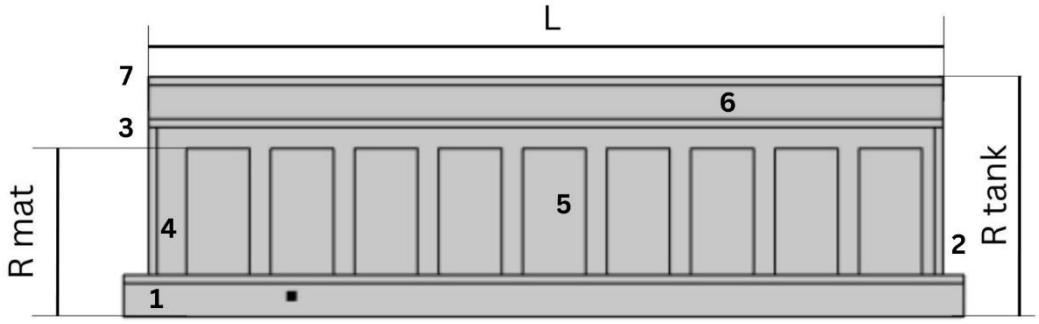

Figure 36: Geometry 11 design concept.

Geometry 12

This configuration was designed for a horizontal implementation in the container, and considering the container interior volume restrictions, 4 tanks could be employed. This geometry has a tank longitude of 10.89m, an external radius of 0.47 m, an adsorbent radius of 0.3m, and 54 torus material pieces.

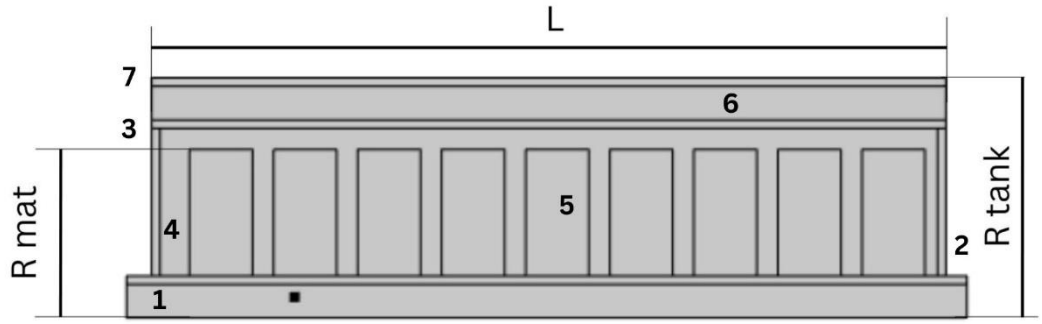

Figure 37: Geometry 12 section layout.

Geometry 13

This layout was designed to be installed vertically in the container, and considering the interior volume, 6 tanks could be installed. This geometry has a tank longitude of 1.89m, an external radius of 0.57 m, an adsorbent radius of 0.4m, and a longitude of the hydrogen host of 1.8 m.

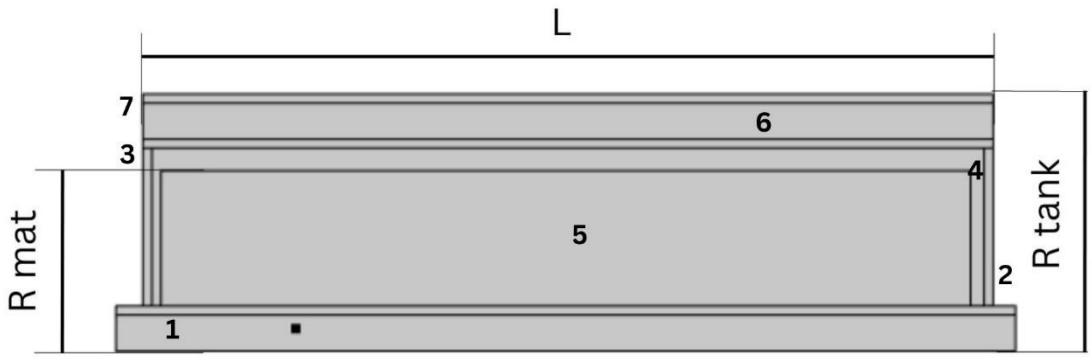

Figure 38: Geometry 13 definition

Geometry 14

This tank was created for vertical installation within the container. It is possible to install 12 tanks according to the container's interior volume. The tanks in this design have a length of 1.89 meters, an outer radius of 0.47 meters, an adsorbent longitude of 1.8 meters, and a host radius of 0.3m.

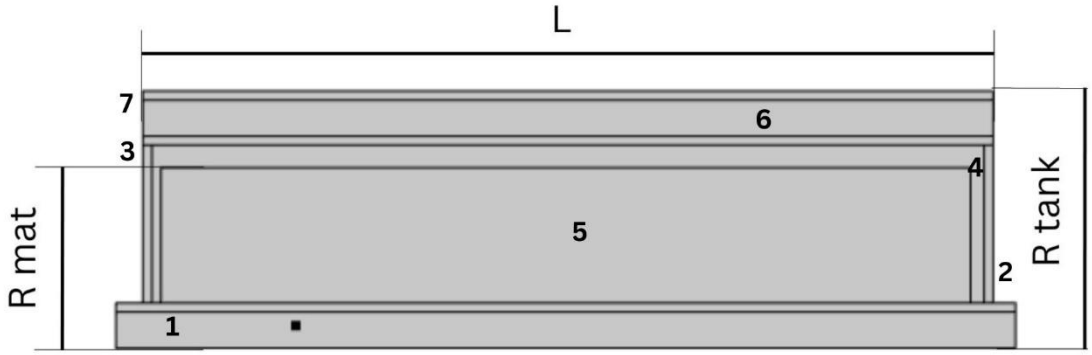

Figure 39: Geometry 14 layout.

Geometry 15

This design was conceptualized to be installed horizontally in the container, and considering the interior volume restrictions, 4 tanks could be employed. This geometry has a tank longitude of 10.89m, an external radius of 0.57 m, an adsorbent radius of 0.4m, and an adsorbent length of 10.8m.

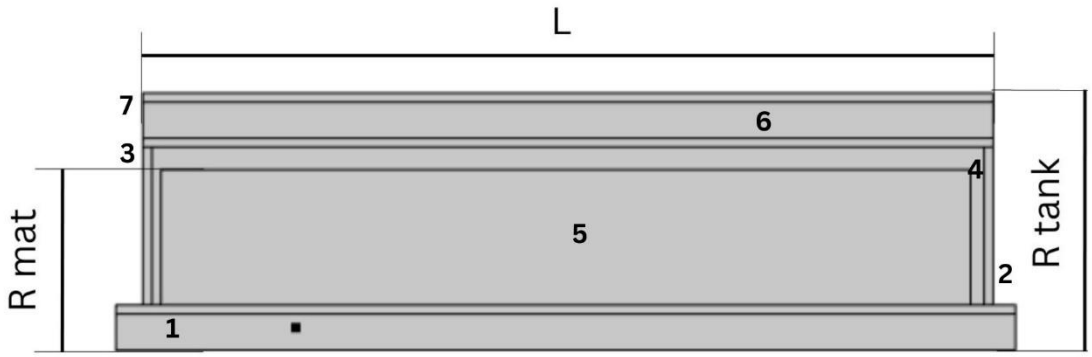

Figure 40: Geometry 15 section design.

Geometry 16

This configuration was designed for a horizontal implementation in the container, and considering the container interior volume restrictions, 4 tanks could be employed. This geometry has a tank longitude of 10.89m, an external radius of 0.47 m, an adsorbent radius of 0.3m, and material longitude of 10.8m.

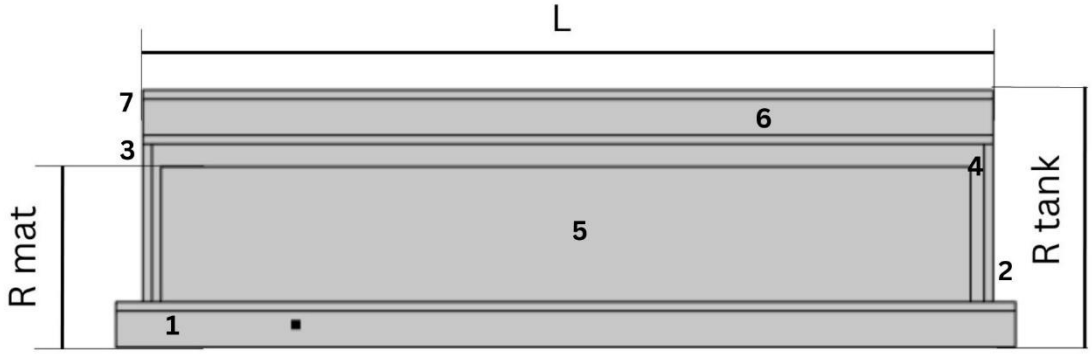

Figure 41: Geometry 16 configuration.